Simulations of Lattice Fermions with Chiral Symmetry in Quantum Chromodynamics

D I S S E R T A T I O N

zur Erlangung des akademischen Grades
doctor rerum naturalium
(dr. rer. nat.)
im Fach Physik

eingereicht an der
Mathematisch-Naturwissenschaftlichen Fakultät I
Humboldt-Universität zu Berlin

von
Herr Dipl.-Phys. Stanislav Shcheredin
geboren am 17.12.1978 im Moskauer Gebiet

Abstract

This thesis is dedicated to explore the feasibility of extraction of the low energy constants of the chiral Lagrangian in the epsilon–regime of quenched QCD. We apply two formulations of the Ginsparg-Wilson fermions, namely, the Neuberger operator and the hypercube overlap operator to compute the observables of interest. As a main result we present the comparison of the distributions of the leading individual eigenvalues of the Neuberger operator in QCD and the analytical predictions of chiral random matrix theory. We observe a good agreement as long as each side of the physical volume exceeds about 1.12 fm. At the same time the chiral condensate Sigma can also be estimated. It turns out that this bound for L is generic and sets the size of the physical volume where the axial correlator behaves according to chiral perturbation theory. This allows us to compute a value for the pion decay constant. The simulations also show that due to the high probability of the near-zero modes it is prohibitively difficult to sample the axial correlator in the neutral topological sector. In the higher sectors, however, we observe that the sensitivity of the analytical predictions for the axial correlator to extract Sigma is lost to a large extent. As an alternative procedure we only consider the contribution from the zero modes. Here we are able to obtain an estimate for the pion decay constant and alpha, where alpha is a low energy constant peculiar to quenching. We calculate the topological susceptibility, both for the Neuberger operator and for the overlap hypercube operator. It turns out that the result with the overlap hypercube operator is closer to the continuum limit. Also the locality properties are superior to those of the Neuberger fermions. As a theoretical development the Lüscher topology conserving gauge action is investigated. This enables us to sample the observables of interest in the epsilon–regime without recomputing the index.

Keywords:
lattice QCD, chiral perturbation theory, random matrix theory, epsilon regime

Zusammenfassung

Das Ziel dieser Dissertation besteht darin, die Realisierbarkeit der Berechnungen der Niederenergie-Konstanten der chiralen Lagrangedichte zur Gewinnung physikalischer Informationen im epsilon–Regime der quenched QCD zu erforschen. Wir haben der Neuberger Operator und Overlap Hyperkubus Operator eingesetzt. Ein Hauptergebniss dieser Arbeit ist der Vergleich der Wahrscheinlichkeitsverteilungen einzelner Eigenwerte des Neuberger Operators in der QCD mit den analytischen Vorhersagen der Theorie der Zufallsmatritzen. Wir beobachten eine gute Übereinstimmung solange jede Seite des physikalischen Volumens größer als etwa 1.12 fm ist. Dabei kann auch das chirale Kondensat Sigma abgeschätzt werden. Es ergab sich, daß diese untere Schranke von L allgemein gilt und die Größe des physikalischen Volumens, auf dem der Axialkorrelator den Vorhersagen des chiralen Störungstheorie folgt, festlegt. Damit koennen wir die Pionzerfallskonstante bestimmen. Unsere Simulationen zeigen, daß wegen der großen Wahrscheinlichkeit niedriger Eigenwerte die Messung des Axialkorrelators im topologischen neutralen Sektor extrem aufwändig ist. Doch reicht die Empfindlichkeit der Vorhersagen der chiralen Störungstheorie in höheren topologischen Sektoren bei der gegebenen Statistik nicht zur Bestimmung von Sigma aus. Als alternative Methode, gehen wir dazu über, allein den Beitrag der Nullmoden zu betrachten. Hier koennen wir Abschätzungen für die Pionzerfallskonstante und alpha gewinnen. Wir berechnen die topologische Suszeptibilität für den Neuberger und Overlap Hyperkubus Operator. Im letzten Fall ist der berechnete Wert näher beim Kontinuumslimes. Die Lokalisierung für den Overlap Hyperkubus Operator ist auch besser als für den Neuberger Operator. Unser anderes Ziel ist die Erforschung einer topologieerhaltenden Eichwirkung.

Acknowledgments

First of all I would like to express my gratitude to Prof. Michael Müller-Preußker for having made it possible for me to make my Ph.D. in his theoretical group. In particular I received a great scientific supervision as well as the all possible support. I would also like to thank Dr. Karl Jansen for letting me join the χLF collaboration and for many interesting ideas which stimulated me as a scientist. Especially I am indebted to Dr. Wolfgang Bietenholz who became my direct supervisor during my Ph.D. His careful and kind supervision as well as the fascinating ideas filled me all these years and contributed a great deal to my world view as well as to my scientific education. Further I would like to acknowledge Prof. J. J. M. Verbaarschot, Prof. P. Damgaard and Prof. G. Akemann for useful discussions concerning the issues addressed in the thesis. I would also like to acknowledge all my colleagues: Dr. F. Hofheinz, Dipl. Phys. A. Sternbeck and Dipl. Phys. D. Peschka for creating a wonderful working atmosphere and helping me to figure out a number of small things which occur in everyday life. And last but not least I would like to thank my mother and grandmother for the kind support.

Contents

List of Figures

List of Tables

Chapter 1

Motivation

This dissertation is dedicated to the Quantum Chromodynamics (QCD), a theory that explained already many effects and processes in the hadron world.

QCD is a part of the Standard Model of elementary particles with the gauge group $SU(3) \otimes SU(2) \otimes U(1)$. It is the theory that describes the strong interactions of quarks and gluons. Quarks are the fermion fields which belong to the fundamental representation of the gauge group $SU(3)$ and gluons being in its Lie algebra. In QCD the strong interactions are mediated by the exchange of these gauge bosons. Due to the non-Abelian nature of the gauge group $SU(3)$ a self interaction of the gauge bosons is also present. There is experimental evidence that the quarks come in six flavors: up (u), down (d), strange (s), charm (c), bottom (b) and top (t).

Many QCD calculations were successful in the domain of high energies where — due to the asymptotic freedom — the coupling constant becomes a convenient small expansion parameter. This is the perturbative regime where many quantities of interest can be expressed in terms of the asymptotic expansion in powers of the strong coupling constant α_s.

In the domain of energies of order 1 GeV the coupling constant rises to order 1, $\mathcal{O}(1)$, and the perturbative treatment fails. Therefore a non-perturbative approach must be applied to address the problems of interest in this domain. This scale of energies corresponds to color singlet bound states of quarks when they form hadrons. One distinguishes between mesons, consisting of a quark and antiquark, and baryons, consisting of three quarks. An elegant classification of the mesons and baryons is given by the quark model. The particles are identified with the fields belonging to the irreducible representation of their flavor group. To this end the classification of the mesons for the flavor group $SU(2)$ is $\bar{2} \otimes 2 = 3 \oplus 1$, i.e. there is a triplet of meson fields and a singlet. For the $SU(3)$ group the pattern is $\bar{3} \otimes 3 = 8 \oplus 1$, i.e. an octet and a singlet. In experiments on the deep inelastic scattering

the building blocks of hadrons, the partons, were identified. The quarks are, however, observed in nature only in such bound states and no free quark has ever been found. This phenomenon, known as confinement, cannot be derived by the perturbative analysis.

From experimental data of particles one can see three lightest hadronic states π^0, π^+, π^- belonging to the triplet of the $SU(2)$ multiplet of u, d flavors and π^0, π^+, π^-, η, K^+, K^-, K^0, $\bar{K}^0$ belonging to the octet of the $SU(3)$ multiplet of u, d, s flavors with the masses below the mass of the higher lying ρ meson. At present it is generally assumed to be a result of the spontaneous chiral symmetry breaking which occurs in the massless QCD Lagrangian. The non-vanishing quark masses break the chiral symmetry of the Lagrangian explicitly which gives rise to non-zero masses of the quasi-Goldstone bosons. The particles in the multiplets are identified with these quasi-Goldstone bosons. Their masses are proportional to the square root of the quark masses. This phenomenon, known as the chiral symmetry breaking, is a truly non-perturbative effect. The chiral symmetry that is broken at low energies is, however, expected to be restored if the energies are increased. This scenario corresponds to a phase transition. An order parameter indicating this phase transition is the chiral condensate $\langle \bar{\psi}\psi \rangle$, which is zero in the chirally symmetric phase and picks up a non-zero value once we pass to the chirally broken phase.

Lattice QCD is a theory that provides a non-perturbative approach from the first principles. One introduces a space-time lattice and formulates the theory by a lattice regularized path integral. Quarks and gluons become regularized fields. Quarks are represented by Grassmann spinor fields attached to the lattice sites and the gauge fields are represented by parallel transporters defined on the lattice links. The regularization introduces a momentum cut-off π/a, where a is the lattice spacing. This represents a statistical model that is subject to the Monte Carlo simulations on a computer. The continuum limit is recovered if one sends the lattice spacing to 0 and the number of lattice sites to infinity, keeping the physical volume fixed.

When addressing the phenomenon of the chiral symmetry breaking and the physics of the light quarks, it is vital to have a discretization of fermions which preserves the chiral symmetry at finite lattice spacing. In this thesis we will describe results obtained with various formulations of such chiral fermions. At present all these formulations are tedious to simulate in QCD due to their computational overhead compared to the non-chiral discretizations such as the Wilson fermions. Therefore all simulations are carried out at quite small physical volumes and the values of the meson masses higher than one would expect in nature. The latter is reflected for instance in the pion mass. Hence the simulated data have to be necessarily extrapolated to

the small physical quark masses. In addition the quark loops are also neglected which leads to quite difficult accountable systematic uncertainties. A way to extract physical information from the QCD simulations is to use theoretical predictions provided by a low energy effective theory. In the context of QCD this is the Chiral Perturbation Theory (χPT).

Owing to the mass gap between the quasi-Goldstone bosons and the first heavier mesons (the ρ–meson) one can integrate out all higher excitations of the mass spectrum of QCD leaving the theory defined solely in terms of the quasi-Goldstone bosons. The resulting theory is a low energy effective theory, which is called the χPT.

An attractive feature for the numerical simulations is that χPT can be formulated in a finite volume and some analytical predictions can be computed which are the same as in the infinite volume. Moreover since the present lattice simulations are done without quark loops this can also be accounted for in the quenched χPT which provides an analytical guide-line for quenched lattice simulations. In particular the analytical predictions in the framework of χPT have been worked out for the regime of the soft pion where the Compton wavelength cannot be accommodated in the finite volume. This regime, though representing an unphysical situation, provides a powerful tool for the lattice simulations with chiral fermions. The main advantage is that the finite size effects can be calculated in this setting using the χPT and the low energy constants appearing in the corresponding analytical expressions are those of the infinite volume. The control over the finite size effects, which one otherwise wishes to suppress, provides us with physical information. Since in this regime one does not need to use large lattices, it is viewed to be promising for obtaining the low energy constants parameterizing the χPT Lagrangian. This can be achieved by using the formalism of the chiral fermions. The use of the chiral fermions allows us to perform calculations at small meson masses and thereby approach their physical values, i.e. the so-called chiral limit of observables of interest.

In Chapter 2 we give an introduction and fix our notations in QCD, χPT and chiral Random Matrix Theory. Lattice QCD will also be briefly discussed. For completeness the traditional formulations of lattice fermions will be reviewed. We discuss various formulations of the chiral lattice fermions realized through the Ginsparg-Wilson relation. In particular we consider the conventional formulation of the overlap fermions and an improved formulation based on the perfect action — the hypercube fermions. The Chapter 3 is concerned with simulation aspects of the Ginsparg-Wilson fermions and also quenched gauge simulations are briefly discussed. The Chapter 4 deals with the numerical aspects of simulation of the hypercube fermions. In Chapter 5 we present our results for the dependence of the pion mass versus the bare

quark mass. In Chapter 6 the results for the distributions of the eigenvalues of the overlap Dirac operator are considered in conjunction with the chiral Random Matrix Theory. In Chapter 7 the results for the topological susceptibility, computed with the chiral fermions, are addressed. In Chapter 8 the two-point mesonic functions are addressed. We discuss the feasibility to extract the physical information from the axial and pseudo-scalar correlators. In Chapter 9 we present a study of a gauge action which may be useful for the future lattice simulations in the ϵ–regime. In Chapter 10 we draw the conclusions and give an outlook.

Chapter 2

Theoretical background

2.1 QCD at first glance. Gluons and quarks

In this Section we introduce the basic notation of QCD. Its degrees of freedom are carried by quarks and gluons. Gluons are described by the non-Abelian $SU(3)$ gauge group while quarks belong to its fundamental representation. We will consider QCD in Euclidean space that will be the relevant theory for the results discussed in the thesis. The Euclidean formulation is especially useful for the lattice simulations since the theory becomes a statistical ensemble with the Boltzmann weight $\exp\left(-S_{QCD}\right)$, where S_{QCD} is the QCD action. The use of the Euclidean formulation is justified since there exists an analytical continuation of the Euclidean Green functions to the Minkowski space [2, 3].

The quarks are represented by spinor fields in the fundamental representation of the $SU(3)$ color group, and the gluon vector fields A_μ ($\mu = 1, \ldots, 4$) take their values in the Lie algebra of the $SU(3)$ color group. The quarks come in six flavors ψ_f, where $f = 1, \ldots, 6$. We decompose the matrix valued vector potential A_μ in fields A_μ^a, where $a = 1, \ldots, N_c^2 - 1$ with N_c being the number of colors,

$$A_\mu = -ig \sum_{a=1}^{N_c^2-1} A_\mu^a \frac{T_a}{2} \ . \tag{2.1}$$

g is the bare coupling constant and the matrices T_a are the generators of the gauge group $SU(3)$, which are traceless and Hermitian. They are normalized by

$$\mathrm{Tr}(T^a T^b) = \frac{1}{2}\delta_{ab} \ .$$

The generators satisfy the commutation relation

$$\left[\frac{T^a}{2}, \frac{T^b}{2}\right] = i f_{abc} \frac{T^c}{2} \ , \tag{2.2}$$

where f_{abc} are structure constants of the $SU(3)$ Lie group which can be chosen to be real. The values of the structure constants for the special choice of generators as the Gell-Mann matrices are given in Ref. [4].

We split the QCD action into two parts, $S_{\mathrm{QCD}} = S_{\mathrm{YM}} + S_{\mathrm{F}}$, with the action of quarks given by

$$S_{\mathrm{F}} = \sum_{f=1}^{N_f} \int_V d^4x \, \bar{\psi}_f (\mathcal{D} + m_f) \psi_f \ . \tag{2.3}$$

N_f is the number of quark flavors, S_{YM} is the Euclidean Yang-Mills action, $\mathcal{D}$ is the massless Dirac operator and m_f is the quark mass corresponding to the flavor f. The integration is done over the Euclidean four-volume $V = L^3 \times T$. The boundary conditions are taken to be periodic up to a gauge transformation for the gluons, and antiperiodic for the quarks. This defines the theory on a four dimensional torus. The QCD Dirac operator is given by

$$\mathcal{D} = \gamma_\mu (\partial_\mu + A_\mu) \ . \tag{2.4}$$

The γ_μ are the Euclidean Dirac matrices with $\{\gamma_\mu, \gamma_\nu\} = 2\delta_{\mu\nu}$. We chose them such that the Dirac operator is anti-Hermitian, $\mathcal{D}^\dagger = -\mathcal{D}$. In particular we use the chiral representation in which $\gamma_5 \equiv \gamma_1 \gamma_2 \gamma_3 \gamma_4 = \mathrm{diag}\,(1, 1, -1, -1)$ (see for instance Ref. [5]).

The Euclidean Yang-Mills gauge action is given by

$$S_{\mathrm{YM}} = \frac{1}{4} \int_V d^4x \, F_{\mu\nu}^a F_{\mu\nu}^a \ . \tag{2.5}$$

In this formula, and throughout this thesis, the summation over the repeated indices is assumed if not stated otherwise. The field strength tensor $F_{\mu\nu}^a$ carries one color a index running from $1 \ldots N_c^2 - 1$ and two Lorentz indices $\mu, \nu = 1 \ldots 4$,

$$F_{\mu\nu}^a = \partial_\mu A_\nu^a - \partial_\nu A_\mu^a + g f_{abc} A_\mu^b A_\nu^c \ . \tag{2.6}$$

The theory is finally defined by its partition function in the form of the functional integral over the fermion fields ψ_f and $\bar{\psi}_f$ and the gauge vector potential A_μ in the Euclidean space,

$$Z^{\mathrm{QCD}}(m_f, \theta) = \int \prod_\mu [DA_\mu] \prod_{f=1}^{N_f} [D\psi_f D\bar{\psi}_f] \, e^{-S_{\mathrm{QCD}}[\bar{\psi}_f, \psi_f, A] + i\theta\nu[A]} \ . \tag{2.7}$$

The parameter θ is a real vacuum angle and the topological charge ν is defined by

$$\nu[A] = -\frac{1}{32\pi^2} \int_V d^4x \, \epsilon_{\alpha\beta\rho\sigma} \mathrm{Tr}(F_{\alpha\beta}F_{\rho\sigma}) \tag{2.8}$$

where $\epsilon_{\alpha\beta\rho\sigma}$ is the antisymmetric unit tensor of rank four. $\nu[A]$ is the winding number of a field configuration and takes integer values for finite action field configurations. The field ψ_f is a four component spinor field and $\bar{\psi}_f$ is a conjugate spinor field. Integrating out the fermion degrees of freedom we arrive at

$$Z^{\mathrm{QCD}}(m_f, \theta) = \int \prod_\mu DA_\mu \prod_{f=1}^{N_f} \det(\mathcal{D} + m_f) \, e^{-S_{\mathrm{YM}}[A] + i\theta\nu[A]} . \tag{2.9}$$

The integral over all field configurations $\int \prod_\mu [DA_\mu]$ includes a sum over all topological sectors ν.

The partition function in the sector of topological charge ν is obtained by the Fourier transform

$$Z_\nu^{\mathrm{QCD}}(m_f) = \frac{1}{2\pi} \int_0^{2\pi} d\theta \, e^{-i\nu\theta} Z^{\mathrm{QCD}}(m_f, \theta) . \tag{2.10}$$

2.2 Chiral symmetry breaking and eigenvalues of the Dirac operator

2.2.1 Implications of the chiral symmetry for the structure of the Dirac operator

In this Section we discuss the chiral symmetry in QCD and its implication for the spectrum of the Dirac operator.

We start from the definitions of right-handed and left-handed spinors $\psi^{R/L}$ which are defined as projections of ψ and $\bar{\psi}$

$$\begin{aligned}
\psi^{R/L} &= P^{(+/-)}\psi , \quad \bar{\psi}^{R/L} = \bar{\psi}P^{(-/+)} , \\
P^{(+/-)} &= \frac{1}{2}(1 \pm \gamma_5) , \\
1 &= P^{(+)} + P^{(-)}, \quad P^{(+)}P^{(-)} = 0 ,
\end{aligned} \tag{2.11}$$

where the spinor ψ describes N_f Dirac spinor species.

The massless Dirac operator satisfies the anticommutation relation

$$\{\gamma_5, \mathcal{D}\} = 0 . \tag{2.12}$$

7

Using the decomposition of the fermion fields ψ, $\bar{\psi}$

$$\psi = \psi^R + \psi^L, \quad \bar{\psi} = \bar{\psi}^R + \bar{\psi}^L \tag{2.13}$$

we obtain for the fermion action

$$S_F = \int d^4x \left(\bar{\psi}^R \mathcal{D} \psi^R + \bar{\psi}^L \mathcal{D} \psi^L + \bar{\psi}^R M \psi^L + \bar{\psi}^L M \psi^R \right) , \tag{2.14}$$

where $M = \mathrm{diag}(m_1, \ldots, m_f)$.

Relation (2.12) can be seen also as an expression of the chiral symmetry of the fermion action for every fermion flavor ψ_f,

$$\psi_f \rightarrow e^{i\alpha\gamma_5} \psi_f , \quad \bar{\psi}_f \rightarrow \bar{\psi}_f e^{i\alpha\gamma_5} , \tag{2.15}$$

where α is a real angle of the chiral rotation. The quark action (2.14) remains invariant under a chiral rotation if $M = 0$.

One can write down an eigenvalue equation for $\mathcal{D}$ as

$$\mathcal{D}[A]\psi_n = i\lambda_n \psi_n , \quad \lambda_n \in \mathbb{R} , \tag{2.16}$$

where the eigenvalues and eigenfunctions depend on the gauge field. Using Eq. (2.12) one can show that the nonzero eigenvalues of $\mathcal{D}$ occur in pairs $\pm i\lambda_n$ with eigenfunctions ψ_n and $\gamma_5 \psi_n$. Indeed, if $i\lambda_n$ is an eigenvalue of $\mathcal{D}$ and ψ_n is the corresponding eigenfunction, then Eq. (2.12) implies

$$\mathcal{D}\gamma_5 \psi_n = -\gamma_5 \mathcal{D} \psi_n = -i\lambda_n \gamma_5 \psi_n , \tag{2.17}$$

hence $\gamma_5 \psi_n$ is also an eigenfunction of $\mathcal{D}$ with the eigenvalue $-i\lambda_n$. There can also be eigenvalues equal to zero, $\lambda_n = 0$. Because of Eq. (2.12) the corresponding eigenfunctions can be arranged to be simultaneous eigenfunctions of $\mathcal{D}$ and γ_5 with eigenvalues ± 1 of γ_5, i.e. these states have a definite chirality. Denoting the number of zero eigenvalues per flavor f with positive and negative chirality by N_+ and N_-, respectively, the Atiyah-Singer index theorem [6] states that

$$\nu = N_f(N_+ - N_-) \tag{2.18}$$

is a topological invariant that does not change under continuous deformations of the gauge field. Note that the Atiyah-Singer index theorem identifies the definition of the index given by gauge fields (2.8) and the definition given by the index of the Dirac operator, i.e. the fermionic index.

In a chiral basis with $\gamma_5 \psi_n^{R/L} = \pm \psi_n^{R/L}$, one can use Eq. (2.12) to show that $\langle \bar{\psi}_m^R | \mathcal{D} | \psi_n^L \rangle = 0 = \langle \bar{\psi}_m^L | \mathcal{D} | \psi_n^R \rangle$ for all m and n. From this property and the fact that $\mathcal{D}$ is anti-Hermitian, it follows that the projection of the

Dirac operator onto the subspace spanned by the zero modes has the matrix structure

$$\mathcal{D}^{(0)} = \begin{pmatrix} 0 & iW \\ iW^\dagger & 0 \end{pmatrix} . \tag{2.19}$$

This off-diagonal block structure is characteristic for systems with chiral symmetry. The matrix W has dimension $N_f N_+ \times N_f N_-$, and the matrix $\mathcal{D}$ in Eq. (2.19) has $|\nu|$ eigenvalues equal to zero.

Using formula (2.19) we can write down the contribution of the zero modes to the fermion action as

$$S_F^{(0)} = \int d^4x \left(\bar{\psi}^R iW^\dagger \psi^R + \bar{\psi}^L iW \psi^L + \bar{\psi}^R M \psi^L + \bar{\psi}^L M \psi^R \right) . \tag{2.20}$$

In the chiral limit where all $m_f = 0$, the fermion actions (2.14) as well as (2.20) are invariant under the global transformations

$$\begin{aligned}
\psi^L &\rightarrow L\psi^L , & \bar{\psi}^L &\rightarrow \bar{\psi}^L L^{-1} , \\
\bar{\psi}^R &\rightarrow \bar{\psi}^R R^{-1} , & \psi^R &\rightarrow R\psi^R .
\end{aligned} \tag{2.21}$$

$L \in U_L(N_f)$ and $R \in U_R(N_f)$, where $U_L(N_f)$ and $U_R(N_f)$ are independent unitary groups. If the number of right-handed states $N_R = N_f N_+$ is equal to the number of left-handed states $N_L = N_f N_-$, the symmetry is thus $U_R(N_f) \otimes U_L(N_f)$. However, if $N_R \neq N_L$, i.e. if $\nu \neq 0$, the axial symmetry group $U_A(1)$, which is a U(1) subgroup of $U_R(N_f) \otimes U_L(N_f)$, is broken by instantons. Invariance under a second subgroup U(1) of $U_R(N_f) \otimes U_L(N_f)$, the group $U_V(1)$, corresponds to the conservation of the baryon number. The full flavor symmetry group in the chiral limit is thus given by $G = SU_R(N_f) \otimes SU_L(N_f)$.

Since G is a symmetry group for the massless fermion action one can write down the Noether currents

$$\begin{aligned}
J_{a\mu}^L &= \bar{\psi}\gamma_\mu \frac{(1-\gamma_5)}{2} T^a \psi , \\
J_{a\mu}^R &= \bar{\psi}\gamma_\mu \frac{(1+\gamma_5)}{2} T^a \psi .
\end{aligned} \tag{2.22}$$

T^a is a generator of the $SU(N_f)$ group, where $a = 1, \ldots, N_f^2 - 1$. One obtains conserved Noether charges by the usual procedure,

$$Q_a^{R/L} = \int d^3x \, J_{a4}^{R/L}(x) . \tag{2.23}$$

We construct generators of the axial $\mathrm{SU}_A(N_f)$ and vector subgroup $\mathrm{SU}_V(N_f)$ by linear combination of the Noether currents J^L and J^R,

$$
\begin{aligned}
J^A_{a\mu} &= J^R_{a\mu} - J^L_{a\mu} \ , \\
J^V_{a\mu} &= J^R_{a\mu} + J^L_{a\mu} \ .
\end{aligned}
\tag{2.24}
$$

The other two currents which are related to the $\mathrm{U}_V(1)$ and $\mathrm{U}_A(1)$ symmetries are given by

$$
\begin{aligned}
J^A_{0\mu} &= \bar{\psi}\gamma_5\gamma_\mu\psi \ , \\
J^V_{0\mu} &= \bar{\psi}\gamma_\mu\psi \ .
\end{aligned}
\tag{2.25}
$$

As we mentioned before, for $\nu \neq 0$ the axial current $J^A_{0\mu}$ is not conserved. Its divergence is given by

$$
\partial_\mu J^A_{0\mu}(x) = -\frac{N_f}{32\pi^2}\epsilon_{\mu\nu\rho\sigma}\mathrm{Tr}[F_{\mu\nu}(x)F_{\rho\sigma}(x)] \ .
\tag{2.26}
$$

One can also see that the axial $\mathrm{SU}(N_f)$ subgroup with $L = R^{-1}$ is broken explicitly by the mass term. On the other hand the $\mathrm{SU}(N_f)$ vector subgroup (with $L = R$) is not broken for degenerate quark masses ($m_f = m$ for all f), but breaks explicitly for different quark masses ($m_f \neq m_{f'}$ for some $f \neq f'$).

If the quark masses were zero, the action (2.20) would have an exact axial flavor $\mathrm{SU}(N_f) \otimes \mathrm{SU}(N_f)$ symmetry. However, there is strong evidence that the axial $\mathrm{SU}(N_f)$ subgroup with $L = R^{-1}$ is broken spontaneously with the following spontaneous symmetry breaking pattern of the chiral group,

$$
\mathrm{SU}_R(N_f) \otimes \mathrm{SU}_L(N_f) \rightarrow \mathrm{SU}_V(N_f) \ .
\tag{2.27}
$$

This implies that the ground state of the quantum system being invariant with respect to the $\mathrm{SU}_V(N_f)$ is, however, not invariant with respect to the $\mathrm{SU}_A(N_f)$ symmetry. According to the Goldstone theorem spontaneous breaking of a Lie group G down to a Lie group H gives rise to Goldstone boson fields [7, 8]. The Goldstone manifold is a coset space $G/H = \mathrm{SU}(N_f)$, and so there are $N_f^2 - 1$ Goldstone bosons.

The fact that the pattern of the spontaneous symmetry breaking has the form $\mathrm{SU}_R(N_f) \otimes \mathrm{SU}_L(N_f)$ to $\mathrm{SU}_V(N_f)$ is supported firstly by the absence of the parity doublets in the hadron spectrum. Indeed in the mass spectrum one can observe three light pseudo-scalar particles, the pions (which are the triplet of an approximate $\mathrm{SU}(2)$ meson multiplet) as well as somewhat heavier pseudo-scalars —the four kaons K^+, K^0, $\bar{K}^0$, K^- and the η -meson (belonging to the approximate $\mathrm{SU}(3)$ meson multiplet). Along with

the eight approximate Goldstone bosons one observes a heavier η' meson. Its mass is too large to be considered as a result of the spontaneous symmetry breaking of the axial $U_A(1)$ subgroup. According to 't Hooft's idea its mass receives contributions from instantons due to a relation of the derivative of the anomaly axial current to the topological charge [9, 10].

Secondly the value of the chiral condensate $\langle\bar\psi\psi\rangle = \langle\bar\psi^R\psi^L\rangle + \langle\bar\psi^L\psi^R\rangle$ would be zero if the ground state was axial-flavor symmetric. However, lattice QCD simulations indicate that $\langle\bar\psi\psi\rangle$ is non-zero. The quantity $\langle\bar\psi\psi\rangle$ is only invariant if $L = R$, i.e. the vacuum state is symmetric under the flavor group $H = \mathrm{SU}_V(N_f)$. Thus, the vector symmetries are unbroken, whereas the axial symmetries are maximally broken. If we now add to this scenario of the spontaneous chiral symmetry breaking the explicit symmetry breaking by the mass terms of light quarks, then we arrive at a consistent picture for the observable approximate $SU(2)$ triplet and $SU(3)$ octet. Comparing masses of the pions in the triplet and pions, kaons and η meson in the octet, we see that the explicit symmetry breaking is larger for the octet. This implies that the mass of the strange quark in the QCD Lagrangian is large compared to masses of the u and d quarks, which one often assumes to be degenerate.

2.2.2 Spectral density of the Dirac operator

In terms of the eigenvalues of the Dirac operator, the QCD partition function (2.9) can be rewritten as

$$
Z^{\mathrm{QCD}}(m_f, \theta) = \sum_{\nu=-\infty}^{+\infty} e^{i\nu\theta} \prod_{f=1}^{N_f} m_f^{|\nu|} \int_\nu DA_\mu \prod_{k\geq 1}(\lambda_k^2 + m_f^2)e^{-S_{\mathrm{YM}}[A]} , \quad (2.28)
$$

where $\int_\nu DA_\mu$ denotes the path integral over field configurations with topological charge ν. The eigenvalues of the Dirac operator, λ_k, are introduced in Eq. (2.16).

The spectral density of the Dirac operator is given by

$$
\rho(\lambda) = \left\langle \sum_n \delta(\lambda - \lambda_n) \right\rangle , \quad (2.29)
$$

where the expectation value is over gauge fields weighted by the full QCD action. The spectral density is important because of its relation to the order parameter for spontaneous chiral symmetry breaking, the chiral condensate $\Sigma = -\langle\bar\psi\psi\rangle$.

It was shown by Banks and Casher [11] that

$$
\Sigma = \lim_{\varepsilon\to 0} \lim_{m\to 0} \lim_{V\to\infty} \pi\rho(\varepsilon)/V . \quad (2.30)
$$

It is important that the limits are taken in the order indicated. (In the normalization of Eq. (2.29) the spectral density is proportional to the volume, so the explicit factor of $1/V$ in (2.30) is compensated to yield a finite result.) This relation can be readily derived. The chiral condensate is given by

$$\langle \bar{\psi}\psi \rangle = - \lim_{m \to 0} \lim_{V \to \infty} \frac{1}{V N_f} \partial_m \log Z^{\text{QCD}}(m, \theta) \ . \tag{2.31}$$

If we now apply this definition to the partition function (2.28) then we arrive at

$$\langle \bar{\psi}\psi \rangle = - \lim_{m \to 0} \lim_{V \to \infty} \left\langle \frac{1}{V} \sum_{n \geq 1} \frac{2m}{\lambda_n^2 + m^2} \right\rangle \ , \tag{2.32}$$

where the contribution of the zero modes, $|\nu|/(mV)$, was dropped assuming that it becomes asymptotically small in the $V \to \infty$ limit. Now taking the chiral limit we obtain the Banks-Casher relation (2.30).

2.3 χPT as a low energy effective theory of QCD

Due to spontaneous chiral symmetry breaking, at low energies the QCD dynamics is dominated by Goldstone bosons [7, 8] — the pions for $N_f = 2$. It is possible to use a low-energy effective description that only involves the quasi-Goldstone boson fields [12–14]. Chiral perturbation theory [15, 16] provides a systematic low-energy expansion that predicts the pion dynamics based on symmetry principles and a number of low-energy parameters (like the pion decay constant F_π and the chiral condensate Σ) whose values can be determined either from experiments or from lattice QCD calculations.

2.3.1 The chiral Lagrangian and its low energy constants

The Lagrangian of the low-energy effective theory is determined by the global symmetries of the underlying theory. Considering the low energy effective theories one has to think of an energy scale hierarchy and the corresponding theory which is relevant for a given energy interval. As we reduce the energy scale, some degrees of freedom, which were important for higher energies, may become irrelevant for the lower energies.

The low energy effective Lagrangian is constructed as a linear combination of all terms which are local, Lorentz invariant and compatible with the flavor

symmetry. The constants in such an expansion parameterize our lack of knowledge about the underlying theory.

If we write down a low energy effective theory for QCD then the corresponding flavor symmetry includes the chiral symmetry. It is broken down to $SU(N_f)$ and therefore the Goldstone bosons belong to the coset space $SU_R(N_f) \otimes SU_L(N_f)/SU_V(N_f)$, which is again $SU(N_f)$. If we are interested only in the lightest excitations then the Lagrangian will contain only Goldstone fields $U(x)$. Under global chiral rotations they transform as

$$U(x)' = LU(x)R^\dagger \ , \tag{2.33}$$

where L and R are matrices of the chiral transformation belonging to $SU_L(N_f)$ and $SU_R(N_f)$, respectively. To fully determine the theory we need to write down its partition function and specify the measure. The partition function of the chiral perturbation theory takes the following general form

$$Z_{\chi PT} = \int [DU(x)] \exp\left(-\int d^4x \, \mathcal{L}[U]\right) \ , \tag{2.34}$$

where $[DU(x)]$ represents the Haar measure and the integration is done over the flavor group $SU(N_f)$ in each space point x. The Haar measure is a left- and right-invariant measure, i.e.

$$\int_{SU(N_f)} dU \ f(\Omega U) = \int_{SU(N_f)} dU \ f(U\Omega) = \int_{SU(N_f)} dU \ f(U) \ , \tag{2.35}$$

for any function $f(U)$ and for any matrix $\Omega \in SU(N_f)$. It is convenient to normalize the measure such that

$$\int_{SU(N_f)} dU = 1 \ . \tag{2.36}$$

The interaction among the Goldstone bosons is weak at low energies and decreases as the energy is reduced. For the effective Lagrangian it implies that it can be represented as an expansion in derivatives. On the other hand the quark masses can be viewed as parameters which characterize how strongly the chiral symmetry is broken.

To a good absolute accuracy the up and down quarks can be regarded to have nearly the same mass. So for $N_f = 2$ we can choose the mass matrix $\mathcal{M} = m\mathbb{1}$. One can write a systematic low-energy expansion in powers of the pion momentum p and mass $m_{\pi^0}^2 = 2m\Sigma/F_\pi^2$ over the cut-off of the effective theory, $\Lambda_{QCD} \simeq 4\pi F_\pi$. In the standard chiral expansion both quantities, $\frac{p}{\Lambda_{QCD}}$ and $\frac{m_{\pi^0}}{\Lambda_{QCD}}$, are taken to be of the same order. Because of these counting

rules the chiral expansion cannot be considered as a Taylor expansion. Here we give the result for the leading term of the pion effective Lagrangian in the θ vacuum,

$$\mathcal{L}^{(2)} = \frac{F_\pi^2}{4}\mathrm{Tr}(\partial_\mu U^\dagger \partial_\mu U) - \frac{\Sigma}{2}\mathrm{Tr}(e^{i\frac{\theta}{N_f}}\mathcal{M}U^\dagger + Ue^{-i\frac{\theta}{N_f}}\mathcal{M}^\dagger) \ . \qquad (2.37)$$

The first term on the right-hand side is chirally invariant. Its prefactor is given by the constant F_π related to the pion decay constant which determines the strength of the interaction between the Goldstone bosons. The second term is the chiral symmetry breaking mass term which contains the quark mass matrix. Under chiral transformations (2.33) this term transforms as

$$\mathrm{Tr}(e^{i\frac{\theta}{N_f}}\mathcal{M}U'^\dagger + U'e^{-i\frac{\theta}{N_f}}\mathcal{M}^\dagger) = \mathrm{Tr}(e^{i\frac{\theta}{N_f}}\mathcal{M}RU^\dagger L^\dagger + LUR^\dagger e^{-i\frac{\theta}{N_f}}\mathcal{M}^\dagger) \ . \ (2.38)$$

Since we assume the two quarks to have identical masses, the Lagrangian is invariant under $SU(2)$ flavor rotations for which $R = L$. For a general diagonal mass matrix with N_f flavors the flavor symmetry is reduced to $\prod_{f=1}^{N_f} U(1)_f$.

The constants F_π and Σ determine the low-energy dynamics at leading order and enter the effective theory as free parameters.

It can be shown that in the chiral limit

$$\langle 0|J_{0\mu}^A|\pi^+(p)\rangle = i\sqrt{2}F_\pi p_\mu \ . \qquad (2.39)$$

The same formula at physical values of quark masses is in fact the definition of the pion decay constant F_π^{decay}. So the physical value of F_π^{decay} being F_π in the leading order is modified by $\mathcal{O}(m_f^2) \sim \mathcal{O}(p^4)$ corrections in the next-to-leading order,

$$F_\pi^{\mathrm{decay}} = F_\pi + \mathcal{O}(m_f^2, p^4) \ . \qquad (2.40)$$

The pion decay constant is experimentally known from the process $\pi^\pm \to \mu^\pm + \nu$ and it is approximately 93 MeV. If we formulate the chiral Lagrangian for the $SU(3)$ flavor group — i.e. including the s-quark — then in addition to the pion decay constant we will have also the kaon decay constant. In principal one could relate it to the prefactor of the kinetic term of the chiral Lagrangian. The kaon decay constant is about 114 MeV. The difference between the pion decay constant and the kaon decay constant is a typical $\mathcal{O}(p^4)$ effect, which is beyond the lowest order. However, the effects of order $\mathcal{O}(p^4)$ are expected to be larger in the case of the kaon decay constant. Therefore the most natural determination of the prefactor at $\mathcal{O}(p^2)$ is still provided by the pion decay constant.

Contrary to the decay constants, the quark condensate is not directly related to any physical observable. It is the product $m_q B$, where $B = \Sigma/F_\pi^2$, that can be constrained by means of experimental data. To the leading order we have

$$
\begin{aligned}
m_{\pi^0}^2 &= (m_u + m_d)B, \\
m_{K^0}^2 &= (m_d + m_s)B \ .
\end{aligned}
\tag{2.41}
$$

The analogous equation for $m_{\eta_8}^2$, where η_8 denotes the octet component of the η meson, contains no new parameters and gives rise to a consistency relation,

$$
3m_{\eta_8}^2 = 4m_{K^0}^2 - m_{\pi^0}^2 \ .
\tag{2.42}
$$

This is the famous Gell-Mann-Okubo mass formula, well satisfied by experimental data under the assumption $m_\eta = m_{\eta_8}$. The validity of the Gell-Mann-Okubo formula provides a significant a posteriori check that the $\mathcal{O}(m_q^2)$ corrections to Eq. (2.41) are small.

Up to these two low-energy constants the Goldstone boson dynamics at the leading order of the chiral perturbation theory is completely determined by chiral symmetry. At higher energies additional terms arise in the effective theory. Again, they are restricted by chiral symmetry and they contain new low energy constants — the Gasser-Leutwyler coefficients.

2.3.2 The $p-$ and ϵ−expansion of χPT

Let the system now to be placed in a four dimensional box of length L. We assume from now on that the volume is large with respect to the QCD scale set by the $1/\Lambda_{QCD}$. More precisely, the allowed momenta should not take values higher than the scale of the chiral symmetry breaking in the infinite physical volume given by $\Lambda_{QCD} = 4\pi F_\pi$,

$$
p \sim \frac{2\pi}{L} \ll 4\pi F_\pi \ .
\tag{2.43}
$$

As a general property, no chiral symmetry breaking occurs in a finite volume. However, this condition separates the hard momenta from the soft ones and thereby provides the corresponding framework for calculations in the finite volume.

The inverse product $1/(F_\pi L)$ is not the only relevant parameter. Also the relative size of m_π and $1/L$ is important, as it was discussed in the previous Section. Indeed the χPT considers an expansion in two parameters: the mass of the quasi-Goldstone boson m_π and its momentum p over the scale $4\pi F_\pi$.

In the finite volume the corresponding momenta are quantized in units of $2\pi/L$. The Euclidean partition function for the χPT,

$$Z(V, \mathcal{M}) = \int [dU] \exp\left(-\int_V d^4x\, \mathcal{L}[U]\right) , \qquad (2.44)$$

involves three energy scales: Λ_{QCD}, $\mathcal{M}$ and $1/L$ or $p = 2\pi n/L$.

In the chiral expansion, $U = \exp(i\sqrt{2}\eta(x)/F_\pi)$ is expanded around the classical solution

$$U(x) = 1 + i\sqrt{2}\eta(x)/F_\pi + \dots . \qquad (2.45)$$

The field $\eta(x)$ belongs to the Lie algebra of $SU(3)$ and it describes fields of the pseudo-scalar mesons.

Inserting Eq. (2.45) in the expression for the Lagrangian (2.37) and integrating over the volume we arrive at the action

$$\int_V d^4x\, \mathcal{L}^{(2)} = -\frac{1}{2} N_f F_\pi{}^2 m_\pi^2 V + \frac{1}{2} \int_V d^4x\, \mathrm{Tr}\left((\partial_\mu \eta)^2 + m_\pi^2 \eta^2\right) . \qquad (2.46)$$

Since $\eta(x)$ is defined on the torus $V = L^4$ we may expand it in terms of periodic plane waves

$$\begin{aligned}
\eta(x) &= \sum_{n_1=-\infty}^{\infty} \cdots \sum_{n_4=-\infty}^{\infty} q_n\, u_n(x) + h.c. , \quad n = (n_1, \dots, n_4) , \\
u_n(x) &= \exp(2\pi i\, nx/L) ,
\end{aligned} \qquad (2.47)$$

where h.c. represents the Hermitian conjugate of the preceding term. Inserting this expression in Eq. (2.46) we see that the zero mode degrees of freedom q_0 of course do not appear in the kinetic term. This fact manifests itself also in the expression for the pion propagator which develops a pole,

$$G(x - y) = \frac{u_0(x)\, u_0(y)^*}{m_\pi^2\, V} + \dots \qquad (2.48)$$

So now one can distinguish several cases. If the linear size L is much larger than the Compton wavelength of the pions, $1/m_\pi$, then the system hardly feels the finite volume and we have the usual chiral expansion. As the size of the box or the pion mass becomes smaller, finite size effects become significant, but provided that $m_\pi L \geq 1$, ordinary perturbation theory is still applicable. This is the so-called *p-expansion* [17] with the counting rules

$$\frac{|q_n|}{F_\pi} \sim \frac{m_\pi}{\Lambda_{QCD}} \sim \frac{p}{\Lambda_{QCD}} \sim \frac{1}{LF_\pi} .$$

If the chiral limit is approached further in such a way that the Compton wavelength of the pion is larger than the box size ($L < 1/m_\pi$), the conventional p-expansion eventually breaks down due to the propagation of pions with zero momenta [17]. Indeed, according to Eq. (2.48) the pion propagator contains a pole. Therefore in order to arrive at a representation which would be valid in this regime of small quark masses (or lengths L) one needs to reorder the chiral perturbation series by summing graphs which involve an arbitrary number of zero mode propagators.

An appropriate expansion for this regime is the so-called ϵ-*expansion*, in which [17–23]

$$\frac{m_\pi}{\Lambda_{QCD}} \sim \frac{p^2}{\Lambda_{QCD}^2} \sim \frac{1}{L^2 F_\pi^2} \sim \epsilon^2 \ .$$

Note that Σ and F_π, as well as other low energy constants, appearing in this counting scheme are those of the infinite volume. Using Eq. (2.43) the above relation implies for the ϵ–regime

$$m_\pi < \frac{1}{L} \ll 4\pi F_\pi \ .$$

The difficulty in this regime comes from the fact that the zero modes have to be accounted for exactly, while the chiral perturbation theory applies to the non-zero mode integration, since $q_p^2 \sim O(\epsilon^2)$ for $|p| \neq 0$. One treats the zero modes of the pion as a collective coordinate by factorizing $U(x)$ into a constant collective field U_0 and the pion fluctuations $\xi(x)$,

$$U(x) \ = \ U_0 \exp i \left(\frac{\sqrt{2}\xi(x)}{F_\pi} \right) \ . \tag{2.49}$$

The field $\xi(x)$ can be represented in terms of the plane waves with momenta $|p|$ larger than zero. U_0 is a $SU(N_f)$ matrix independent of x.

To leading order, the partition function reads

$$\mathcal{Z}(\theta, m_q) = \int_{SU(N_f)} d\xi dU_0 \exp \frac{1}{2} \int_V d^4x \, \mathrm{Tr}\,(\partial_\mu \xi(x) \partial_\mu \xi(x)) \times \tag{2.50}$$

$$\exp \frac{\Sigma V}{2} \mathrm{Tr}\,\left(\mathcal{M}e^{i\theta/N_f}U_0 + h.c.\right) \ ,$$
$$\mathcal{M} = \mathrm{diag}(m_1, \ldots, m_{N_f}) \ .$$

It is also interesting to consider expectation values in sectors of fixed topology [24]. Fourier-transforming in θ and dropping the non-zero mode

contributions, we obtain

$$\mathcal{Z}_\nu(m_1,\ldots,m_{N_f}) \;=\; \int_{SU(N_f)} dU_0 \,(\det U_0)^\nu \exp\left(\frac{\Sigma V}{2}\mathrm{Tr}\left(\mathcal{M}U_0 + U_0^\dagger \mathcal{M}^\dagger\right)\right)$$

or for the degenerate quark masses with $\mathcal{M} = \mathrm{diag}(m_q,\ldots,m_q)$

$$\mathcal{Z}_\nu(m_q) = \int_{SU(N_f)} dU_0 \,(\det U_0)^\nu \exp\left(\frac{m_q\Sigma V}{2}\mathrm{Tr}\left(U_0 + U_0^\dagger\right)\right) . \tag{2.51}$$

If $F_\pi L \gg 1$, the p- and ϵ-expansions should match in the range of quark masses such that $m_\pi L \sim 1$. In this regime $m_q\Sigma V \sim (F_\pi L)^2(m_\pi L)^2 \gg 1$, so the results in the ϵ-expansion should reproduce those of the p-expansion in the limit of large $m_q\Sigma V$.

2.3.3 Quenched χPT: first order expressions for the axial-vector correlation function

We start by writing down the expression for the axial-vector current,

$$\mathcal{A}_\mu^a(t,\vec{x}) = \bar{\psi}(t,\vec{x})\gamma_5\gamma_\mu T^a\psi(t,\vec{x}) . \tag{2.52}$$

The two-point correlation function is as usually given by the expectation value

$$\langle\mathcal{A}_\mu^a(x)\mathcal{A}_\nu^b(y)\rangle = \frac{\int[DA_\mu][D\psi][D\bar{\psi}]\mathcal{A}_\mu^a(x)\mathcal{A}_\nu^b(y)e^{-S_{\mathrm{QCD}}+i\theta\nu[A]}}{Z^{\mathrm{QCD}}(m_q,\theta)} \tag{2.53}$$

or in terms of the propagator $(\mathcal{D}+m_q)^{-1}(x,y)$,

$$\langle\mathcal{A}_\mu^a(x)\mathcal{A}_\nu^b(y)\rangle =$$
$$-\mathrm{Tr}(T^aT^b)\langle\mathrm{Tr}\left[\gamma_5\gamma_\mu(\mathcal{D}+m_q)^{-1}(x,y)\gamma_5\gamma_\nu(\mathcal{D}+m_q)^{-1}(y,x)\right]\rangle . \tag{2.54}$$

This expression can be obtained using the partition function for QCD in the presence of auxiliary external fields $a_\mu(x)$, the so-called generating functional. For the sake of the following discussion we will also add auxiliary fields for the pseudo-scalar density $P(x) = \bar{\psi}i\gamma_5\psi$,

$$Z(a_\mu, P) = \int DA_\mu D\psi D\bar{\psi} \exp\left[-S_{\mathrm{QCD}} + \int_V dx\,\bar{\psi}(\gamma_\mu\gamma_5 a_\mu + i\gamma_5 P)\psi\right] . \tag{2.55}$$

If we compute the second functional derivative of the partition function $Z(a_\mu, P)$ with respect to the axial current a_μ and put a_μ and P to zero

afterwards, we recover the expression (2.53) for the axial current correlation function. This new partition function (2.55) is now subject to its low energy approximation, i.e. one integrates out the quark degrees of freedom leaving only the mesons. The leading order expression of the chiral Lagrangian of the low energy effective theory in the presence of a_μ and P takes the form

$$
\begin{aligned}
\mathcal{L}^{(2)}[U, a_\mu, P] &= \frac{F_\pi^2}{4} \mathrm{Tr}\left(\nabla_\mu U^\dagger \nabla_\mu U\right) - \\
&\quad - \frac{\Sigma}{2} \mathrm{Tr}\left[e^{i\frac{\theta}{N_f}}(\mathcal{M} + iP(x))U^\dagger + Ue^{-i\frac{\theta}{N_f}}(\mathcal{M}^\dagger - iP^\dagger(x))\right],
\end{aligned}
\tag{2.56}
$$

where

$$
\nabla_\mu U = \partial_\mu U - ia_\mu U - iUa_\mu , \quad \mathcal{M} = \mathrm{diag}(m_q, \ldots, m_q) .
$$

We see that the partial derivatives in the expression (2.37) were promoted to some kind of covariant derivatives. Note that $P(x)$ is assumed to be of the same order as m_q in the chiral expansion, whereas $a_\mu(x)$ is counted as the pion momenta p .

Now from this expression one can construct the partition function. Taking then two functional derivatives with respect to the axial current $a_\mu(x)$ or two functional derivatives with respect to the pseudo-scalar density $P(x)$ we obtain the expression for the axial correlation function and pseudo-scalar correlation function in χPT. As far as full QCD is concerned, all two-point functions had been calculated before for the ϵ-regime in Ref. [21].

The QCD partition function (2.9) includes a fermion determinant. It accounts for the creation and annihilation of the quark-antiquark pairs. It turned out that in computer simulations the calculation of the determinant slows down the updating of the gauge fields tremendously since one has to recompute it for every gauge configuration. Therefore a crude approximation to QCD that goes under the name of *quenched approximation* is used in part of the contemporary simulations. It neglects the fermion determinant in the QCD partition function (2.9) and in the expectation values of the observables calculated with it. Despite the crudeness of the approximation it is useful to employ it as an estimate for the observables of interest, keeping in mind the systematic uncertainties of about $10 - 15\%$ [25, 26]. The latter depends of course on the observable of interest. We aim, however, at the quenched formulation of the chiral perturbation theory, i.e. a low energy effective theory where the quark loops were eliminated on the level of QCD. In order to get rid of the quark loops one can add quarks with bosonic statistics to the fermion part of the QCD Lagrangian (2.3) keeping the external currents

coupled to the quarks with the proper statistics. The latter are called the "valence" quarks. This results in the cancellation of the diagrams with internal loops. The corresponding partition function with the sources J_i coupled to quark bilinears is,

$$Z_{\text{SUSY}}(J_1, \ldots, J_{N_v}) = \int [DA_\mu] \frac{\prod_{i=1}^{N_v} \det(\mathcal{D} + m_q + J_i)}{\det(\mathcal{D} + m_q)^{N_v}} e^{-S_{\text{YM}}[A] + i\theta\nu[A]} \ . \tag{2.57}$$

The $2N_v$ quarks (N_v with usual fermionic statistics and N_v additional with bosonic statistics) lie in the fundamental representation of the graded group $SU(N_v|N_v)$. For massless quarks, the corresponding full QCD Lagrangian exhibits a graded symmetry $SU(N_v|N_v)_L \otimes SU(N_v|N_v)_R \otimes U(1)_V$ that is assumed to be spontaneously broken down to $SU(N_v|N_v)_V \otimes U(1)_V$. This is the so–called "supersymmetric" formulation of quenched QCD [27]. Using it as a starting point one obtains a low energy theory without quark loops.

The "supersymmetric" chiral Lagrangian in the leading order is given by

$$\mathcal{L}_{\text{SUSY}}^{(2)} = \frac{F_\pi^2}{4} \text{Str} \left(\partial_\mu U^{-1} \partial_\mu U \right) - \frac{m_q \Sigma}{2} \text{Str} \left(U_\theta U + U^{-1} U_\theta^{-1} \right) + \tag{2.58}$$

$$+ \frac{m_0^2}{2N_c} \Phi_0^2 + \frac{\alpha}{2N_c} \partial_\mu \Phi_0(x) \partial^\mu \Phi_0(x) \ ,$$

where Str denotes the "supertrace", $\Phi_0 \equiv \frac{F_\pi}{2} \text{Str}[-i \log(U)]$ and

$$U_\theta \equiv \exp(i\theta/N_v) I_{N_v} + \tilde{I}_{N_v} \ . \tag{2.59}$$

Here, I_{N_v} is the identity matrix in the fermion–fermion block of "physical" Goldstone bosons and zero otherwise, while $\tilde{I}_{N_v}$ is the identity in the boson–boson block and zero elsewhere. Apart from the familiar low energy constants F_π and Σ — which now, however, take their quenched values — we have also two new parameters m_0 and α, which are artifacts of the quenched approximation.

We note that there is also another method to formulate the quenched χPT — the replica method [28]. Here one considers N_v valence quarks to be part of N quarks in total. Considering now N as a parameter and sending it to 0 we obtain the replica limit. The equivalence of the two methods was verified at the perturbative level of the chiral Lagrangian [28].

An important difference of quenched χPT from the full theory is the unavoidable presence of a singlet scalar field Φ_0, which cannot be decoupled in this case. The singularities of the propagator of the Φ_0 field are responsible for the quenching artifacts. Also the formulation of the counting rules for the quenched χPT becomes more involved. These issues, as well as the two-point

functions for the ϵ– regime in the quenched approximation, were addressed in Refs. [29, 30].

For the purpose of this thesis we consider the expression for the axial correlation function with one flavor. We define the bare axial current with one flavor at momentum $\vec{p} = \vec{0}$ and Euclidean time t,

$$\mathcal{A}_\mu(t) = \sum_{\vec{x}} \bar{\psi}(t, \vec{x})\gamma_5\gamma_\mu\psi(t, \vec{x}) . \tag{2.60}$$

The formula for the axial correlation function in a volume $L^3 \times T$, to the first order in quenched χPT, reads [29][1]

$$
\begin{aligned}
\langle \mathcal{A}_0(t)\,\mathcal{A}_0(0)\rangle_\nu &= 2 \cdot \left(\frac{F_\pi^2}{T} + 2m_q\Sigma_{|\nu|}(z_q)T \cdot h_1(\tau) \right) , \\
h_1(\tau) &= \frac{1}{2}\left(\tau^2 - \tau + \frac{1}{6} \right), \qquad \tau = \frac{t}{T} , \\
\Sigma_\nu(z_q) &= \Sigma\left(z_q\left[I_\nu(z_q)K_\nu(z_q) + I_{\nu+1}(z_q)K_{\nu-1}(z_q)\right] + \frac{\nu}{z_q} \right)
\end{aligned}
\tag{2.61}
$$

I_ν and K_ν are modified Bessel functions, $z_q = m_q\Sigma V$, ν is again the topological charge, and h_1 is a purely kinematic function. The latter shows that this correlation function is given by a parabola in t with its minimum at $T/2$. This behavior is qualitatively different from the infinite volume, where the correlations decay exponentially (resp. as a cosh function in a periodic volume). However, the small and the infinite volume have in common that in both cases the quenched axial correlation function to the first order only depends on the low energy constants F_π and Σ.

2.3.4 Zero mode contributions to the pseudo-scalar correlation function

We start off by writing the expressions of the pseudo-scalar densities $\mathcal{P}^0(x), \mathcal{P}^a(x)$

$$
\begin{aligned}
\mathcal{P}^0 &= \bar{\psi}i\gamma_5\psi , \\
\mathcal{P}^a &= \bar{\psi}T^a i\gamma_5\psi , \quad a = 1, \ldots, N_f^2 - 1 ,
\end{aligned}
\tag{2.62}
$$

where T^a are generators of the group $SU(N_f)$ and a runs from 1 to $N_f^2 - 1$. Let I, J run from 0 to $N_f^2 - 1$ and $T^0 = 1$, then the correlation function

---

[1]We have an extra factor of 2 compared to Ref. [29] because this definition of the current is considered only for one flavor.

$\langle \mathcal{P}^I(x)\mathcal{P}^J(y)\rangle_\nu$ takes the general form

$$\langle \mathcal{P}^I(x)\mathcal{P}^J(y)\rangle_\nu = -\mathrm{Tr}(T^I T^J)\,\mathcal{P}_1(x,y) + \mathrm{Tr}(T^I)\,\mathrm{Tr}(T^J)\,\mathcal{P}_2(x,y)\ . \quad (2.63)$$

$\mathcal{P}_1$ and $\mathcal{P}_2$ are the connected and disconnected parts of the correlation function,

$$
\begin{aligned}
\mathcal{P}_1(x,y) &= \mathrm{Tr}[i\gamma_5(\mathcal{D}+m_q)^{-1}(x,y)\,i\gamma_5(\mathcal{D}+m_q)^{-1}(y,x)]\ , \\
\mathcal{P}_2(x,y) &= \mathrm{Tr}[i\gamma_5(\mathcal{D}+m_q)^{-1}(x,x)]\,\mathrm{Tr}[i\gamma_5(\mathcal{D}+m_q)^{-1}(y,y)]\ , \quad (2.64)
\end{aligned}
$$

where $\mathcal{D}^{-1}(x,y)$ is the propagator of the Dirac operator. The correlation function can be computed from the generating functional which we discussed in the previous Subsection. Now one has to calculate two derivatives of the generating functional with respect to the auxiliary pseudo-scalar field $P(x)$ introduced in Eq. (2.55) and put all the auxiliary fields to zero at the end. Applying the same technique to the generating functional of the low energy effective theory we obtain the corresponding pseudo-scalar correlation function in the quenched χPT (qχPT).

We consider the pseudo-scalar correlation function for the definite topological sector ν. Application of the spectral representation of the quark propagator to the pseudo-scalar correlation function was first considered in Ref. [1]. By employing the spectral representation of the quark propagator, it is clear that the correlator $\langle \mathcal{P}^I(x)\mathcal{P}^J(y)\rangle_\nu$ contains a pole in m_q^2, due to the exact zero modes. Its residue is

$$\lim_{m_q\to 0}(m_q V)^2\langle \mathcal{P}^I(x)\mathcal{P}^J(0)\rangle_\nu = \mathrm{Tr}[T^I T^J]\,\mathcal{C}_{|\nu|}(x) + \mathrm{Tr}[T^I]\mathrm{Tr}[T^J]\tilde{\mathcal{C}}_{|\nu|}(x)\ , \quad (2.65)$$

where

$$\mathcal{C}_{|\nu|}(x-y) = \left\langle \sum_{i,j=1}^{K} v_j^\dagger(x)v_i(x)v_i^\dagger(y)v_j(y)\right\rangle_\nu\ , \quad (2.66)$$

$$\tilde{\mathcal{C}}_{|\nu|}(x-y) = -\left\langle \sum_{i=1}^{K} v_i^\dagger(x)v_i(x)\sum_{j=1}^{K} v_j^\dagger(y)v_j(y)\right\rangle_\nu\ , \quad (2.67)$$

and the sums are over the set of $K = N_+ + N_-$ zero modes v_i of the Dirac operator, $\mathcal{D}v_i = 0\ ,\forall\ i = 1,\ldots,K$. We recall that N_+ zero modes have positive chirality while N_- have negative chirality. The modes are normalized so that $\int \mathrm{d}^4 x\, v_i^\dagger(x)v_i(x) = V$.

It is important to note that in writing Eqs. (2.65)—(2.67) it is assumed that poles arise only from exact zero modes, i.e. that taking the limit $m_q \to 0$ and performing the average over the full space of configurations commute. At

fixed volume the only potential danger arises from the average distribution of eigenvalues near zero; this assumption holds if the density of eigenvalues vanishes for gauge configurations at fixed non-zero topological charge. In χPT, as well as in random matrix theory (RMT) [31–34], which will be discussed in the next Section, the densities behave as $\rho_\nu(\lambda) \sim \lambda^{(2|\nu|+1+2N_f)}$, and no contribution from the non-zero modes is thus expected in the considered observables.

The zero mode contribution to the pseudo-scalar correlation functions $\langle P^I(x)P^I(y)\rangle_\nu$ at next-to-next-to-leading order (NNLO) in the ϵ–regime for a given topological sector ν was computed in Ref. [1], both for full and quenched QCD. In this computation the chiral expansion in momentum and mass was combined with the $1/N_c$ expansion

$$p^2 \sim \frac{1}{N_c} \sim \epsilon^2 \ . \tag{2.68}$$

The corresponding Lagrangian for the quenched χPT to the NNLO reads

$$
\begin{aligned}
\mathcal{L}^{(2)}_{q\chi PT} &= \frac{F_\pi^2}{4}\mathrm{Str}\left[\partial_\mu U \partial_\mu U^{-1}\right] - \frac{m_q\Sigma}{2}\mathrm{Str}\left[U_\theta U + U^{-1}U_\theta^{-1}\right] - \\
&- im_q K \Phi_0 \mathrm{Str}\left[U_\theta U - U^{-1}U_\theta^{-1}\right] + \frac{m_0^2}{2N_c}\Phi_0^2 + \frac{\alpha}{2N_c}(\partial_\mu\Phi_0)^2
\end{aligned} \tag{2.69}
$$

It has an additional low energy constant K coupling the singlet scalar field Φ_0 to the pseudo-scalar meson field U.

In this particular expansion the mass m_0 was chosen to be a small parameter of order ϵ, in contrast to the standard counting where it is treated to be of order $\mathcal{O}(1)$. It is also assumed that F_π, Σ and K scale as

$$F_\pi^2 = \bar{F}_\pi^2 N_c, \quad \Sigma = \bar{\Sigma}N_c, \quad K = \frac{\bar{K}}{\sqrt{N_c}} \ . \tag{2.70}$$

This implies that $\mathcal{O}(\bar{F}_\pi) \sim \mathcal{O}(\bar{\Sigma}) \sim 1$. Given the fact that $\mathcal{O}(m_q\Sigma V) \sim 1$ we are led to the relation

$$m_q \sim \epsilon^6 \ . \tag{2.71}$$

It is further assumed that $\mathcal{O}(\alpha) \sim \mathcal{O}(\bar{K}) \sim 1$ and $\mathcal{O}(m_0^2) \sim \epsilon^2$. In this framework the pseudo-scalar density P^I corresponding to $\mathcal{P}^I$ in QCD takes the form

$$P^I = i\frac{\Sigma}{2}\mathrm{Str}\left[T^I\left(U_\theta U - U^{-1}U_\theta^{-1}\right)\right] - K\Phi_0\mathrm{Str}\left[T^I\left(U_\theta U + U^{-1}U_\theta^{-1}\right)\right] \ . \tag{2.72}$$

The authors of the Ref. [1] worked out the expressions for the first derivative of the pseudo-scalar as well as the scalar correlators at non-zero time separations in quenched as well as in full χPT. It was pointed out that taking the

first derivative helps to get rid of the NNLO Gasser-Leutwyler coefficients for the expressions in full χPT,

$$
\begin{aligned}
\frac{1}{2}C'_{|\nu|}(t) &= \lim_{m_q \to 0}(m_q V)^2 \frac{\mathrm{d}}{\mathrm{d}t}\int \mathrm{d}^3 x\,\langle P^a(x)P^a(0)\rangle_\nu\,, \\
N_f\,C'_{|\nu|}(t) + N_f^2\,\tilde{C}'_{|\nu|}(t) &= \lim_{m_q \to 0}(m_q V)^2 \frac{\mathrm{d}}{\mathrm{d}t}\int \mathrm{d}^3 x\,\langle P^0(x)P^0(0)\rangle_\nu\,. \quad (2.73)
\end{aligned}
$$

$C_{|\nu|}(x)$ and $\tilde{C}_{|\nu|}(x)$ are quantities which correspond to $\mathcal{C}_{|\nu|}(x)$ and $\tilde{\mathcal{C}}_{|\nu|}(x)$, but calculated in the framework of χPT. If we define the volume average $\mathcal{C}_{|\nu|}(t) = \int d^3 x\,\mathcal{C}_{|\nu|}(x)$ and $\tilde{\mathcal{C}}_{|\nu|}(t) = \int d^3 x\,\tilde{\mathcal{C}}_{|\nu|}(x)$, then at large time t

$$
\mathcal{C}_{|\nu|}(t) = C_{|\nu|}(t)\,, \quad \tilde{\mathcal{C}}_{|\nu|}(t) = \tilde{C}_{|\nu|}(t)\,, \quad (2.74)
$$

which represent the matching of the results in quenched QCD and in quenched χPT.

In the following we redefine α as

$$
\frac{\alpha}{2N_c} \to \frac{\alpha}{2N_c} - \frac{2KF_\pi}{\Sigma}\,. \quad (2.75)
$$

This allows us to simplify the resulting expressions for the zero mode contributions to the pseudo-scalar correlator in a way that only two low energy constants will appear instead of the combination of K, F_π, Σ and α. The expressions for qχPT in the volume $V = L^3 T$ read

$$
\begin{aligned}
F_\pi^2 C'_{|\nu|}(t) &= 2|\nu|\Bigg[|\nu|h'_1(\tau) + \left(\frac{\alpha}{2N_c} - \frac{\beta_1}{F_\pi^2\sqrt{V}}\right)h'_1(\tau) \\
&\quad + \frac{T^2}{F_\pi^2 V}\left(2\nu^2 + \frac{7}{3} - 2\langle\nu^2\rangle\right)h'_2(\tau) + \frac{T^2}{2F_\pi^2 V}h'_3(\tau)\Bigg]\,, \quad (2.76) \\
F_\pi^2 \tilde{C}'_{|\nu|}(t) &= -2|\nu|\Bigg[h'_1(\tau) + |\nu|\left(\frac{\alpha}{2N_c} - \frac{\beta_1}{F_\pi^2\sqrt{V}}\right)h'_1(\tau) \\
&\quad + \frac{T^2}{F_\pi^2 V}\left(\frac{13}{3}|\nu| - 2|\nu|\langle\nu^2\rangle\right)h'_2(\tau) + |\nu|\frac{T^2}{2F_\pi^2 V}h'_3(\tau)\Bigg]\,, \quad (2.77)
\end{aligned}
$$

where $h_1(\tau)$ and τ were defined in Eq. (2.61) and $h_2(\tau) = \frac{1}{24}\left[\tau^2(\tau-1)^2 - \frac{1}{30}\right]$. β_1 is a geometrical shape coefficient depending on the form of the volume. β_1 as well as h_1, h_2 and h_3 were introduced in Ref. [20] in context of computation of the two-point functions in the σ-model at finite

volume. $h_3(\tau)$ is defined by

$$
\begin{aligned}
h_3(\tau) &= [h_1(\tau)]^2 + {\sum_{\vec{n}}}' \left[\frac{\cosh(|\vec{p}|T(\tau - 1/2))}{2|\vec{p}|T\sinh(|\vec{p}|/2)} \right]^2 , \\
|\vec{p}| &= \frac{2\pi}{L} \left[\sum_{i=1}^{3} n_i^2 \right]^{\frac{1}{2}} ,
\end{aligned} \tag{2.78}
$$

where the prime in the sum indicates that the zero mode term, with $\vec{n} = \vec{0}$, is left out. The expectation value $\langle \nu^2 \rangle$ is related to the mass m_0 in analogy to the Witten-Veneziano formula which will be discussed in Chapter 7.

2.4   Chiral random matrix theory

The appearance of the theory of random matrices in the mathematical literature goes back to 1928 and was first applied to physics in the context of nuclear resonances by Wigner almost 50 years ago. At that time, theoretical approaches such as the shell model had proven to be very successful in describing the low-lying excitations of complex nuclei. However, highly excited resonances, which can be observed experimentally by neutron scattering, could not be described by the microscopic theory. The problem is generic: for any complex quantum system containing many degrees of freedom with complicated dynamics, it is very hard, if not impossible, to obtain exact results for the energy levels far above the ground state of the system.

Even though the highly excited states cannot yet be predicted individually, one can try to find in the experimental data some generic statistical features that can be described theoretically. This is where RMT comes in. It aims at a statistical description of the energy levels of the system using only basic symmetry considerations as its theoretical input.

In the following discussion we would like to restrict our attention to the case of QCD. One can write a Hamilton operator for QCD in matrix form. Since QCD is not solved analytically one may follow an approach whereby we assume that all interactions which are consistent with the symmetries of the system are equally likely. This means that we replace the Hamilton matrix by a matrix which is compatible with the global symmetries of QCD and with elements which become now uncorrelated and distributed according to some distribution of random numbers. To obtain definite results, observables such as the level density must then be averaged over the random matrix elements. This defines a statistical theory of energy levels, which is known as RMT.

In this Section we will discuss the *chiral Random Matrix Theory* (χRMT). The structure of the χRMT partition function is inspired by the instanton

gas model. Although it is not necessary, it is instructive to think of the field configurations as a superposition of N_+ instantons and N_- anti-instantons. Each isolated instanton or anti-instanton has exactly one fermionic zero mode with a definite chirality. In total we have $\nu = N_+ - N_-$ for the index of the gauge field configuration. At finite separation of instantons and anti-instantons the remaining modes are no longer exact zero modes of the Dirac equation and give rise to nonzero overlap matrix elements in the submatrix W of the Dirac operator [35].

A model describing the zero mode part of the QCD partition function in the Euclidean volume V is defined by [36]

$$Z(m_f, \theta) = \sum_{N \geq 0} \mu(N) \sum_{N_+=0}^{N} \begin{pmatrix} N \\ N_+ \end{pmatrix} e^{i\theta(2N_+ - N)} \int DW \, P(W) \prod_{f=1}^{N_f} \det \begin{pmatrix} m_f & iW \\ iW^\dagger & m_f \end{pmatrix} .$$
(2.79)

$N = N_+ + N_-$ is the number of zero modes, and the matrix W is a $N_+ \times N_-$ matrix. The integration measure DW is given by the Haar measure. The binomial factor arises since zero modes of each chirality are treated as independently distributed identical particles. $\mu(N)$ is the distribution function of the total number of zero modes. $P(W)$ denotes the probability distribution for field configurations. The structure of the overlap matrix, with off-diagonal blocks W and $W^\dagger$ and diagonal blocks equal to the quark masses m_f times the identity, is dictated by the chirality of the zero modes, see Eq. (2.19). The density $\overline{N}/V$ of the total number of zero modes is kept fixed as V changes. As in the instanton liquid approximation to the QCD partition function [37–39], it is considered to be an external parameter.

We now replace the average over all gauge field configurations with an average over Gaussian distributed overlap matrix elements with the distribution function

$$P(W) = \exp\left(-\frac{N\Sigma^2\beta}{4}\text{Tr}(WW^\dagger)\right) .$$
(2.80)

β is the so-called Dyson index which is defined as the number of independent variables per matrix element. To this end the matrix elements of W can be either real [$\beta = 1$, chiral Gaussian Orthogonal Ensemble (χGOE)], complex [$\beta = 2$, chiral Gaussian Unitary Ensemble (χGUE)], or quaternion real [$\beta = 4$, chiral Gaussian Symplectic Ensemble (χGSE)]. In the latter case, the eigenvalues of $\mathcal{D}$ are doubly degenerate, and the use of Majorana fermions is implemented by replacing the determinant by its square root.

We will restrict ourselves to the χRMT partition function in a specific

topological sector,

$$Z_{N_f,\nu}^{(\beta)}(m_1, \ldots, m_{N_f}) = \int DW \prod_{f=1}^{N_f} \det(\mathcal{D} + m_f) e^{-\frac{N\Sigma^2\beta}{4} \text{Tr}\,(W^\dagger W)} \,, \qquad (2.81)$$

$$\mathcal{D} = \begin{pmatrix} 0 & iW \\ iW^\dagger & 0 \end{pmatrix} \,. \qquad (2.82)$$

The parameter Σ will be later identified with the chiral condensate and N with the spacetime volume. For large N we assume that $|\nu|$ does not exceed $\sqrt{N}$ so that, to a good approximation, $N_+ = N/2$ for large N. These assumptions motivated by the instanton liquid model are, however, not fulfilled in the lattice simulations with the Ginsparg-Wilson fermions which are the subject of the thesis. In fact one observes zero modes either with positive or negative chirality. Therefore an aim of this work is also to prove the viability of the predictions by the RMT in our quenched QCD simulations.

This model inherits the following symmetries of the QCD partition function:

- The $U_A(1)$ symmetry. All eigenvalues of the random matrix Dirac operator occur in pairs $\pm i\lambda_n$, or they are zero.

- The topological structure of the QCD partition function. The Dirac matrix $\mathcal{D}$ has index $\nu = N_+ - N_-$. This identifies ν as the topological charge of the model.

- The flavor symmetry, which is the same as in QCD. For $\beta = 2$ it is $SU(N_f) \otimes SU(N_f)$, for $\beta = 1$ it is $SU(2N_f)$, and for $\beta = 4$ it is $SU(N_f)$ (two Majorana flavors count as one Dirac flavor).

- The chiral symmetry, which is broken spontaneously with a chiral condensate given by
$$\Sigma = \lim_{m_f \to 0} \lim_{N \to \infty} \pi\rho(0)/N \,. \qquad (2.83)$$

(N is interpreted as the dimensionless volume of spacetime.) The symmetry-breaking pattern is [40] $SU(N_f) \otimes SU(N_f) \to SU(N_f)$, $SU(2N_f) \to Sp(2N_f)$, and $SU(N_f) \to O(N_f)$ for $\beta = 2$, 1, and 4, respectively — the same as in QCD [41–43].

The chiral ensembles are, however, only a part of a larger classification scheme that also includes ensembles for the description of disordered superconductors [44]. In total, 10 different families of random matrix ensembles have been identified. They correspond one-to-one to the Cartan

classification of symmetric spaces.

We consider the spectral representation of the χRMT partition function. The partition function (2.81) is invariant under the transformation

$$W \rightarrow U^\dagger W V \; , \tag{2.84}$$

where the $n \times n$ matrix U and the $m \times m$ matrix V are orthogonal matrices for $\beta = 1$, unitary matrices for $\beta = 2$, and symplectic matrices for $\beta = 4$. Using this property the matrix W can be rewritten as

$$W = U^\dagger \Lambda V \; . \tag{2.85}$$

Here, Λ is a diagonal matrix with real positive matrix elements λ_k. In terms of the eigenvalues, the partition function (2.81) is given by

$$Z_{N_f,\nu}^{(\beta)}(m_1, \ldots, m_{N_f}) = \int \prod_k d\lambda_k \, |\Delta(\lambda^2)|^\beta \prod_k \lambda_k^{2N_f + \beta|\nu| + \beta - 1} e^{-\frac{N\Sigma^2\beta}{4}\lambda_k^2} \prod_f m_f^{|\nu|}(\lambda_k^2 + m_f^2) \; , \tag{2.86}$$

where the Vandermonde determinant Δ is defined by

$$\Delta(\lambda^2) = \prod_{k<l}(\lambda_k^2 - \lambda_l^2) \; . \tag{2.87}$$

In the following we will need the σ model representation of the χRMT partition function [36, 45]. One arrives at it by writing the fermion determinant of Eq. (2.81) as a Grassmann integral. Then one averages over the Gaussian distribution function. The resulting expression is subject to the saddle point approximation in the large N limit. We give the expression for the partition function at $\beta = 2$

$$\begin{aligned} Z_{N_f,\nu}^{(2)}(m_1, \ldots, m_{N_f}) &= \int_{U \in \mathrm{U}(N_f)} DU \, (\det U)^\nu \, e^{\frac{N\Sigma}{2}\mathrm{Tr}\,(\mathcal{M}U + \mathcal{M}^\dagger U^{-1})} \; , \\ \mathcal{M} &= \mathrm{diag}(m_1, \ldots, m_{N_f}) \; . \end{aligned} \tag{2.88}$$

One can see that the partition function for the χRMT in the large N limit coincides with the leading order expression of the χPT partition function in the ϵ– regime characterized by Eq. (2.51) [36]. This fact leads to profound consequences for the observables calculated in the ϵ–regime. We are going to discuss the applications for the so-called microscopic eigenvalue density in the next Subsection.

2.4.1 Microscopic spectral properties

We start off by discussing the Leutwyler-Smilga sum rules [24]. The microscopic spectral density of the Dirac eigenvalues arises naturally from them. The Leutwyler-Smilga sum rules are obtained by expanding the partition function $\mathcal{Z}_\nu(m_f)$ in powers of m_f for the expression in the ϵ–regime (2.51), and $Z_\nu^{QCD}(m_f)$ given in Eq. (2.10), and then equating the coefficients. We take the topological sector to be $\nu = 0$. Comparing coefficients at $\mathcal{O}(m_f^2)$ we obtain

$$\langle \sum_{\lambda_k > 0} \frac{1}{\lambda_k^2} \rangle = \frac{\Sigma^2 V^2}{4N_f} \ , \tag{2.89}$$

where the sum is restricted to nonzero positive eigenvalues. The Leutwyler-Smilga sum rules can be expressed as an integral over the eigenvalue spectral density $\rho(\lambda)$ and spectral correlation functions,

$$\frac{1}{V^2 \Sigma^2} \int \frac{\rho(\lambda) d\lambda}{\lambda^2} = \frac{1}{4N_f} \ . \tag{2.90}$$

If we introduce the microscopic variable z,

$$z = \lambda V \Sigma \ , \tag{2.91}$$

the integral can be rewritten as

$$\frac{1}{V\Sigma} \int \frac{\rho(\frac{z}{V\Sigma}) dz}{z^2} = \frac{1}{4N_f} \ . \tag{2.92}$$

Also according to the Banks-Casher relation the small eigenvalues are spaced as

$$\Delta\lambda = \frac{1}{\rho(0)} = \frac{\pi}{V\Sigma} \ , \tag{2.93}$$

provided that $\rho(0)/V > 0$. These arguments naturally define a scale which is suitable for the study of the distribution of individual eigenvalues. For this purpose, it is convenient to define the so-called microscopic spectral density

$$\rho_s(z) = \lim_{\substack{V \to \infty \\ \Sigma V m_f \text{ fixed}}} \frac{1}{V\Sigma} \rho\left(\frac{z}{V\Sigma}\right) = \lim_{\substack{V \to \infty \\ \Sigma V m_f \text{ fixed}}} \frac{1}{V\Sigma} \sum_n \langle \delta(z - \lambda_n \Sigma V) \rangle_{\text{QCD}} \ ,$$

$$\tag{2.94}$$

where the average is taken over the QCD partition function. This limit exists if chiral symmetry is broken. Ab initio calculation of this quantity in QCD is a challenging task which requires a non-perturbative treatment and could not

be solved yet analytically. The microscopic spectral density, however, arises as a natural quantity for the χPT in a finite volume since it is defined at fixed $m_f \Sigma V$ in the dynamical case. By using the relation between the χPT at the leading order and the χRMT in the large N limit, we can reduce the problem to the calculation of the microscopic spectral density for the χRMT [31–34]. The corresponding definition of the microscopic spectral density in χRMT is given by

$$
\rho_s^{\chi\mathrm{GUE}}(x) = \lim_{\substack{N\to\infty \\ \Sigma N m_f \text{ fixed}}} \frac{1}{N\Sigma} \rho^{\chi\mathrm{GUE}}\left(\frac{x}{N\Sigma}\right) = \lim_{\substack{N\to\infty \\ \Sigma N m_f \text{ fixed}}} \sum_n \langle \delta(x - \lambda_n N\Sigma)\rangle_{\chi\mathrm{GUE}} ,
$$

(2.95)

where N is the size of the random matrix, $\langle \dots \rangle_{\chi\mathrm{GUE}}$ denotes averaging with respect to the χGUE partition function and λ_n are the eigenvalues of the random matrices. If N corresponds to the lattice volume then Σ is assumed to be taken in dimensionless units.

The conjecture is that $\rho_s(z)$ is a universal function that only depends on the global symmetries of the QCD partition function and can be therefore computed by means of the χGUE,

$$
\rho_s(z) = \rho_s^{\chi\mathrm{GUE}}(z) .
$$

(2.96)

Below we illustrate how this statement fits in the framework of χPT and χGUE:

$$
Z_\nu^{\mathrm{QCD}}(m_f) = \int_\nu DA_\mu \, e^{-S[A]} \times \quad \xrightarrow{\text{(b)}} Z_{\chi\mathrm{UE}} = \int DW \, e^{-Nv(W)} \prod_f \det(\mathcal{D} + m_f)
$$

$$
\prod_f \det(\mathcal{D} + m_f)
$$

$$
\downarrow \text{(a)} \qquad\qquad\qquad\qquad\qquad\qquad \text{(c)} \downarrow
$$

$$
Z_\nu(\mathcal{M}) = \int_{\mathrm{SU}(N_f)} DU \, (\det U)^\nu \times \quad \xleftarrow{\text{(d)}} \quad Z_{N_f,\nu}^{(2)}(m_1, \dots, m_{N_f}) =
$$

$$
e^{\frac{V\Sigma}{2} \mathrm{Tr}(\mathcal{M}U + \mathcal{M}U^\dagger)} \qquad\qquad\qquad = \int DW \, e^{-\frac{N\Sigma^2}{2}\mathrm{Tr}\, WW^\dagger} \prod_f \det(\mathcal{D} + m_f)
$$

We show the relation between the partition functions of QCD (2.9), χPT (2.51) and χRMT (2.81) with GUE.

If we formally substitute the integration over gauge fields in the QCD partition function by integration over the Dirac matrices then we come to

the formulation in terms of the random matrices W and the partition function of the chiral random unitary ensemble (link (b)). We introduce the potential

$$v(W) = \frac{1}{N}(S_{YM}[A] - \log(J)), \qquad (2.97)$$

where J is the corresponding Jacobian and N is the size of the random matrices, that can be related to the physical volume V. This reduction is, however, not well theoretically founded.

The link (a) corresponds to a reduction of the QCD partition function Z^{QCD} in the finite volume to the low energy effective theory for the soft pions, which amounts to neglecting the derivative terms in the chiral Lagrangian.

Once we have a formulation in terms of the unitary random matrices $Z_{\chi\text{UE}}$ we can apply the result of Ref. [46], where it has been proven that the microscopic spectral densities, and all microscopic spectral correlators are universal within the given classes of matrix model ensembles. Hence, the link (c) leads to the χGUE partition function.

The link (d) corresponds to the reduction of the χGUE in the large N limit to the χPT partition function for the soft pions [36].

All this pattern can be reformulated for quenched QCD. Since RMT is well defined for any number of flavors, one needs only to substitute the χPT by its quenched formulation. Also the formalism of the qχPT is known.

There is now mounting evidence that the described scenario is correct. The microscopic spectral densities, derived from large N random matrix ensembles with Gaussian weights [47–51], have been shown to consistently reproduce the exact spectral sum rules of Leutwyler and Smilga. However there is no similar analytical check for the probability distributions of the individual eigenvalues.

In particular we want to highlight the analytical results for the microscopic spectral density and the probability distributions of the individual eigenvalues. The latter were calculated in the framework of the χRMT with the Gaussian unitary chiral ensemble.

The microscopic spectral density was calculated for the χGUE, as well as for the ϵ–regime of quenched χPT. (Also some other special cases were computed in χPT which agree well with χRMT results [48–50, 52].) The microscopic spectral density in the topological sector $|\nu|$ for the χGUE reads

$$\rho_s^{(\nu)}(z) = \frac{z}{2}\left(J_{N_f+|\nu|}^2(z) - J_{N_f+|\nu|+1}(z)J_{N_f+|\nu|-1}(z)\right) + |\nu|\delta(z) , \qquad (2.98)$$

where the J's are Bessel functions. These expressions can be reassembled in

the microscopic spectral density $\rho_s(z)$,

$$\rho_s(z) = \sum_{\nu=-\infty}^{\infty} \rho_s^{(\nu)}(z), \qquad \nu = \text{topological charge} . \qquad (2.99)$$

These functions $\rho_s^{(\nu)}(z)$ can be expressed in series of distributions of the kth individual lowest eigenvalue for each topological sector. Refs. [31–34] present the general formula for the probability distributions of the individual eigenvalues $\rho_k^{(\nu)}(z)$ calculated for the χGUE,

$$\rho_s^{(\nu)}(z) = \sum_{k \geq 1} \rho_k^{(\nu)}(z) + |\nu|\delta(z) , \qquad (2.100)$$

where the sum runs over the non-zero modes. The distribution of the lowest eigenvalue of the Dirac operator for an arbitrary topological sector and $N_f = 0$ reads

$$\rho_1^{(\nu)}(z) = \frac{z}{2}\mathrm{e}^{-z^2/4} \det[I_{2+i-j}(z)]_{i,j=1,\dots,|\nu|} . \qquad (2.101)$$

The predictions for the lowest eigenvalue at $|\nu| = 0$, 1 and 2 are depicted in Figure 2.1. We see in particular that the density peak moves to larger values of z as $|\nu|$ increases.
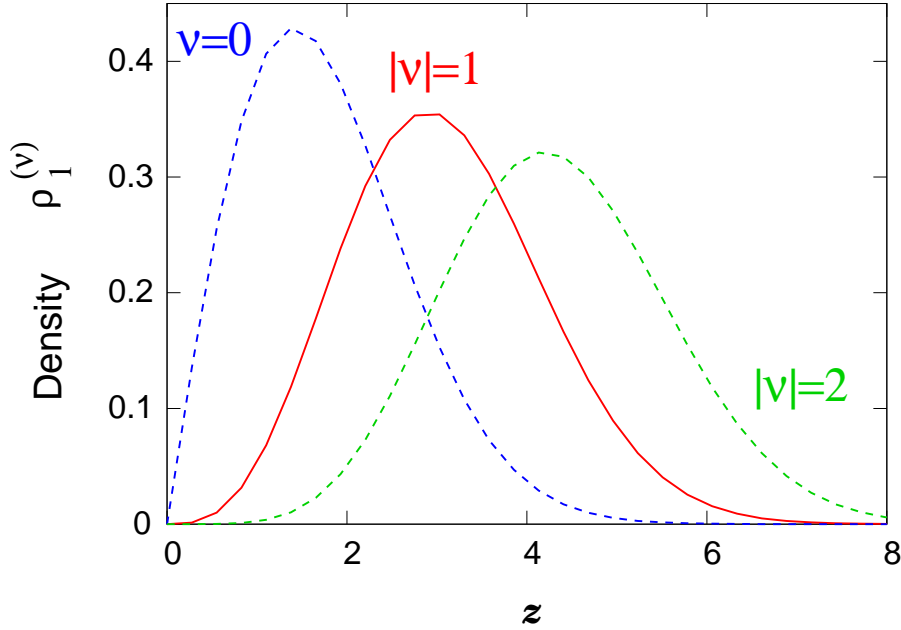
Figure 2.1: The distributions for the lowest eigenvalue at $|\nu| = 0$, 1 and 2, as predicted by χRMT in Eq. (2.101).

2.4.2 Bulk eigenvalues. Unfolding of the spectra

The spectra of many complex quantum systems exhibit a universal behavior. To see this, however, one needs to unfold the spectrum. The unfolding can be done if the scale of the variations of the average spectral density is much larger than the scale of the spectral fluctuations. Then we can separate the spectral density in an average density $\bar{\rho}(\lambda)$ and a fluctuating part,

$$\rho(\lambda) = \bar{\rho}(\lambda) + \rho_{\mathrm{fl}}(\lambda) \ . \tag{2.102}$$

The details of the separation are specific for the observable of interest. The only common feature is that the resulting unfolded spectrum $\{x_n\}$ has average spectral density equal to 1 and is given by

$$x_n = \int_{-\infty}^{E_n} \bar{\rho}(\lambda) d\lambda \ , \tag{2.103}$$

where $\{E_n\}$ represents the original spectrum. There are several ways to obtain the average spectral density. In some cases it can be conjectured analytically by some polynomial approximations. In most cases, however, we have to average over many level spacings. There are two different procedures to achieve this. The first is the spectral averaging where one takes averages over many level spacing around the energy of interest. The second is the ensemble average where one performs averages over many different level spacings drawn from all configurations of the ensemble. If we calculate the spectral correlation functions from the unfolded spectrum then these two procedures do not necessarily yield the same behavior at long distances. The equivalence of the two procedures with respect to the correlation functions is known as "spectral ergodicity".

The distribution of the unfolded eigenvalues takes the usual form

$$\rho_{\mathrm{un}}(x) = \sum_n \delta(x - x_n) \ . \tag{2.104}$$

In this context one usually considers the unfolded level spacing Δ_n as a tool to probe the short range correlations in the spectrum

$$\Delta_n = x_n - x_{n-1} \ . \tag{2.105}$$

Its distribution is given by

$$\rho(s) = \sum_n \delta(s - \Delta_n) \ . \tag{2.106}$$

This function is equal to the probability density for two neighboring levels n and $n + 1$ having the spacing s.

For the uncorrelated case it is expected that the level spacings are distributed according to the Poisson distribution $\rho(s) = \exp(-s)$. A good ansatz for the correlated case is provided by the Wigner distributions, which are the exact "spacing distribution" for a 2×2 matrix model [53]

$$\rho(s) = \begin{cases} \frac{\pi}{2} s \, \mathrm{e}^{-\frac{\pi}{4} s^2} & \text{orthogonal ensemble} \\[2mm] \frac{32}{\pi^2} s^2 \, \mathrm{e}^{-\frac{4}{\pi} s^2} & \text{unitary ensemble} \\[2mm] \frac{262144}{729\pi^3} s^4 \, \mathrm{e}^{-\frac{64}{9\pi} s^2} & \text{symplectic ensemble .} \end{cases} \qquad (2.107)$$

2.5 Lattice QCD

2.5.1 The Wilson gauge action and the Wilson fermions

QCD is a renormalizable quantum field theory that must be regularized. A way to achieve this is to put the system on a cubic space-time lattice with some lattice spacing a [54]. This introduces a momentum cut-off of π/a. Now one has to introduce gauge and quark degrees of freedom on the lattice. Maintaining manifest gauge invariance is essential when gauge theories are regularized on the lattice. In order to achieve this one needs a convenient way to represent the gauge fields on the lattice. Wegner and Wilson, as well as Smit, independently introduced the concept of a *parallel transporter* $U_{x,\mu} \in SU(N_c)$ connecting neighboring lattice points x and $x + a\hat{\mu}$. Here $\hat{\mu}$ is a unit vector pointing in the μ direction. The parallel transporter is related to an underlying continuum gauge field $A_\mu(x) = igA_\mu^a(x)T^a$ by

$$U_{x,\mu} = \mathcal{P} \exp \int_0^a ds \; A_\mu(x + \hat{\mu}s) \;, \qquad (2.108)$$

where $\mathcal{P}$ denotes path-ordering for non-Abelian gauge theory. Under a gauge transformation Ω_x the parallel transporter transforms as

$$U'_{x,\mu} = \Omega_x U_{x,\mu} \Omega^\dagger_{x+\hat{\mu}} \;. \qquad (2.109)$$

One tries to preserve as many symmetries as possible at the finite lattice spacing. The hope is that the rest will be recovered in the continuum limit. A gauge action that respects the gauge symmetry was first put forward by

K. G. Wilson. It is a sum over the so-called plaquette variables $U_{x,\mu\nu}^{(P)}$, which are the products of link variables around a closed square path,

$$
\begin{aligned}
S_{\text{YMW}}[U] &= \beta \sum_{x,\mu<\nu} S_P(U_{x,\mu\nu}^{(P)}) \ , \\
S_P(U_{x,\mu\nu}^{(P)}) &= 1 - \frac{1}{N_c}\text{Re}\,\text{Tr}\,U_{x,\mu\nu}^{(P)} \ , \\
U_{x,\mu\nu}^{(P)} &= U_{x,\mu}U_{x+\mu,\nu}U_{x+\nu,\mu}^{\dagger}U_{x,\nu}^{\dagger} \ .
\end{aligned}
\tag{2.110}
$$

$U_{x+\mu,\nu}$ represents a link attached to a site $x+a\hat{\mu}$ and pointing in the direction ν and $U_{x,\nu}^{\dagger}$ represents a link pointing in the opposite direction to ν and attached to the site $x + a\hat{\nu}$. β is related to the bare coupling constant as $\beta = \frac{2N_c}{g^2}$. The Wilson gauge action reduces to the continuum Yang-Mills action (2.5) in the naive continuum limit $a \to 0$. This is demonstrated e.g. in Refs. [5, 55].

To fully define the path integral we must also consider the measure. The lattice functional integral is obtained as an integral over all configurations of parallel transporters $U_{x,\mu}$, i.e.

$$
Z = \prod_{x,\mu} \int_{SU(N_c)} dU_{x,\mu} \ \exp(-S_{\text{YMW}}[U]) \ .
\tag{2.111}
$$

One integrates independently over all link variables using locally the Haar measure $dU_{\mu,x}$ for each parallel transporter.

For compact groups like $SU(N_c)$ the integration is limited to a finite domain. This makes it unnecessary to fix the gauge in lattice QCD because the functional integral is finite even without gauge fixing. This is an important advantage of the formulation using parallel transporters.

The Yang-Mills functional integral contains a single parameter — the bare gauge coupling g. The continuum limit is taken by searching for values of g for which the correlation length of the lattice theory diverges in lattice units. In the language of statistical mechanics one looks for a second order phase transition. Due to asymptotic freedom, in lattice QCD one expects a second order phase transition at $g \to 0$.

The physical observables must be formulated in a gauge invariant way. In fact, the path integral average over gauge non-invariant observables vanish. This statement is a consequence of Elitzur's theorem [56] which in particular implies

$$
\langle U_{x,\mu} \rangle = 0
\tag{2.112}
$$

for each link variable $U_{x,\mu}$.

Now we would like to discuss how the fermion fields are put on the lattice. The quark lattice fields Ψ_x, $\overline{\Psi}_x$ are Grassmann variables attached to the sites x. The Dirac operator contains a continuum derivative which has to be regularized on the lattice. It turned out that it is a highly non-trivial problem to regularize it in a way that preserves the chiral symmetry. The latter becomes of great importance when addressing the physics of light quarks.

A simple way to regularize the Dirac operator is the so-called naive discretization of fermions on a lattice. One substitutes the partial derivatives with finite differences,

$$S[\overline{\Psi}, \Psi] = a^4 \sum_{x,y} \bar{\Psi}_x (D)_{xy} \Psi_y = a^4 \sum_{x,\mu} \frac{1}{2a} (\overline{\Psi}_x \gamma_\mu \Psi_{x+\hat{\mu}} - \overline{\Psi}_{x+\hat{\mu}} \gamma_\mu \Psi_x) + a^4 \sum_x m \overline{\Psi}_x \Psi_x \ .$$

$$(2.113)$$

This action has the so-called doubling problem which is also present in the interacting case, where the action reads,

$$S[\overline{\Psi}, \Psi, U] = a^4 \sum_{x,\mu} \frac{1}{2a} (\bar{\Psi}_x \gamma_\mu U_{x,\mu} \Psi_{x+\hat{\mu}} - \bar{\Psi}_{x+\hat{\mu}} \gamma_\mu U_{x,\mu}^\dagger \Psi_x) + a^4 \sum_x m \bar{\Psi}_x \Psi_x \ .$$

The free quark propagator has poles at momenta $p_\mu = \{0, \pi/a\}$, which gives rise to a total of 2^4 species in 4 dimensions.

It was Wilson who proposed to eliminate the unwanted doubler fermions by breaking chiral symmetry explicitly [57]. The unwanted $2^4 - 1$ species can be sent to the cut-off scale by adding to the Dirac operator an additional term, the Wilson term, which removes the doublers in the continuum limit,

$$\begin{aligned} S_W[\overline{\Psi}, \Psi, U] &= a^4 \sum_{x,y} \bar{\Psi}_x (D_W)_{xy} \Psi_y \\ &= a^4 \sum_{x,\mu} \frac{1}{2a} (\bar{\Psi}_x \gamma_\mu U_{x,\mu} \Psi_{x+\hat{\mu}} - \bar{\Psi}_{x+\hat{\mu}} \gamma_\mu U_{x,\mu}^\dagger \Psi_x) + a^4 \sum_x m \bar{\Psi}_x \Psi_x \\ &+ a^4 \sum_{x,\mu} \frac{1}{2a} (2\bar{\Psi}_x \Psi_x - \bar{\Psi}_x U_{x,\mu} \Psi_{x+\hat{\mu}} - \bar{\Psi}_{x+\hat{\mu}} U_{x,\mu}^\dagger \Psi_x) \ . \end{aligned} \quad (2.114)$$

The doubling problem is expressed by the Nielsen and Ninomiya No-Go theorem [58–60] which states that it is not possible to simultaneously solve the doubling problem and have exact chiral symmetry on the lattice with a local, discretely translation invariant and real Euclidean action for lattice fermions. The locality of a lattice action is defined by requiring the couplings to decay exponentially with the distance. This provides a safe continuum limit for a lattice Dirac operator.

Many lattice Dirac operators, such as the Wilson Dirac operator, satisfy the following condition, which is called γ_5–Hermiticity,

$$\mathcal{D}^\dagger = \gamma_5 \mathcal{D} \gamma_5 \ . \tag{2.115}$$

If the lattice is finite, one can simulate the theory on a computer. This can be done efficiently only in Euclidean space, where the gluonic weight function is $\exp(-S_{\mathrm{YM}})$ with S_{YM} real and positive. The full weight function of QCD also contains the fermion determinant, which can be expressed in terms of the gauge fields. Observables are computed by generating gauge field configurations at some value of β in a Monte Carlo update procedure and averaging an observable over many configurations.

Since the inclusion of the fermion determinant is very time consuming, it is a well-known simplification to use only the gluonic part of the weight function in the Monte Carlo updates, i.e. to perform the *quenched* simulations, which correspond in some sense to the limit $N_f = 0$. To make contact with continuum physics, the results of lattice simulations must be extrapolated to the continuum limit, i.e to the infinite lattice volume and zero lattice spacing keeping the physical volume fixed.

2.5.2   Staggered fermions

For the sake of the following discussion we would like to introduce in this Subsection the staggered fermions. Staggered fermions are obtained from naive doubled lattice fermions (2.113) by the so-called spin diagonalization [61–65]. It consists in performing a local change of fermionic variables

$$\Psi_x \to A_x \Psi_x \ , \quad \overline{\Psi}_x \to \overline{\Psi}_x A_x^\dagger \ , \tag{2.116}$$
$$A_x^\dagger \gamma_\mu A_{x+a\hat{\mu}} = \Delta_\mu(x) \in U(1)^{\otimes d} \ . \tag{2.117}$$

A_x is a $d \times d$ unitary matrix which performs the spin diagonalization and $\Delta_\mu(x)$ is a diagonal unitary matrix belonging to the direct product of $U(1)$ groups denoted by $U(1)^{\otimes d}$. In four space-time dimensions the size of the Dirac matrices is 4×4. By spin diagonalization one can reduce the fermion multiplication factor 2^d to $2^d/4$, where d is the spacetime dimension. Hence, for $d = 4$, staggered fermions represent $2^4/4 = 4$ pseudo-flavors of mass-degenerate fermions. The new fermionic variables χ_x become a $3(\mathrm{colors}) \times 1(\mathrm{spin})$ component object. The corresponding lattice action for free staggered fermions takes the form

$$S[\overline{\chi}, \chi] = a^4 \sum_{x,\mu} \frac{1}{2a} (\overline{\chi}_x \eta_{x,\mu} \chi_{x+\hat{\mu}} - \overline{\chi}_{x+\hat{\mu}} \eta_{x,\mu} \chi_x) + a^4 \sum_x m \overline{\chi}_x \chi_x \ , \tag{2.118}$$

where

$$\eta_{x,1} = 1, \ \eta_{x,2} = (-1)^{x_1/a} \ , \ \eta_{x,3} = (-1)^{(x_1+x_2)/a}, \ \eta_{x,4} = (-1)^{(x_1+x_2+x_3)/a} \ . \tag{2.119}$$

The 4 spin degrees of freedom for the 4 pseudo-flavors are made from the 16 components of the χ field on a 2^4 hypercube [66].

For $m = 0$ the interacting staggered fermion action has an exact remnant $U(1)_e \otimes U(1)_o$ chiral symmetry

$$
\begin{aligned}
\chi'_x &= \exp(i\varphi_e)\chi_x \ , \ \overline{\chi}'_x = \overline{\chi}_x \exp(-i\varphi_o) \ , \ \text{for } (x_1 + x_2 + x_3 + x_4)/a \text{ even } , \\
\chi'_x &= \exp(i\varphi_o)\chi_x \ , \ \overline{\chi}'_x = \overline{\chi} \exp(-i\varphi_e) \ , \ \text{for } (x_1 + x_2 + x_3 + x_4)/a \text{ odd } ,
\end{aligned}
\tag{2.120}
$$

which is a subgroup of the $SU(4)_L \otimes SU(4)_R \otimes U(1)_B$ chiral symmetry of the corresponding continuum theory. These symmetries are expected to be recovered in the continuum limit.

Due to the remnant chiral symmetry the staggered fermions are protected from some problems which are inherent for the Wilson fermions. These are the additive mass renormalization and the problem of the exceptional configurations in the quenched simulations, i.e. the occurrence of the configurations with accidentally small eigenvalues of the lattice Dirac operator. The staggered fermions are also order a^2 improved i.e. the naive discretization errors are expected to behave like $\mathcal{O}(a^2)$ which is opposed to the Wilson fermions where the errors are of order $\mathcal{O}(a)$.

The first down-side of staggered quarks is the fact that we have to deal with exactly four pseudo-flavors. Secondly, the discretization errors induce flavor-changing interactions and so are rather dangerous. To overcome the first problem it is tempting to consider a fourth square root of the staggered Dirac operator to obtain only one pseudo-flavor theory. This operation, however, is dangerous since the locality of the resulting action is questionable [67].

2.5.3 The Ginsparg–Wilson relation and the Neuberger overlap operator

It were Ginsparg and Wilson who first put forward a relation on the lattice Dirac operator which helps to circumvent the Nielsen and Ninomiya No-Go theorem. One gives up the chiral symmetry in its conventional formulation,

$$\{D, \gamma_5\} = 0 \ , \tag{2.121}$$

and requires for the lattice Dirac operator to satisfy the remnant chiral symmetry condition of Ginsparg and Wilson [68],

$$D\gamma_5 + \gamma_5 D = \frac{a}{\mu} D\gamma_5 R D \ . \tag{2.122}$$

where $R_{x,y}$ is a local operator for the x, y indices and its structure in the spinor space is dictated by $\{\gamma_5, R\} = 0$. The Ginsparg-Wilson relation states that the continuum condition for the right-hand-side to vanish is relaxed to a term of $\mathcal{O}(a)$, where a is the lattice spacing. μ is a mass parameter of order $\mathcal{O}(1)$, see below. The Ginsparg-Wilson relation (GWR) implies that

$$D^{-1}\gamma_5 + \gamma_5 D^{-1} = (a/\mu)\gamma_5 R \tag{2.123}$$

is local. It is a formulation of the chiral symmetry after performing the Wilson renormalization group transformation from the continuum theory to the lattice. Hence the Ginsparg-Wilson fermions necessarily have exact zero modes, which occur with positive or negative chirality. From now on we will consider $R_{xy} = \delta_{xy}$. We follow the idea of M. Lüscher and write down a modified infinitesimal chiral transformation on the lattice

$$\Psi' = \Psi + \delta\Psi = \left(1 + i\varepsilon^a T^a \gamma_5 (1 - \frac{a}{2\mu}D)\right) \Psi \ ,$$

$$\overline{\Psi}' = \overline{\Psi} + \delta\overline{\Psi} = \overline{\Psi}\left(1 + i\varepsilon^a T^a (1 - \frac{a}{2\mu}D)\gamma_5\right) \ . \tag{2.124}$$

where ε^a are parameters of the chiral rotation [69].

Through D Lüscher's lattice version of a chiral transformation depends on the gluon field. Still, in the continuum limit $a \to 0$ it reduces to the standard chiral symmetry of the continuum theory. Any lattice fermion action of the form $S_F = a^4 \overline{\Psi} D \Psi$ is invariant under transformation (2.124) to order $\mathcal{O}(\varepsilon)$, provided that D obeys the Ginsparg-Wilson relation Eq. (2.122). Indeed,

$$\begin{aligned}
\delta S_F &= a^4(\delta\overline{\Psi}D\Psi + \overline{\Psi}D\delta\Psi) \\
&\simeq a^4 \overline{\Psi}D i\varepsilon^a T^a \gamma_5 (1 - \frac{a}{2\mu}D) + a^4 \overline{\Psi} i\varepsilon^a T^a (1 - \frac{a}{2\mu}D)\gamma_5 D\Psi \\
&= a^4 \overline{\Psi} i\varepsilon^a T^a \{\gamma_5, D\}\Psi - a^4 \overline{\Psi} i\varepsilon^a T^a \frac{a}{\mu}D\gamma_5 D\Psi = 0 \ . \tag{2.125}
\end{aligned}$$

Under this transformation the fermion measure $D\overline{\Psi}D\Psi$ is not $U(1)_A$ invariant. This is analogous to continuum QCD where this property of the fermion measure in the partition function leads to the anomaly for the axial current. In this way the axial anomaly is also correctly reproduced by the Ginsparg-Wilson fermions [69–71].

We now define the topological charge ν simply by the index

$$\nu = N_+ - N_- \ , \tag{2.126}$$

where N_+ (N_-) is the number of positive (negative) chiral zero modes. Here one adopts the continuum index theorem and uses it to define the topological charge of the lattice gauge configurations [69–71]. Since the Wilson operator D_W obeys γ_5-Hermiticity (2.115) this allows for a simple solution of the GWR by inserting D_W into the overlap formula [72–74],

$$D_{\text{ov}} = \frac{\mu}{a} \left[1 + A / \sqrt{A^\dagger A} \right] \ , \qquad A = a\hat{D} - \mu \ , \tag{2.127}$$

$$\hat{D} = D_W \ . \tag{2.128}$$

D_{ov} is a solution to condition (2.122) and it is γ_5-Hermitian as well. μ represents a negative mass of the Wilson fermion, which can be chosen in some interval as long as the gauge fields are smooth. This particular solution with the kernel $\hat{D} = D_W$ is often referred to as the Neuberger overlap operator. In this thesis we will denote it also as the overlap Wilson Dirac operator.

If we assume that the operator $\hat{D}$ already satisfies the GWR and also is γ_5-Hermitian, then

$$
\begin{aligned}
A^\dagger A &= (a\hat{D}^\dagger - \mu)(a\hat{D} - \mu) = a^2 \hat{D}^\dagger \hat{D} - \mu a(\hat{D}^\dagger + \hat{D}) + \mu^2 = \\
&= a\mu\gamma_5 \left(\frac{a}{\mu} \hat{D}\gamma_5\hat{D} - \{\hat{D}, \gamma_5\} \right) + \mu^2 = \mu^2 \ .
\end{aligned}
\tag{2.129}
$$

This implies for the overlap operator D_{ov}

$$D_{\text{ov}} = \frac{\mu}{a} \left[1 + \frac{a\hat{D} - \mu}{\mu} \right] = \hat{D} \ , \tag{2.130}$$

i.e. an operator satisfying the GWR is reproduced by the overlap formula [75].

Note that the operator $A / \sqrt{A^\dagger A}$ is unitary, hence the spectrum of D_{ov} is located on a circle in the complex plane through zero, with center and radius μ/a, which we denote as the GW circle. [70].

2.5.4 The hypercube Dirac operator

There is a natural way to proceed from the continuum formulation of the action to a lattice form. In this approach one defines the lattice fermion

fields as block averages of continuum fields integrated over hypercubes. The lattice action of these lattice fermion fields is related to the continuum one by the Wilson renormalization group transformation. The resulting lattice theory, which is called the perfect lattice fermions, is equivalent to the underlying continuum theory with respect to the physical observables, i.e. it is completely free of lattice artifacts. Similarly one can also start from a given lattice formulation on a fine lattice and — by using the renormalization group transformation — arrive at another lattice formulation at coarser lattice which is physically equivalent. Iterating this procedure infinitely many times we arrive at the fixed point action (here we assume that this limit exists). The fixed point action of the quantum renormalization group trajectory represents perfect lattice fermions since it is insensitive to a change of the lattice spacing.

To simplify the notation we will set the lattice spacing to $a = 1$. The hypercube Dirac operator is a free fixed point action with its couplings being truncated to the unit hypercube. In this Subsection we consider the construction of the hypercube Dirac operator. The discussion will closely follow Ref. [76]. We will start from the case of free fermions and then explain how gauge fields can be introduced.

Let us divide the (infinite) lattice into disjoint hypercubic blocks of n^d sites each and introduce new variables living on the centers of these blocks (block factor n RGT). Then the RGT relates

$$\Psi'_{x'} \sim \sum_{x \in x'} \Psi_x \ , \qquad\qquad (2.131)$$

where Ψ represents the fermions on the fine lattice and the Ψ' represents fermions on the coarser lattice. The points $x \in \mathbb{Z}^d$ are the sites of the original fine lattice and x' are those of the new lattice with spacing n. $x \in x'$ means that the site x belongs to the block with center x'.

Now the original action $S[\bar{\Psi}, \Psi]$ transforms into a new action $S'[\bar{\Psi}', \Psi']$ on the coarse lattice. The latter is determined by the functional integral

$$e^{-S'[\bar{\Psi}', \Psi']} = \int D\bar{\Psi} D\Psi \ K[\bar{\Psi}', \Psi', \bar{\Psi}, \Psi] e^{-S[\bar{\Psi}, \Psi]} \ . \qquad\qquad (2.132)$$

The kernel $K[\bar{\Psi}', \Psi', \bar{\Psi}, \Psi]$ has to be chosen such that the partition function and all expectation values remain invariant under the RGT. At the end, one usually rescales the lattice spacing back to 1. In any case, the correlation length in lattice units gets divided by n.

For the kernel functional there are many possible choices [77, 78]. We will use the Gaussian type kernel

$$e^{-S'[\bar{\Psi}',\Psi']} = \int D\bar{\Psi} D\Psi \, e^{-S[\bar{\Psi},\Psi]}$$

$$\times \quad \exp\left\{ -\frac{1}{\alpha} \sum_{x'} \left[\bar{\Psi}'_{x'} - \frac{1}{n^{(d+1)/2}} \sum_{x\in x'} \bar{\Psi}_x \right] \left[\Psi'_{x'} - \frac{1}{n^{(d+1)/2}} \sum_{x\in x'} \Psi_x \right] \right\} \quad (2.133)$$

This type of transformation with non-vanishing $\alpha > 0$ is not chirally invariant, which will lead to the formulation with broken chiral symmetry in its standard form given by Eq. (2.121).

Assume that we are on a "critical surface", where the correlation length is infinite. After an infinite number of RGT iterations we obtain a finite fixed point action (FPA) $S^*[\bar{\Psi},\Psi]$. The critical surface requires a fermion mass $m = 0$, but one can generalize the consideration to a finite mass.

Assume that we want to perform a number N of RGT iterations. If we start from a small mass $m/(nN)$, then the final mass will be m. In the limit $nN \to \infty$ (i.e. we start from an infinitesimal mass) we obtain a perfect action at finite mass. In this context, "perfect" means that dimensionless quantities do not depend on the lattice spacing, hence they are identical to the continuum values.

For the above transformation (2.133), this perfect action can be computed analytically in momentum space [79]. The computation simplifies if we let $n \to \infty$, so that $N = 1$ is sufficient. Hence we start from the continuum action now, and the perfect action takes the form

$$
\begin{aligned}
S^*[\bar{\Psi},\Psi] &= \frac{1}{(2\pi)^d} \int_{-\pi}^{\pi} d^d p \, \bar{\Psi}(-p) \Delta^*(p)^{-1} \Psi(p) \, , \\
\Delta^*(p) &= \sum_{l\in\mathbb{Z}^d} \frac{\Pi(p+2\pi l)^2}{i(p_\mu + 2\pi l_\mu)\gamma_\mu + m} + \alpha \, , \\
\Pi(p) &= \prod_{\mu=1}^{d} \frac{2\sin(p_\mu/2)}{p_\mu} \, ,
\end{aligned}
\qquad (2.134)
$$

where Δ^* is the free perfect propagator. The same perfect action is obtained starting from a variety of lattice actions [80], in particular from the Wilson fermion action.

In coordinate space we write this action as

$$S^*[\bar{\Psi},\Psi] = \sum_{x,r} \bar{\Psi}_x [\rho_\mu(r)\gamma_\mu + \lambda(r)]\Psi_{x+r} \, . \qquad (2.135)$$

At the cost of broken chiral symmetry we obtain a theory with its couplings in ρ_μ and λ decaying exponentially as $|r|$ increases. An exception is

the case $d = 1$, where they are confined to one lattice spacing for the special choice

$$\alpha = \frac{e^m - m - 1}{m^2} \ .$$ (2.136)

It is also in agreement with the Nielsen-Ninomiya theorem that, in order to obtain a local perfect action, one must break chiral symmetry explicitly. Although the chiral symmetry is not manifest in the perfect action, all chiral properties are still correctly reproduced by it. This is due to famous Ginsparg-Wilson relation, introduced before in (2.122), to which the perfect action obeys,

$$\{\Delta^*(p), \gamma_5\} = 2\alpha\gamma_5 \ .$$ (2.137)

Here we can identify α with the mass parameter μ, namely,

$$\alpha = \frac{1}{2\mu} \ .$$ (2.138)

It turns out that for the choice of α in Eq. (2.136) the locality is also excellent in higher dimensions, i.e., the exponential decay of the couplings is very fast. This is important, because for practical purposes the couplings have to be truncated to a short range, and the truncation should not distort the perfect properties too much. Ref. [81] proposed a nice truncation scheme that uses periodic boundary conditions over 3 lattice spacings and thus confines the couplings to a unit hypercube. It was pointed out that the spectral and thermodynamic properties of the HF are still drastically improved compared to Wilson fermions [81, 82].

It is far more difficult to construct an approximately perfect action for a complicated interacting theory like QCD. However, as it was proposed in Ref. [76, 81, 83] one can just use a simple ansatz for HF together with the standard gauge link variables. Apart from nearest neighbors, one also has couplings over 2, 3 and 4-space diagonals in the unit hypercube. One connects all these coupled sites by all possible *shortest* lattice paths, by multiplying the compact gauge fields on the path links. This procedure was called "minimal gauging". Note that one can connect two sites x and y lying on d-space diagonals via $d!$ such shortest lattice paths. One averages over all of them to construct the hyper-link, see Figure 2.2 which we adopted from Ref. [76]. The hyper-link $U_\mu^{(1)}(x)$ between site x and $x+\hat{\mu}$ is identified with $U_{x,\mu}$, and we denote the hyper-link in plane, cube and hyper-cube as $U_{\mu+\nu}^{(2)}(x)$, $U_{\mu+\nu+\rho}^{(3)}(x)$, and $U_{\mu+\nu+\rho+\sigma}^{(4)}(x)$, respectively. Then we can write the corresponding fermion matrix in terms of the hyper-links which are constructed recursively starting

from the gauge links $U_\mu^{(1)}$,

$$
\begin{aligned}
U^{(d)}_{\mu_1+\mu_2+\cdots+\mu_d}(x) = \quad \frac{1}{d}\Big[\quad & U^{(1)}_{\mu_1}(x)\,U^{(d-1)}_{\mu_2+\mu_3+\cdots+\mu_d}(x+\hat{\mu}_1) \\
+ \quad & U^{(1)}_{\mu_2}(x)\,U^{(d-1)}_{\mu_1+\mu_3+\cdots+\mu_d}(x+\hat{\mu}_2) \\
+ \quad & \ldots \\
+ \quad & U^{(1)}_{\mu_d}(x)\,U^{(d-1)}_{\mu_1+\mu_2+\cdots+\mu_{d-1}}(x+\hat{\mu}_d) \quad \Big] \;. \quad (2.139)
\end{aligned}
$$
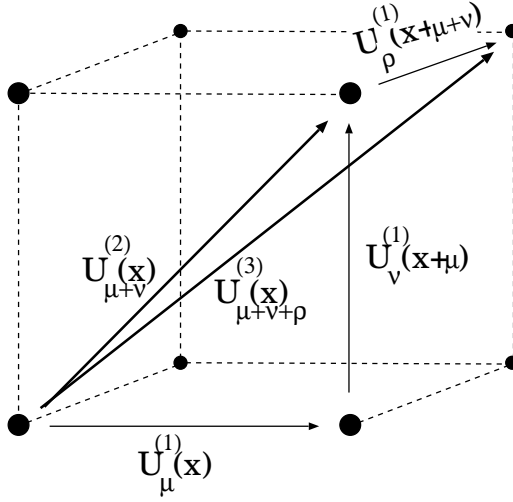
Figure 2.2: 1-space, 2-space and 3-space hyper-links.

It is convenient to introduce prefactors which are functions of the HF hopping parameters κ_i and λ_i, $i = 1, \ldots, 4$, and sums of γ-matrices

$$
\begin{aligned}
\Gamma_{\pm\mu} &= \lambda_1 + \kappa_1(\pm\gamma_\mu) \\
\Gamma_{\pm\mu\pm\nu} &= \lambda_2 + \kappa_2(\pm\gamma_\mu \pm \gamma_\nu) \\
\Gamma_{\pm\mu\pm\nu\pm\rho} &= \lambda_3 + \kappa_3(\pm\gamma_\mu \pm \gamma_\nu \pm \gamma_\rho) \\
\Gamma_{\pm\mu\pm\nu\pm\rho\pm\sigma} &= \lambda_4 + \kappa_4(\pm\gamma_\mu \pm \gamma_\nu \pm \gamma_\rho \pm \gamma_\sigma) \,. \quad (2.140)
\end{aligned}
$$

Note that the λ_i in Eq. (2.140) differ from $\lambda(r)$ in Eq. (2.135) by a normalization factor $\frac{1}{\lambda_0}$. The κ_i arise from $\rho_\mu(r)$ by the same normalization. The couplings are given in Ref. [81] and in Chapter 4.

The hypercube operator is organized in sums which run over four different directions for two 1-space links, six directions for four 2-space links, four directions for eight 3-space links, and one direction for the sixteen 4-space links. Altogether 80 hyper-links plus the term δ_{xy} contribute. With each path of the free HF, a γ-matrix is associated. The γ-matrices are chosen so that

they add up to produce a prefactor Γ, see Eq. (2.140), which is associated with a given hyper-link.

The 1-space links $U_\mu^{(1)}(x)$ are identical to the Hermitian-conjugate links in negative direction, $U_{x+\hat{\mu},-\mu}^{\dagger}$, and this feature also holds for the hyper-links, e.g.

$$U_{\mu_1+\mu_2+\cdots+\mu_d}^{\dagger(d)}(x) = U_{-\mu_1-\mu_2-\cdots-\mu_d}^{(d)}(x + \hat{\mu}_1 + \hat{\mu}_2 + \cdots + \hat{\mu}_d) \ . \qquad (2.141)$$

Therefore, only one half of the $3^d - 1$ hyper-links has to be computed and stored in the implementation of the HF.

As in the case of Wilson fermions, the HF matrix exhibits the "γ_5-Hermiticity"

$$\gamma_5 \, D_{HF} \gamma_5 = D_{HF}^{\dagger} \ , \qquad (2.142)$$

i.e. D_{HF} is non-Hermitian but its eigenvalues come in complex-conjugate pairs. The corresponding HF matrix is defined by [76]

$$
\begin{aligned}
D_{HF}(x,y) \;=\;& \lambda_0 \Bigg\{ \delta_{x,y} \\[4pt]
&+\sum_{\mu} \Big[\Gamma_{+\mu} U^{(1)}_{\mu}(x)\delta_{x,y-\hat\mu} \;+\; \Gamma_{-\mu} U^{(1)}_{-\mu}(x)\delta_{x,y+\hat\mu} \Big] \\[4pt]
&+\sum_{\mu}\sum_{\nu>\mu} \Big[\\
&\quad \Gamma_{+\mu+\nu} U^{(2)}_{+\mu+\nu}(x)\delta_{x,y-\hat\mu-\hat\nu} \;+\; \Gamma_{+\mu-\nu} U^{(2)}_{+\mu-\nu}(x)\delta_{x,y-\hat\mu+\hat\nu} \\
&\quad +\Gamma_{-\mu+\nu} U^{(2)}_{-\mu+\nu}(x)\delta_{x,y+\hat\mu-\hat\nu} \;+\; \Gamma_{-\mu-\nu} U^{(2)}_{-\mu-\nu}(x)\delta_{x,y+\hat\mu+\hat\nu} \Big] \\[4pt]
&+\sum_{\mu}\sum_{\nu>\mu}\sum_{\rho>\nu} \Big[\\
&\quad \Gamma_{+\mu+\nu+\rho} U^{(3)}_{\mu+\nu+\rho}(x)\delta_{x,y-\hat\mu-\hat\nu-\hat\rho} \;+\; \Gamma_{+\mu+\nu-\rho} U^{(3)}_{\mu+\nu-\rho}(x)\delta_{x,y-\hat\mu-\hat\nu+\hat\rho} \\
&\quad +\Gamma_{+\mu-\nu+\rho} U^{(3)}_{\mu-\nu+\rho}(x)\delta_{x,y-\hat\mu+\hat\nu-\hat\rho} \;+\; \Gamma_{+\mu-\nu-\rho} U^{(3)}_{\mu-\nu-\rho}(x)\delta_{x,y-\hat\mu+\hat\nu+\hat\rho} \\
&\quad +\Gamma_{-\mu+\nu+\rho} U^{(3)}_{-\mu+\nu+\rho}(x)\delta_{x,y+\hat\mu-\hat\nu-\hat\rho} \;+\; \Gamma_{-\mu+\nu-\rho} U^{(3)}_{-\mu+\nu-\rho}(x)\delta_{x,y+\hat\mu-\hat\nu+\hat\rho} \\
&\quad +\Gamma_{-\mu-\nu-\rho} U^{(3)}_{-\mu-\nu+\rho}(x)\delta_{x,y+\hat\mu+\hat\nu-\hat\rho} \;+\; \Gamma_{-\mu-\nu-\rho} U^{(3)}_{-\mu-\nu-\rho}(x)\delta_{x,y+\hat\mu+\hat\nu+\hat\rho} \Big] \\[4pt]
&+\sum_{\mu}\sum_{\nu>\mu}\sum_{\rho>\nu}\sum_{\sigma>\rho} \Big[\\
&\quad \Gamma_{+\mu+\nu+\rho+\sigma} U^{(4)}_{\mu+\nu+\rho+\sigma}(x)\delta_{x,y-\hat\mu-\hat\nu-\hat\rho-\hat\sigma} \;+\; \Gamma_{+\mu+\nu+\rho-\sigma} U^{(4)}_{\mu+\nu+\rho-\sigma}(x)\delta_{x,y-\hat\mu-\hat\nu-\hat\rho+\hat\sigma} \\
&\quad +\Gamma_{+\mu+\nu-\rho+\sigma} U^{(4)}_{\mu+\nu-\rho+\sigma}(x)\delta_{x,y-\hat\mu-\hat\nu+\hat\rho-\hat\sigma} \;+\; \Gamma_{+\mu+\nu-\rho-\sigma} U^{(4)}_{\mu+\nu-\rho-\sigma}(x)\delta_{x,y-\hat\mu-\hat\nu+\hat\rho+\hat\sigma} \\
&\quad +\Gamma_{+\mu-\nu+\rho+\sigma} U^{(4)}_{\mu-\nu+\rho+\sigma}(x)\delta_{x,y-\hat\mu+\hat\nu-\hat\rho-\hat\sigma} \;+\; \Gamma_{+\mu-\nu+\rho-\sigma} U^{(4)}_{\mu-\nu+\rho-\sigma}(x)\delta_{x,y-\hat\mu+\hat\nu-\hat\rho+\hat\sigma} \\
&\quad +\Gamma_{+\mu-\nu-\rho+\sigma} U^{(4)}_{\mu-\nu-\rho+\sigma}(x)\delta_{x,y-\hat\mu+\hat\nu+\hat\rho-\hat\sigma} \;+\; \Gamma_{+\mu-\nu-\rho-\sigma} U^{(4)}_{\mu-\nu-\rho-\sigma}(x)\delta_{x,y-\hat\mu+\hat\nu+\hat\rho+\hat\sigma} \\
&\quad +\Gamma_{-\mu+\nu+\rho+\sigma} U^{(4)}_{-\mu+\nu+\rho+\sigma}(x)\delta_{x,y+\hat\mu-\hat\nu-\hat\rho-\hat\sigma} \;+\; \Gamma_{-\mu+\nu+\rho-\sigma} U^{(4)}_{-\mu+\nu+\rho-\sigma}(x)\delta_{x,y+\hat\mu-\hat\nu-\hat\rho+\hat\sigma} \\
&\quad +\Gamma_{-\mu+\nu-\rho+\sigma} U^{(4)}_{-\mu+\nu-\rho+\sigma}(x)\delta_{x,y+\hat\mu-\hat\nu+\hat\rho-\hat\sigma} \;+\; \Gamma_{-\mu+\nu-\rho-\sigma} U^{(4)}_{-\mu+\nu-\rho-\sigma}(x)\delta_{x,y+\hat\mu-\hat\nu+\hat\rho+\hat\sigma} \\
&\quad +\Gamma_{-\mu-\nu+\rho+\sigma} U^{(4)}_{-\mu-\nu+\rho+\sigma}(x)\delta_{x,y+\hat\mu+\hat\nu-\hat\rho-\hat\sigma} \;+\; \Gamma_{-\mu-\nu+\rho-\sigma} U^{(4)}_{-\mu-\nu+\rho-\sigma}(x)\delta_{x,y+\hat\mu+\hat\nu-\hat\rho+\hat\sigma} \\
&\quad +\Gamma_{-\mu-\nu-\rho+\sigma} U^{(4)}_{-\mu-\nu-\rho+\sigma}(x)\delta_{x,y+\hat\mu+\hat\nu+\hat\rho-\hat\sigma} \;+\; \Gamma_{-\mu-\nu-\rho-\sigma} U^{(4)}_{-\mu-\nu-\rho-\sigma}(x)\delta_{x,y+\hat\mu+\hat\nu+\hat\rho+\hat\sigma} \\
&\quad \Big] \Bigg\} .
\end{aligned}
$$

$$(2.143)$$

2.5.5   The overlap hypercube Dirac operator

In this Section we would like to present motivations for a non-standard choice of the kernel in the overlap formula.

The generalization of the overlap fermions to a whole class of solutions of the GWR and the motivation for considering alternative kernels $\hat{D}$ were given in Ref. [75]. In particular it was pointed out that the Ginsparg-Wilson fermions reproduce themselves if the kernel already obeys GWR as we showed in Section 2.5.3. To put it the other way: if the kernel does not obey the GWR then it gets corrected by the overlap formula [75]. This additional freedom of having different kernels can be used in order to improve such properties of the overlap operator as locality and get rid of the lattice artifacts which reside, for example, in approximate rotational symmetry. Also the dependence of the observables on different lattice spacings, that is referred to as the scaling behavior, is expected to be improvable. To this end we start from the kernel that already has good properties in rotational invariance, locality, scaling behavior and approximately satisfies the GWR. If we insert it into the overlap formula then we can expect that due to its already good chiral properties the chiral corrections to the operator will be small and therefore the properties of locality, approximate rotational symmetry and scaling behavior will be essentially inherited by the resulting overlap operator [75]. A good candidate for that would be the approximate perfect fermions introduced in the previous Subsection.

When constructing the overlap operator the parameter μ must be chosen in some interval to ensure that the doublers are projected to the right arc of the GW spectrum. This interval is $\mu \in [0, 2]$ for the free Wilson fermions and shrinks from both sides in the interacting case. This procedure can be realized once the gauge configurations are smooth enough (or β is sufficiently large) to allow for the spectrum of the kernel develop such a window. It is conceivable that using the hypercube operator as a kernel in the overlap formula one can admit lower values of β than it is the case for the Wilson kernel. This is based on the fact that the hypercube operator approximately obeys GW relation and this should lead to a better behavior in its spectrum. Having the doublers projected to the cut-off scale one can optimize the overlap operator further by requiring the best locality properties or the least condition number for the $A^\dagger A$ operator. This will specify μ and also impose additional constraints on the couplings in the hypercube operator.

Chapter 3

Lattice simulations

3.1 Quenched simulations of the gauge fields

The QCD partition function in the formalism of the path integral is defined by an integral with an infinite number of dimensions which cannot be analytically solved so far. However its regularization on a finite lattice is reduced to an integral over a finite number of dimensions and can be used to address non-perturbative physics. To this end one can use the Monte Carlo (MC) simulations to evaluate the lattice regularized partition function.

In lattice MC simulations of quenched QCD one usually generates equilibrium gauge configurations of $SU(3)$ fields U with a probability distribution proportional to $W[U] = e^{-S_{YM}[U]}$ at a certain value of the strong gauge coupling. This procedure is referred to as importance sampling. It can be simulated by generating a Markov chain of configurations. One parameterizes the Markov chain with τ and introduces the transition probability matrix $P([U_{\tau+1}] \leftarrow [U_\tau])$ connecting the field configuration at simulation time τ and $\tau + 1$. A condition to arrive at the equilibrium distribution in the limit of large τ is detailed balance

$$P(\,[U_{\tau+1}] \leftarrow [U_\tau]\,)\,W[U_\tau] = P(\,[U_\tau] \leftarrow [U_{\tau+1}]\,)\,W[U_{\tau+1}]\;. \qquad (3.1)$$

For quenched simulations it is numerically favorable to perform a link by link update of the given configuration instead of the update of it as a whole. The process when all links of the field configuration have been once updated is referred to as a configuration update or one sweep. In quenched $SU(3)$ gauge simulations two transition probability distributions are mostly used. These are the heat bath [84] and Metropolis [85] transition probability distributions. The heat bath was conventionally designed for the generation of $SU(2)$ pure gauge configurations. To adopt it for quenched simulations with

the $SU(3)$ gauge group one needs to use the Cabbibo-Marinari update [86] whereby one splits an $SU(3)$ link variable in three $SU(2)$ link variables and performs the heat bath update over each of them. Then these three $SU(2)$ link variables are reassembled again in the updated $SU(3)$ link variable. In Markov processes one has to consider the autocorrelation of the configurations. Indeed since every next configuration is produced from the previous one, it contains information about it. This spoils the sampling of observables which in the spirit of MC simulations are supposed to be computed on an uncorrelated set of configurations picked out with the probability distribution $W[U] = e^{-S_{YM}[U]}$. Since the quenched updates are computationally quite fast we can arrange for many of them in-between to make sure that the resulting configurations become uncorrelated. To cope with the autocorrelations and thereby to speed up the updating process it was proposed [87–90] also to choose the trial elements for the update in a particular way. This is the so-called overrelaxation update. It is achieved by choosing the new link $U'_{x,\mu}$ as far as possible from $U_{x,\mu}$. The overrelaxation update for $SU(N)$ gauge fields relies on the particular form of the lattice gauge action. The part of the gauge action containing one link variable $U_{x,\mu}$ must have the form

$$\Delta S[U_{x,\mu}] = \text{const} \cdot \text{Re} \, \text{Tr}(U_{x,\mu}V) \, , \tag{3.2}$$

where the matrix V does not necessarily belong to $SU(N)$. This is the case in particular for the Wilson gauge action (2.110) that we are using.

3.2 A numerical treatment of the overlap Dirac operator

In this Subsection we discuss numerical details of simulations of the overlap Dirac operator.

The formula of the overlap Dirac operator contains the square root of a Hermitian operator. It is instructive to rewrite it as

$$
\begin{aligned}
D_{ov} &= \mu \left[1 + \gamma_5 \frac{Q}{\sqrt{Q^2}} \right] , \\
Q &= c\gamma_5(\hat{D} - \mu) , \quad \hat{D} = D_W .
\end{aligned} \tag{3.3}
$$

Q is a Hermitian operator and constant c was chosen to ensure that the spectrum of Q^2 is bounded by 1. For our treatment of the square root we used the Chebyshev polynomials $T_n(x)$ to approximate the function $1/\sqrt{x}$

in the interval $(\epsilon, 1)$, where ϵ is the inverse condition number of the operator Q^2. This method was proposed in Ref. [91]

The Chebyshev polynomials T_i are the orthonormal polynomials with respect to the inner product

$$\langle T_i, T_j \rangle = \int_{-1}^{1} \frac{1}{\sqrt{(1 - t^2)}} T_i(t) T_j(t) \, dt \ . \tag{3.4}$$

We thus have

$$\langle T_i, T_j \rangle = \delta_{ij} \ . \tag{3.5}$$

Every function f for which $\langle f, f \rangle$ exists can be expanded into its Chebyshev series

$$f(x) = \sum_{i=0}^{\infty} c_i T_i(x) \quad \text{where} \quad c_i = \langle f, T_i \rangle \ . \tag{3.6}$$

Truncating the series at the N-th summand gives the polynomial approximation of degree $N - 1$

$$P_{N-1}(x) = \sum_{i=0}^{N-1} c_i T_i(x) \ . \tag{3.7}$$

The Chebyshev polynomials $T_n(x)$ have exactly n zeros on the interval $[-1, 1]$, and they are located at the points

$$x_k = \cos\left(\frac{\pi(k - 0.5)}{n}\right) \quad \text{where} \quad k = 1, 2, \dots, n \ . \tag{3.8}$$

In the same interval there are $n + 1$ extrema (maxima and minima), located at

$$x_k = \cos\left(\frac{\pi k}{n}\right) \quad \text{where} \quad k = 0, 1, \dots, n \ . \tag{3.9}$$

At all of the maxima we have $T_n(x) = 1$, while at all of the minima $T_n(x) = -1$. This property makes the Chebyshev polynomials so useful in polynomial approximation of functions. It provides the basis for deducing the bounds of the maximal error in the approximation.

The coefficients c_j of the series (3.7) are given by

$$c_j = \frac{2}{N} \sum_{k=1}^{N} f(x_k) T_j(x_k) \ , \quad \text{where} \quad j = 0, \dots, N - 1 \ , \tag{3.10}$$

where x_k are the N zeros of $T_N(x)$. Then for an arbitrary function f on the interval $[-1, 1]$ the approximation formula

$$f(x) \simeq P_{N-1}(x) = \left[\sum_{k=0}^{N-1} c_k T_k(x) \right] - \frac{1}{2} c_0 \qquad (3.11)$$

is exact at $x_1, \ldots, x_N$.

For any point $x \in [-1, 1]$ this gives the Chebyshev approximation of degree $N - 1$ for function $f(x)$. The Chebyshev approximation is not the best approximation with respect to all polynomials of the same degree, i.e. it does not have the smallest maximum deviation from the true general function. The latter is true for the so-called minimax polynomials. However the Chebyshev approximation is almost as good as the minimax polynomials. The advantage of the Chebyshev polynomials is that the formulae (3.10) and (3.11) can be arranged in one recurrence process, the Clenshaw recurrence formula [92]. This property makes the Chebyshev polynomials attractive for numerical simulations since one can avoid the calculation and use of the c_j coefficients which can take large magnitudes and bring in numerical instabilities.

In our simulations we made the following approximation

$$\frac{1}{\sqrt{t}} = P_{N,\epsilon}(t) , \quad \text{where} \quad t \in [\epsilon, 1] , \qquad (3.12)$$

and $\epsilon = \lambda_{\min}/\lambda_{\max}$, where $\lambda_{\min}$ and $\lambda_{\max}$ are the minimal and maximal eigenvalues of Q^2, respectively.

Inserting the approximation to the square root we obtain for the overlap Dirac operator

$$D_{\mathrm{ov}} \simeq \mu \left[1 + \gamma_5 Q P_{N,\epsilon}(Q^2) \right] . \qquad (3.13)$$

The degree N of the polynomial approximation was chosen in a way to obtain a specific precision $\epsilon_{\mathrm{overlap}}$ for the square root approximation

$$\frac{\|X - Q^2 P_{N,\epsilon}(Q^2)^2 X\|}{4\|X\|} \leq \epsilon_{\mathrm{overlap}} , \qquad (3.14)$$

where X is a random spinor vector and $\epsilon_{\mathrm{overlap}}$ was usually chosen between 10^{-12} and 10^{-15}. We checked that this condition is insensitive to different choices of the random vector X. It also implies a similar precision for the GWR.

The computational cost of the approximation is roughly proportional to the polynomial degree. The latter is proportional to the square root of the condition number. In order to decrease the condition number of the Q^2

operator, $\lambda_{\max}/\lambda_{\min}$, and thus to decrease the required polynomial degree, we projected out the lowest eigenmodes,

$$Q^2_{\mathrm{proj}} = Q^2 - \sum_{k=1}^{m} \lambda_k^2 |k\rangle\langle k| , \quad \text{where} \quad Q^2 |k\rangle = \lambda_k^2 |k\rangle . \tag{3.15}$$

Then the overlap formula takes the form

$$D_{ov} = \mu \left[1 + \gamma_5 Q_{\mathrm{proj}} P_{N,\epsilon}(Q^2_{\mathrm{proj}}) + \gamma_5 \sum_{k=1}^{m} |k\rangle\langle k| \operatorname{sign}(\lambda_k) \right] , \tag{3.16}$$

and the condition number has to be evaluated with respect to the operator Q^2_{proj}. To render the chiral symmetry reliable and assure the convergence of the polynomial approximation, the eigenvectors of the operator Q^2 should be computed to a very good accuracy. We take it again to be between 10^{-12} and 10^{-15}.

For $\beta = 5.85$ and $\beta = 6$ on lattices of $V = 8^4$, 10^4 we projected out 10 eigenvectors. It turned out that projecting out more of them does not help much any more. This is due to the fact that above a certain energy the eigenvalues are densely packed and further increasing the number of projected out eigenvectors does not influence much the condition number. In Figure 3.1 we show the condition number for the lattice volumes $V = 8^4$ and 10^4 at $\beta = 5.85$ and $\mu = 1.6$. Here we projected out 5, 10 and 20 eigenvectors, respectively. The corresponding degree of the polynomial approximation varies for different lattice volumes and β. For instance on the 10^4 lattice at $\beta = 5.85$, for 44 projected out eigenvectors it was about 180 at $\epsilon_{\mathrm{overlap}} = 10^{-15}$.

In addition one has to assure that one deals with a local formulation of the overlap fermions. The locality of the overlap Wilson fermions is related to the spectrum of its Q^2 operator. Let the spectrum be bounded by u from below and by 1 from above

$$u \le \lambda(Q^2) \le 1 . \tag{3.17}$$

If u comes too close to the origin and the spectrum develops also very dense eigenvalues then this will lead to strong fluctuations in the inverse square root and locality will be lost. Note, however, that the presence of a few near-zero eigenvalues does not spoil the locality. The issue of locality was addressed in Ref. [91] where also a numerical study at $\beta = 6, 6.2, 6.4$ was presented. Analytically the locality properties of the overlap operator can be established for smooth configurations. Once each plaquette variable $U^{(P)}$
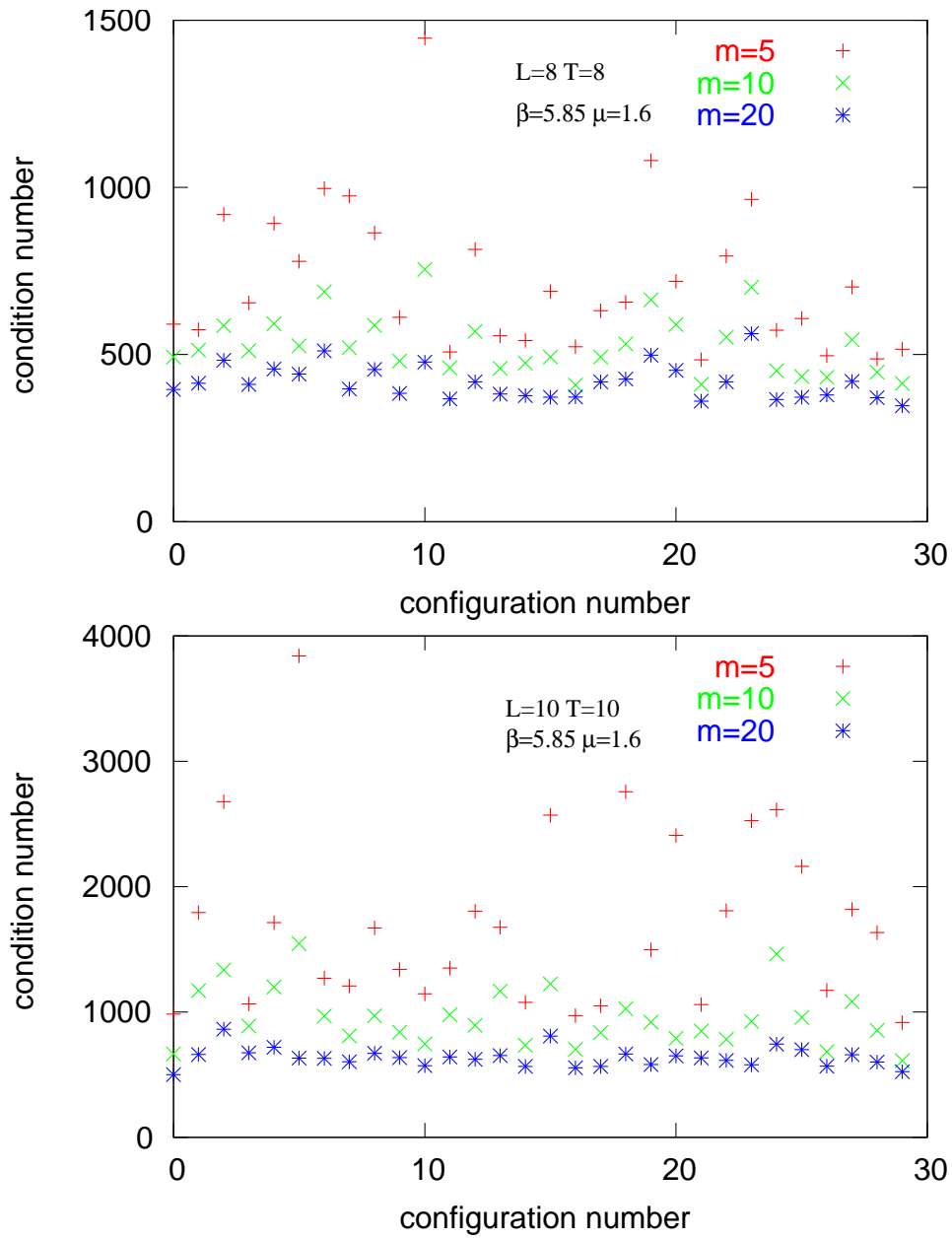
Figure 3.1: The condition number of the Q^2 operator in $V = 8^4$ and 10^4 volumes at $\beta = 5.85$ and $\mu = 1.6$ after $m = 5$, 10 and 20 eigenvectors being projected out.

53

defined in Eq. (2.110) obeys an inequality of the form

$$|1 - \frac{1}{3}\mathrm{Re}\,\mathrm{Tr}\,U^{(P)}| \leq \epsilon \quad \text{for all plaquettes} \tag{3.18}$$

then the operator Q^2 is uniformly bounded from below and the locality is guaranteed. In particular, for $\mu = 1$ Ref. [91] found the condition

$$\frac{Q^2}{c^2} \geq 1 - 30\epsilon \;. \tag{3.19}$$

Even if this condition is not obeyed, numerical results can still reveal locality. In particular in the simulations at $\beta = 6$, 6.2, 6.4 the corresponding overlap operator can be made local [91]. The optimal locality is achieved by varying the parameter μ. The optimized values of μ at $\beta = 6$, 6.2, 6.4 were presented in Ref. [91] and in Ref. [93] the value of μ that guarantees a good locality at $\beta = 5.85$ was pointed out.

The mass μ separates doublers from the "physical" eigenvalues of the Wilson operator, which are projected onto the left arc of the GW fermion spectrum. This imposes a restriction on μ to be between $0 \leq \mu \leq 2$ in the free case. In the interacting case the interval shrinks from both sides. The separation can be done unambiguously only if the spectrum of the Wilson operator has a window with a negligible eigenvalue density. The latter cannot be achieved for the Wilson operator at strong β. Therefore one rather has to work in a range of moderate values of β. For illustration of this behavior we show in Figure 3.2 [94] two plots of the distribution of eigenvalues of the Wilson operator for quenched QCD configurations at $\beta = 5.6$ and $\beta = 5.4$ on the lattice of volume 4^4. The left plot shows a spectrum with such a window while the right plot does not have it. Note that these distributions are done for quite small lattices and due to the boundary conditions the configurations are smother than they would be in a larger volume at the same β. Hence the window in the spectrum opens up at somewhat lower values of β than it would be expected for large lattice volumes.

Once the window was identified one can use the freedom of varying the value of μ within the window to optimize the locality properties further. This can be done by comparing the exponential decays of the couplings of the overlap operator at different μ. It turned out that the locality breaks down once β is below the value about 5.7 [95].

According to Ref. [91] it is optimal for locality to put $\mu = 1.4$ at $\beta = 6$ and from Ref. [93] $\mu = 1.6$ at $\beta = 5.85$. In Figure 3.3 we show the locality property of the overlap Wilson operator at $\beta = 5.85$, $\mu = 1.6$. We take the
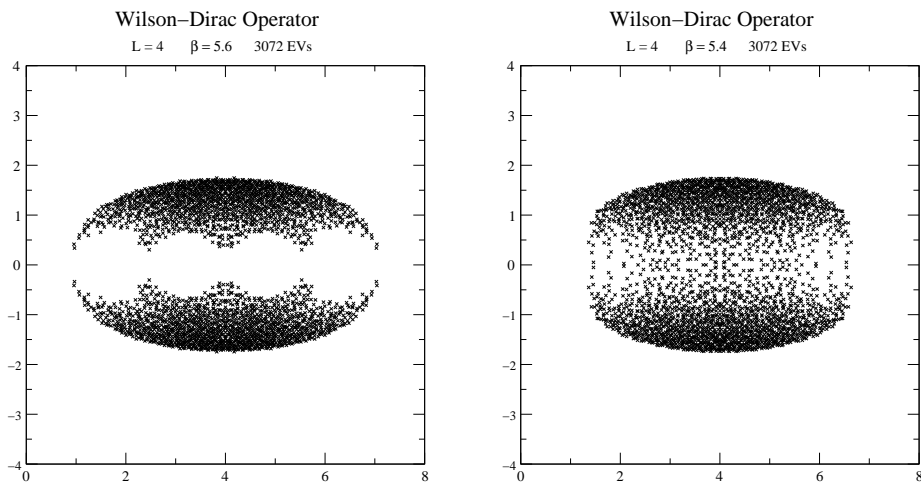
Figure 3.2: Eigenvalues of the Wilson operator at $\beta = 5.6$ and $\beta = 5.4$ on the lattice 4^4. We see that at $\beta = 5.4$ the spectrum does not develop a window.
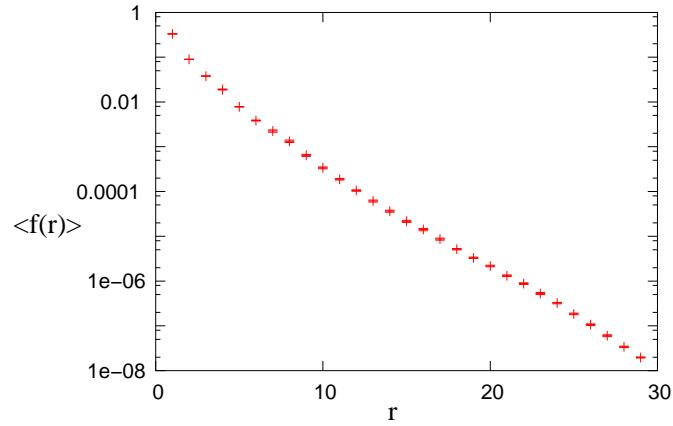
Figure 3.3: Locality of the overlap Wilson operator at $\beta = 5.85$, $\mu = 1.6$ on the lattice of volume $12^3 \times 24$. The exponential decay is clearly pronounced.

"taxi driver metrics" $\|x - y\|_{\text{taxi}}$ to measure the distance on the lattice

$$\|x - y\|_{\text{taxi}} = \sum_{\mu=1}^{4} |x_\mu - y_\mu| \ . \tag{3.20}$$

The locality is measured in terms of $f(r)$

$$f(r) = \max_x || \sum_y (D_{\text{ov}})_{xy} \psi_y || \ , \quad \text{where} \quad r = ||x - x_0||_{\text{taxi}} \quad \text{and} \quad \psi_y = \delta_{yx_0} \ . \tag{3.21}$$

We see in Figure 3.3 that the decay is safely exponential and therefore the operator is local.

Chapter 4

Numerical treatment of the hypercube fermions

In this Chapter we discuss the simulation of the hypercube Dirac operator. First we consider the hypercube operator itself. We tune it to decrease the remaining additive mass renormalization and minimize the violation of the GWR, i.e. to improve its chiral behavior. Secondly we use the hypercube operator as a kernel for the overlap operator. Since the hypercube operator is a truncated fixed point operator we expect that the favorable properties such as locality become much better than for the overlap Wilson Dirac operator.

Note that the hypercube operator would be perfect if we considered it for the free case on the lattice of size 3^4. This provides us with an ansatz for the parameters $(\lambda_0, \ldots, \lambda_4, \kappa_1, \ldots, \kappa_4)$ in Eq. (2.143). We give the corresponding values in Table 4.1. On a larger lattice and for the interactive case we adopted the "minimal gauging" described in Subsection 2.5.4. As an ansatz for the couplings we take the values from the free case to start with. However this creates a large additive mass renormalization that was pointed out in Ref. [96]. In order to account for it we rescaled the parameters λ_i and κ_j as it was prescribed in Ref. [96].

$$
\begin{aligned}
\lambda_0 &\rightarrow \lambda_0 \ , \\
\lambda_1 &\rightarrow u\lambda_1 \ , \quad \kappa_1 \rightarrow uv\,\kappa_1 \ , \\
\lambda_2 &\rightarrow u^2\lambda_2 \ , \quad \kappa_2 \rightarrow (uv)^2\kappa_2 \ , \\
\lambda_3 &\rightarrow u^3\lambda_3 \ , \quad \kappa_3 \rightarrow (uv)^3\kappa_3 \ , \\
\lambda_4 &\rightarrow u^4\lambda_4 \ , \quad \kappa_4 \rightarrow (uv)^4\kappa_4 \ , \quad (4.1)
\end{aligned}
$$

where $1/u \leq v \leq 1$.

If we represent the hypercube operator as $D_{HF}[x, y, U] = \gamma_\mu \rho_\mu(x, y, U) + \lambda(x, y, U)$ then the rescaling of the couplings would imply a rescaling of the

link variable $U_\mu(x)$ as follows

$$
\begin{aligned}
U_{x,\mu} &\to uv\,U_{x,\mu} \quad \text{in} \quad \rho_\mu(x,y,U) \ , \\
U_{x,\mu} &\to u\,U_{x,\mu} \quad\ \text{in} \quad \lambda(x,y,U) \ .
\end{aligned}
\tag{4.2}
$$

The factor u is used to compensate the (mean) link suppression due to the gauge field and therefore reduce the mass renormalization. The factor v controls mostly the imaginary part of the eigenvalues and serves to move them closer to the GW circle which we described below Eq. (2.130).

A further chiral improvement which was outlined in Ref. [96] is the use of the fat link. For a given configuration we substitute each link variable $U_{x,\mu}$ by the following expression

$$
U_{x,\mu} \to (1-\alpha)U_{x,\mu} + \frac{\alpha}{6}\left[\sum \text{staples}\right] \ ,
\tag{4.3}
$$

where the staples for the link $U_{x,\mu}$ are depicted on the Figure 4.1. The staples are calculated as a product of the three links and are given by: $U_{x,\nu}\,U_{x+\hat\nu,\mu}\,U^\dagger_{x+\hat\mu,\nu}$ in positive direction and $U^\dagger_{x-\hat\nu,\nu}\,U_{x-\hat\nu,\mu}\,U_{x-\hat\nu+\hat\mu,\nu}$ in negative direction. In the four dimensional space there are six staples for each link variable, hence the factor 6 in the definition.

We applied a step by step procedure to tune couplings of the hypercube operator for quenched configurations generated at $\beta = 5.85$. We started from a 8^4 lattice and worked out a first approximation of α, u and v by plotting the eigenvalue spectrum of the hypercube operator D_{HF} and comparing it with the GW circle. In this way we obtained the following approximations

$$
\alpha = 0.3 \ , \quad u = 1.32 \ , \quad v = 0.76 \ .
\tag{4.4}
$$

In Figure 4.2 we plot the lowest 80 eigenvalues of the hypercube operator for a typical configuration on 8^4 lattice at $\beta = 5.85$ for the mentioned parameters. To improve the chiral properties of the hypercube operator further we decided to look at the condition number of the Q^2 operator resp. the polynomial degree of the overlap hypercube Dirac operator after projecting out 44 eigenvectors as a function of α, u and v for a given lattice volume $L^3 \times T$. The accuracy of the Q^2 eigenvectors was taken 10^{-12} and the accuracy for the polynomial approximation was of 10^{-15}. These accuracies were sufficient to obtain a good convergence of the Chebyshev polynomial approximation. The parameter μ of an auxiliary mass in the definition of the operator $Q = c\gamma_5(D_{\text{HF}} - \mu)$ c.f. Eq. (3.3) becomes redundant in this context since we can account for it by the proper combination of u and v. Therefore we set $\mu = 1$. We calculated the average value of the Q^2 condition number over 30 configurations — which we found to be sufficient for this purpose

— and built the gradient of it in the three dimensional parameter space of α, u and v. By going in the direction of the gradient, i.e. the direction of the steepest descent, we found the parameters optimized with respect to the condition number of Q^2. This procedure was iterated until it converged. The optimal parameters are given in Table 4.2.

Alternatively, one can also think of an optimization with respect to the locality properties. On the lattice 10^4 we found that if we increase the parameter α then the locality properties of the corresponding overlap hypercube Dirac operator become worse. Therefore we decided to relax the optimal parameter α for the condition number in favor of the locality of the resulting operator. We want to point out that the parameter α was decreased only mildly to provide the better locality property and still keeping the condition number at a good value. The suitable parameter α in this respect is $\alpha = 0.52$ on 10^4 lattice at $\beta = 5.85$. When we increased the lattice volume to $12^3 \times 24$ we found out that the trend established on a smaller lattice is reproduced to a good extent. Therefore we can safely adopt the parameters from the study on the 10^4 lattice. This we first confirmed by the recalculating the gradient for the optimal parameters on the $12^3 \times 24$ lattice. Secondly it is supported by the behavior of the locality properties on 10^4 and $12^3 \times 24$ lattices. To illustrate this we show in Figure 4.3 the locality of the overlap hypercube Dirac operator at two different values of α together with the locality of the overlap Wilson Dirac operator. We see that the larger value of α, which corresponds to a lower value of the condition number, shows a weaker slope and thus results in a worse locality. We therefore decide to stick in our simulations of the overlap hypercube Dirac operator to $\alpha = 0.52$. We also observe that the locality behavior on the 10^4 lattice is reproduced almost identically on a larger $12^3 \times 24$ lattice.

In Table 4.3 we give the condition numbers for the hypercube Q^2 operator for two optimized sets of parameters: with respect to the best condition number and the locality properties. We include the polynomial degree of the overlap hypercube operator after 44 eigenvectors being projected out at accuracy $\epsilon_{\text{overlap}} = 10^{-15}$. In Table 4.4 we add for comparison the condition number for the Wilson Q^2 operator. Note that the degree of the Chebyshev polynomial approximation is proportional to the square root of the condition number.

λ_0	1.8527205471652000
λ_1	-0.0327938644185406
λ_2	-0.0162118524304803
λ_3	-0.0086184721387295
λ_4	-0.0045483448675513
κ_1	0.0738626203107888
κ_2	0.0173136117866899
κ_3	0.0059685910389885
κ_4	0.0025632525141047

Table 4.1: The parameters of the HF.
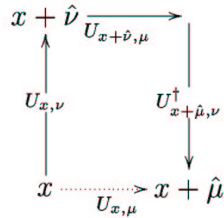
Figure 4.1: A staple in the positive direction for the link variable $U_{x,\mu}$.
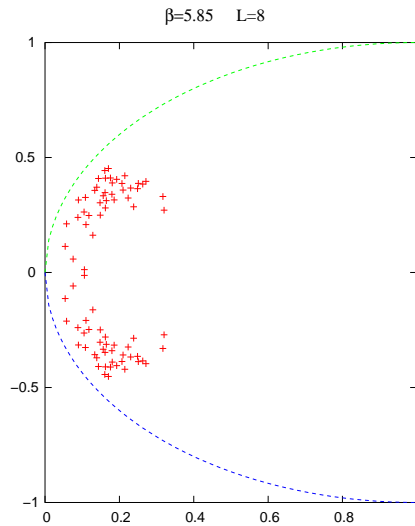
Figure 4.2: The lowest 80 eigenvalues of the hypercube operator D_{HF} with $\alpha = 0.3$, $u = 1.32$, $v = 0.76$ on a 8^4 lattice, at $\beta = 5.85$. For comparison we also show the corresponding GW circle.

V	u	v	α
8^4	1.22	0.76	0.4
10^4	1.28	0.96	0.72

Table 4.2: The parameters of the HF optimized with respect to the condition number at $\beta = 5.85$.
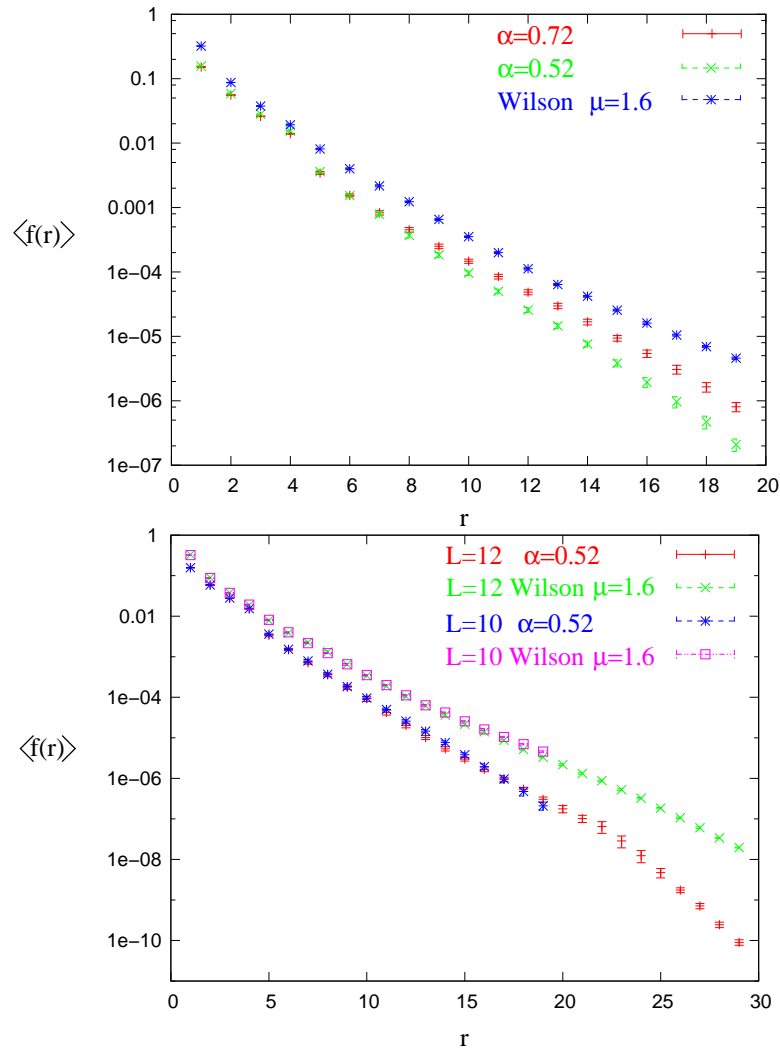
Figure 4.3: The locality of the overlap HF and the overlap Wilson fermions vs. the taxi driver distance r. The upper Figure shows the results on a 10^4 lattice, and the lower Figure shows two results on $12^3 \times 24$ lattice along with 10^4 lattice. We see the same exponential decay as we increase the lattice volume.

V	u	v	α	polynomial degree	condition number		
					$m = 20$	$m = 30$	$m = 40$
8^4	1.22	0.76	0.4		25.2 ± 0.6	22.2 ± 0.4	20.2 ± 0.3
10^4	1.28	0.96	0.52	40 ± 1	26.8 ± 0.9	22 ± 0.5	19.4 ± 0.4
10^4	1.28	0.96	0.72	39 ± 1	26 ± 1	20.9 ± 0.6	18.2 ± 0.3
$12^3 \times 24$	1.28	0.96	0.52	53 ± 1	81 ± 4	52 ± 3	41 ± 1

Table 4.3: The condition number for the hypercube Q^2 operator at $\mu = 1$ after $m = 20, 30, 40$ eigenvectors being projected out and the polynomial degree for the overlap hypercube Dirac operator after 44 eigenvectors being projected out.

V	polynomial degree	condition number		
		$m = 20$	$m = 30$	$m = 40$
8^4		417 ± 10	363 ± 8	330 ± 4
10^4	172 ± 1	636 ± 14	529 ± 10	467 ± 7
$12^3 \times 24$	247 ± 4	2100 ± 200	1260 ± 60	996 ± 36

Table 4.4: The condition number for the Wilson Q^2 operator at $\mu = 1.6$ after $m = 20, 30, 40$ eigenvectors being projected out and the polynomial degree of the overlap Wilson Dirac operator after 44 eigenvectors being projected out.

Chapter 5

Results on the pion dispersion relation

The p–expansion can be used once the pion Compton wavelength is well accommodated inside the physical volume. This implies that in order to reach the chiral limit, i.e. very small quark masses, one has to simulate in extremely large lattice volumes. On the other hand the ϵ–regime is defined when the pion Compton wavelength extends over the sizes of the physical volume. One uses the fact that the finite size effects appearing in this regime are controlled by the low energy constants of the infinite volume. In this Chapter we explore the product Lm_π in the definition of the p– and ϵ–regime.

The pion mass in the infinite volume is extracted from a time exponential decay of the pseudo-scalar correlator $a^3 \sum_{\vec{x}} \langle \mathcal{P}^b(\vec{x},t) \mathcal{P}^b(\vec{0},0) \rangle$. Here summation over b is not taken and the pseudo-scalar density $\mathcal{P}^b(x)$ was defined in Eq. (2.62). In the p–regime on a lattice of size $L^3 \times T$ this is modified to

$$a^3 \sum_{\vec{x}} \langle \mathcal{P}^b(\vec{x},t) \mathcal{P}^b(\vec{0},0) \rangle = \frac{|\langle 0|\mathcal{P}^b|\mathrm{pion}\rangle|^2}{m_\pi} e^{-m_\pi \frac{T}{2}} \cosh\left[m_\pi \left(t - \frac{T}{2} \right) \right] \ . \ (5.1)$$

As the bare quark mass m_q is decreased, the contribution of the zero modes to the $\langle \mathcal{P}\mathcal{P} \rangle$ rises as $|\nu|/(m_q V)^2$, which is seen from the spectral representation of the pseudo-scalar correlator in Eqs. (2.65-2.67). On the other hand $|\nu| \sim \sqrt{V}$ (we anticipate the formula (7.5) for the topological susceptibility). In total the contribution of the zero modes is reduced as the physical volume V is increased. In full QCD simulations the configurations with topological charge ν would be suppressed compared to the quenched case due to the fermionic determinant by a factor $\prod_{q=1}^{N_f} m_q^{|\nu|}$. Therefore in our quenched simulations the sampling of the pseudo-scalar correlator has a systematic error hidden in the contribution of the zero modes. This error is increased for smaller m_q

and decreased for larger V. As it was pointed out in Ref. [97], the problem can be avoided by subtracting the scalar correlator $\langle \mathcal{S}^b(x)\mathcal{S}^b(y)\rangle$,

$$\mathcal{S}^b(x) = \bar{\psi}(x)iT^b\psi(x) \; , \tag{5.2}$$

which leads to the cancellation of the zero mode contributions. This happens due to their exact chirality. The proposed method introduces also an additional scalar mass to the spectrum of the $\langle \mathcal{PP} - \mathcal{SS}\rangle$ correlator. It is, however, expected to be much larger than the pion mass and therefore it should be visible only among the excited states which are usually suppressed at least by a factor of $\exp{(m_\pi - M_{\text{excited}})t}$.

We used the Neuberger operator as a regularization for fermions to extract the pion mass in quenched QCD simulations on $12^3 \times 24$ lattice at $\beta = 5.85$. To calculate the pseudo-scalar correlation function the Dirac operator has to be inverted as in Eq. (2.63) at a bare quark mass m_q which is introduced as

$$D_{\text{ov}}(m_q) = \left(1 - \frac{m_q}{2\mu}\right) D_{\text{ov}} + m_q \; . \tag{5.3}$$

We approximated the square root appearing in D_{ov} with the Chebyshev polynomials to accuracy 10^{-15}. Descriptions of highly optimized algorithms to invert the overlap operator is given in Refs. [98–101]. In particular we use the multiple mass solver [102]. The quark masses were chosen to lie in the range where the p–regime is applicable so that the exponential decay of the pseudo-scalar correlator can be used. The lowest considered quark mass corresponds to the cross-over of the p–regime to the ϵ–regime. In Table 5.1 and in Figure 5.1 the quark masses and the pion masses extracted from the $\mathcal{PP}$ as well as $\mathcal{PP} - \mathcal{SS}$ correlators are reported [103]. We see that the deviation between the two methods becomes larger as the quark mass is decreased. We also give the product $m_\pi L$ to quantify the the p–regime. In Figure 5.1 we also show the chiral extrapolation by a linear fit of the square of the pion mass vs. the quark mass down to $m_q = 0$. We see that the linear behavior is reproduced well for the pion mass calculated with the $\langle \mathcal{PP} - \mathcal{SS}\rangle$ correlator. The intercept amounts to $-0.002(6)$. For the lowest quark mass $m_q = 0.01$, which is in the domain of the cross over to the ϵ–regime, we found $m_\pi L = 1.68$. This is quite small and therefore the finite size effects on the pion mass cannot be neglected.

To fix the physical scale we used the Sommer scale r_0, see Refs. [104, 105]. It was computed for the considered range of β in Ref. [106]
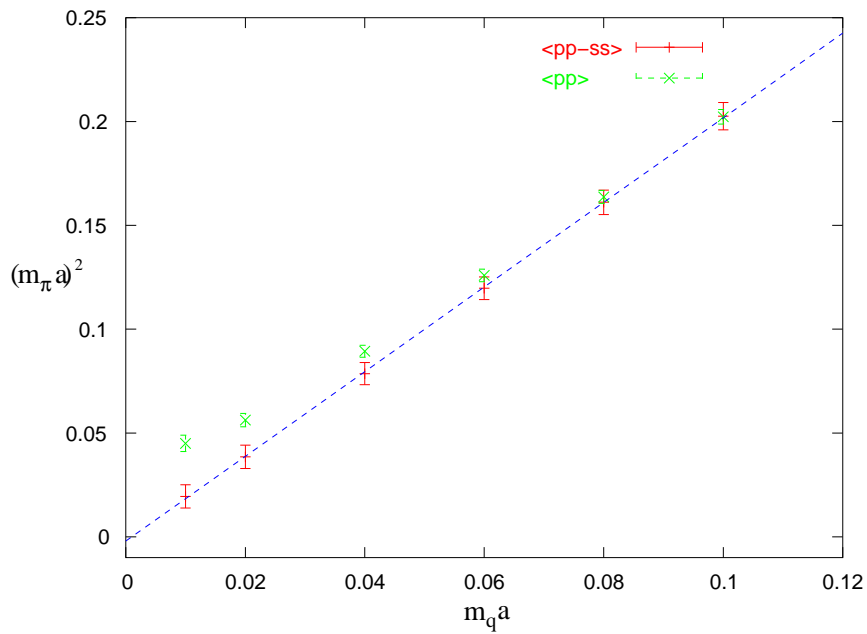
Figure 5.1: The square of the pion mass m_π^2 vs. the bare quark mass computed both for $\langle \mathcal{PP} - \mathcal{SS} \rangle$ and $\langle \mathcal{PP} \rangle$ correlators. The data for $\langle \mathcal{PP} - \mathcal{SS} \rangle$ can be linearly extrapolated to $m_q a = 0$ with an intercept compatible with $m_\pi^2 a^2 = 0$.

$m_q a$	$m_\pi^{\mathcal{P}} a$	$m_\pi^{\mathcal{P}-\mathcal{S}} a$	$m_\pi^{\mathcal{P}-\mathcal{S}} L$
0.01	0.212(9)	0.140(20)	1.68
0.02	0.237(7)	0.196(14)	2.35
0.04	0.299(5)	0.280(10)	3.36
0.06	0.355(4)	0.346(8)	4.15
0.08	0.405(4)	0.401(7)	4.81
0.10	0.450(4)	0.451(6)	5.41

Table 5.1:   The pion mass m_π calculated from 140 configurations for the $\langle \mathcal{PP} \rangle$ and for the $\langle \mathcal{PP} - \mathcal{SS} \rangle$ correlators. The products $m_\pi L$ are also shown. At $m_q a = 0.01$ we obtain the pion mass $m_\pi^{\mathcal{P}-\mathcal{S}} \approx 225$ MeV.

Chapter 6

Eigenvalue distributions of the overlap Dirac operator

Since the individual distributions of the eigenvalues of the Dirac operator were only conjectured in the framework of the χRMT, it is of interest to compare these predictions to the corresponding eigenvalue distributions obtained from QCD lattice simulations with chiral fermions.

The Wilson Dirac operator seems hardly suitable in this respect; because of the mass renormalization it would be highly problematic to identify the zero modes and the relative values of the remaining modes. In addition, quenched simulations at small quark masses are plagued by the occurrence of accidentally extremely small unphysical eigenvalues which is known as exceptional configurations.

Staggered fermions do not suffer from additive mass renormalization because they have an exact remnant chiral symmetry $U(1) \otimes U(1)$. Indeed such comparisons exist. The staggered fermion spectrum agrees well with the χRMT prediction in the sector $\nu = 0$. However, it turns out that all other sectors, $\nu \neq 0$, yield the same distributions, in particular the same histogram for $\rho_1^{(\nu)}(z)$ in QCD [107, 108]. It seems that staggered fermions are generally insensitive to the topology, and therefore not adequate in their conventional formulation for this purpose, at least for moderate and strong gauge coupling. However, latest studies with improved staggered fermions, where the mixing of the pseudo-flavors is suppressed, showed that the sensitivity can be recovered [109–111]. There is also an indication that the sensitivity of the conventional staggered fermions becomes better as we approach the continuum limit. This was suggested in Ref. [112] where a study with the Schwinger model was presented.

The lattice studies of the distributions of individual eigenvalues with the GW fermions were pioneered in Ref. [113] where the eigenvalues of the overlap

operator and the fixed point operator were considered for the Schwinger model. In both cases the results agreed with the χRMT formulae.

Such studies were also performed with the overlap operator in 4d QED [114] and again the predictions were successful within the statistical errors.

Finally QCD was considered, but initially just on tiny lattices of size 4^4. Ref. [115] used the overlap operator at strong coupling of $\beta = 5.1$ which in our opinion corresponds to too strong coupling regime where the overlap formula cannot be safely applied, as we pointed out in Chapter 3. Ref. [116] applied a truncated fixed point action and obtained a decent agreement in a volume of $V = (1.2\,\text{fm})^4$. However, when the physical lattice spacing is decreased so that the volume shrinks to $(0.88\,\text{fm})^4$, the leading non-zero eigenvalue distributions of the different topological sectors are on top of each other, in contrast to the χRMT prediction.

6.1 Microscopic regime

In this Section we discuss our results for the individual eigenvalue distributions of the overlap Wilson Dirac operator. Most of them were published in Ref. [117].

Due to the computational time required by the overlap operator we had to use the quenched approximation, as it was also the case in all previous studies mentioned above. We generated quenched $SU(3)$ gauge fields with the Wilson gauge action (2.110) with periodic boundary conditions. We used moderate gauge couplings, $\beta \geq 5.85$ and chose the mass μ in the overlap formula in a way to render the operator optimally local. In particular we took $\mu = 1.4$ for $\beta = 6$ and $\mu = 1.6$ for $\beta = 5.85$. We approximated the inverse square root by Chebyshev polynomials to an accuracy of $\epsilon_{\text{overlap}} = 10^{-12}$ for lattices of volume 8^4, 10^4, 12^4. Then we used the PARPACK routines [118, 119] to evaluate up to 100 eigenvalues of the overlap Wilson Dirac operator with the least absolute value. The index for each configuration was identified by computing eigenvalues of the operator γ_5 for the leading modes. They came out to be ± 1 to a very high accuracy for the zero modes. The corresponding zero eigenvalues on the 10^4 lattice at $\beta = 5.85$ were of order 10^{-10} to 10^{-6}, and the first non-zero eigenvalues were in the range about 10^{-3} to 10^{-2}. So there was a large gap between non-zero and zero eigenvalues, which allowed us to safely identify the zero modes. Then the index was read off from the chirality of the corresponding eigenvectors. To illustrate this we show in Table 6.1 an example of the eigenvalues and the chirality of the corresponding eigenvectors of the Neuberger operator in topological sectors $\nu = 0$ and -2.

Of course the non-zero eigenvalues occur in complex conjugate pairs, hence

EV of $D_{ov}^\dagger D_{ov}$	EV of γ_5
example for charge $\nu = 0$	
$6.23013e-3$	0.3608201
$6.23014e-3$	-0.3608198
$9.90174e-3$	-0.7622260
$9.90177e-3$	0.7622260
$2.69086e-2$	-0.7528350
example for charge $\nu = -2$	
$6.03761e-16$	-1.0000000
$9.43764e-11$	-0.9999999
$3.68203e-3$	-0.9240370
$3.73623e-3$	0.9205659
$7.04176e-3$	-0.7016518

Table 6.1: *Typical examples for the lowest eigenvalues of $D_{ov}^\dagger D_{ov}$ on a $10^3 \times 24$ lattice at $\beta = 6$.*

we will consider only one sign for the imaginary part below. Our statistics in various topological sectors is collected in Table 6.2. To fix the physical scale we again used the Sommer scale r_0 introduced in Chapter 5.

6.1.1 Distributions of individual eigenvalues

In this Subsection we discuss the probability distributions of the individual lowest eigenvalues of the overlap Wilson Dirac operator.

In order to relate the eigenvalues found on the Ginsparg-Wilson circle to the continuum eigenvalues λ_n, we map the circle stereographically onto the imaginary axis. Requiring $f(z) = z + \mathcal{O}(z^2)$ and $f(2\mu) = \infty$ singles out the Möbius transform

$$f(z) = \frac{z}{1 - z/(2\mu)} \ . \tag{6.1}$$

This mapping has been suggested before in Refs. [120, 121], for instance, in connection with the Leutwyler-Smilga sum rules [120].

The results for the distribution of the lowest eigenvalue of the overlap Wilson Dirac operator can be represented by a histogram, which then could be compared to Figure 2.1. However, such a picture depends on the arbitrary choice of the bin size in the histogram. This can be avoided by calculating the cumulative density, which sums up all the entries up to the considered value of z — it is normalized so that the full number of entries corresponds to the

lattice size	β	μ	physical volume	number of configurations $\nu = 0$	$|\nu| = 1$	$|\nu| = 2$
8^4	5.85	1.6	$(0.98\,\text{fm})^4$	80	63	28
12^4	6	1.4	$(1.12\,\text{fm})^4$	44	70	24
10^4	5.85	1.6	$(1.23\,\text{fm})^4$	74	112	84
$16^3 \times 32$	6	1.4	$(1.49\,\text{fm})^3 \times 2.98\,\text{fm}$	49	87	63

Table 6.2: The statistics of our simulations on four lattice sizes.

cumulative density 1. The resulting cumulative densities can be compared to the analytical curves of the cumulative density of the χRMT prediction for the kth eigenvalue in the topological sector ν,

$$\rho_{k,c}^{(\nu)}(z) = \frac{\int_0^z \rho_k^{(\nu)}(z')\,dz'}{\int_0^\infty \rho_k^{(\nu)}(z')\,dz'} \ . \tag{6.2}$$

The chiral condensate enters these analytical formulae as the only free parameter. Therefore, applying a one parameter fit to the data in various topological sectors it is possible to obtain an estimate for its bare quenched value.

We note in passing that the absolute values of the eigenvalues of the operator $\gamma_5 D_{\text{ov}}$ are equal to absolute values of the $\sqrt{D_{\text{ov}}^\dagger D_{\text{ov}}}$. Moreover the stereographically projected eigenvalues of the operator D_{ov} can be related to the Hermitian eigenvalues by the simple formula [100, 122],

$$\left| \frac{\lambda_j}{1 - \lambda_j/(2\mu)} \right| = \frac{|\lambda_j^H|}{\sqrt{1 - (\frac{1}{2\mu}\lambda_j^H)^2}} \ , \text{ where} \tag{6.3}$$

$$D_{\text{ov}}\psi_j = i\lambda_j\psi_j \ , \quad \gamma_5 D_{\text{ov}}\phi_j = i\lambda_j^H\phi_j \ . \tag{6.4}$$

We start the discussion of the cumulative distributions for our smallest physical volume of $(0.98\,\text{fm})^4$ in Figure 6.1. Here the lines represent the predictions by χRMT for the lowest eigenvalue of the Dirac operator in the topological sectors $|\nu| = 0$, 1 and 2, and the symbols the cumulative distribution of the overlap Wilson Dirac operator. One can see a clear disagreement with the χRMT curves. In particular the sensitivity of the data to the topological charge is lost to a large extent. Notice that for very small values of z the data are closer to the analytical predictions. However, this does not allow for a reasonable fitting procedure to extract the chiral condensate Σ.

Now we consider a larger physical volume of $(1.12\,\text{fm})^4$. It corresponds in our simulations to a 12^4 lattice volume at $\beta = 6$. The plot is depicted in
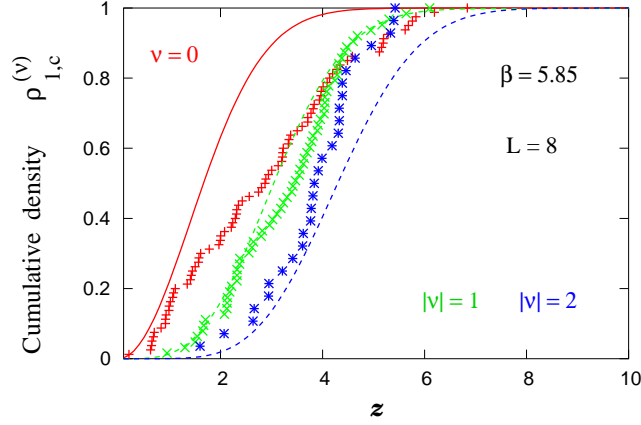
Figure 6.1: The cumulative distribution of the lowest non-zero eigenvalue of the overlap Wilson Dirac operator on 8^4 lattice, at $\beta = 5.85$ in the topological sectors $|\nu| = 0, 1, 2$ vs. χRMT predictions (lines). No agreement is found.
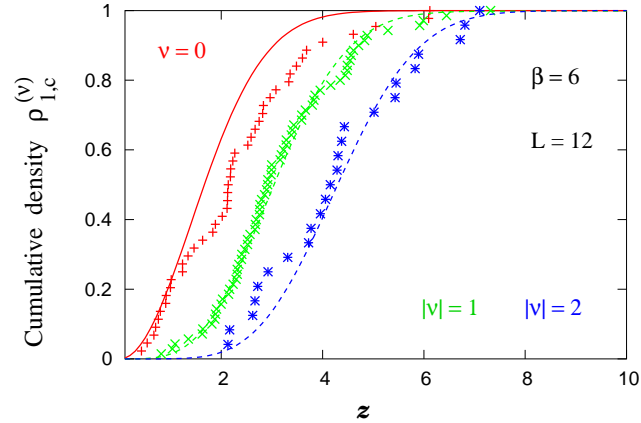
Figure 6.2: The cumulative distribution of the lowest non-zero eigenvalue of the overlap Wilson Dirac operator on 12^4 lattice, at $\beta = 6$ in the topological sectors $|\nu| = 0, 1, 2$ vs. χRMT predictions at $\Sigma = (256\,\text{MeV})^3$ (lines). A reasonable agreement is observed.
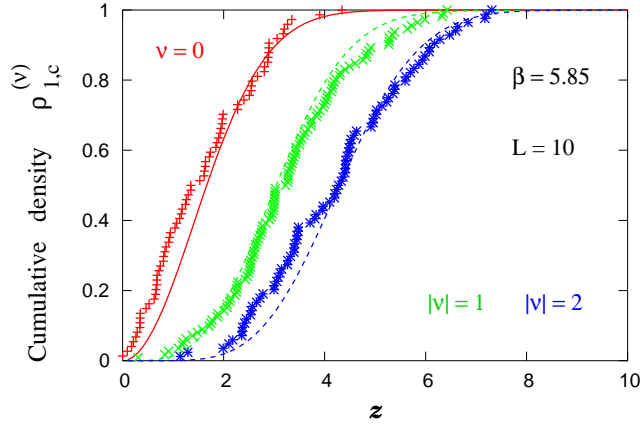
Figure 6.3: The cumulative distribution of the lowest non-zero eigenvalue of the overlap Wilson Dirac operator on 10^4 lattice, at $\beta = 5.85$ in the topological sectors $|\nu| = 0$, 1, 2 vs. χRMT predictions at $\Sigma = (253\,\mathrm{MeV})^3$ (lines). A good agreement is observed.

Figure 6.2. One can see that the agreement starts to set in. We interpret this picture as a satisfactory agreement with the predictions by the χRMT. In particular, we do see the effect that the peak of the density, resp. the interval of steepest ascent of the cumulative density, moves to larger values of z for increasing topological charge $|\nu|$. The plot is shown for the optimal value of the chiral condensate $\Sigma = (256\ \mathrm{MeV})^3$.

Next we studied a 10^4 lattice at $\beta = 5.85$, which corresponds to a somewhat larger physical volume of $V = (1.23\,\mathrm{fm})^4$. Again the results for the leading non-zero eigenvalue are shown for the topological sectors $|\nu| = 0$, 1 and 2 in Figure 6.3. We interpret the results to be in a good agreement with the χRMT predictions. The optimal value of the chiral condensate is modified to $\Sigma = (253\mathrm{MeV})^3$.

Finally we looked at the lattice size $16^3 \times 32$, at $\beta = 6$ which corresponds to a yet larger volume of $(1.49\,\mathrm{fm})^3 \times 2.98\,\mathrm{fm}$. In Figure 6.4 we show the cumulative densities of the lowest eigenvalue in topological sectors $|\nu| = 0$, 1 and 2 for $\Sigma = (286\,\mathrm{MeV})^3$. We interpret it again as a good agreement.

χRMT predicts a (logarithmically) increasing $\Sigma(V)$ due to quenching [123]. A conclusive verification of this behavior (beyond possible lattice artifacts) would require further simulations.

In Figure 6.5 we show the cumulative distributions of the next-to-lowest eigenvalue in the topological sectors $|\nu| = 0$, 1 and 2. The data we take from simulations on 10^4 and 12^4 lattices. Here we do not find a convincing agreement with the χRMT predictions; note that the relevant values of z are larger compared to Figure 6.2. Also the second non-zero eigenvalue moves
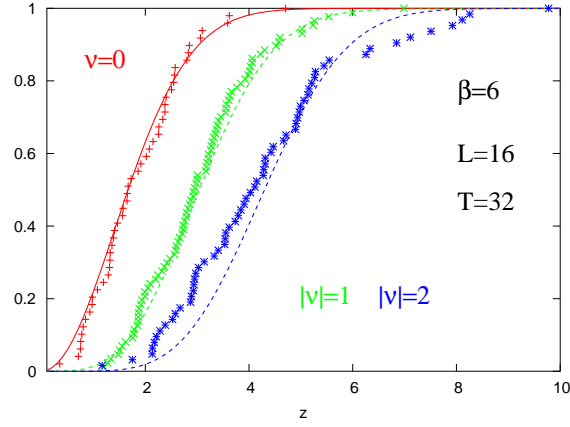
Figure 6.4: The cumulative distribution of the lowest non-zero eigenvalue of the overlap Wilson Dirac operator on $16^3 \times 32$ lattice, at $\beta = 6$ in the topological sectors $|\nu| = 0$, 1, 2 vs. χRMT predictions at $\Sigma = (286\text{MeV})^3$ (lines). A good agreement is observed.
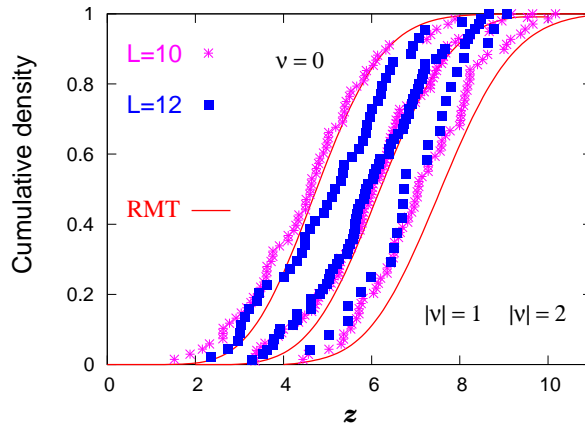
Figure 6.5: The results for the cumulative distribution of the next to lowest eigenvalue in topological sectors $|\nu| = 0$, 1, 2 for two lattice volumes 10^4 and 12^4 vs. the χRMT predictions (lines). No convincing agreement is observed.

lattice size	β	optimal Σ	confidence level		
			$\nu = 0$	$|\nu| = 1$	$|\nu| = 2$
12^4	6	$(256\text{MeV})^3$	0.003	0.73	0.79
10^4	5.85	$(253\text{MeV})^3$	0.03	0.48	0.10
$16^3 \times 32$	6	$(286\text{MeV})^3$	0.7	0.8	0.12

Table 6.3: The results for the chiral condensate and the statistical confidence level according to the Kolmogorov-Smirnov test.

to larger values of z if $|\nu|$ increases.

To quantify the quality of the fit we used the Kolmogorov-Smirnov test [92]. This test provides a confidence level that the given data set is drawn from the probability distribution of interest. In Table 6.3 we collect the confidence levels and the optimal values for Σ on the lattice volumes where we found a reasonable agreement with the χRMT. We see that the box length of 1.2 fm constitutes the lower bound of applicability of the χRMT predictions. We do not observe a full agreement. However, one can argue that the separation of the topologies for the lowest eigenvalue has set in to a large extent, and the box length is sufficient to obtain a good estimate for the chiral condensate.

The observation that there is a minimal physical box length where the χRMT predictions set in can be interpreted in terms of the so-called Thouless energy, a term that originates from mesoscopic physics (see the Review [124] on more details). The χRMT predictions become valid once we ensure that the simulations are performed in the ϵ–regime of the χPT. This can be estimated if we require the potential term in the Lagrangian of the χPT (2.37) to dominate over the kinetic term. Applying this argument to the characteristic scale of Dirac eigenvalues we arrive at

$$\lambda \ll \lambda_{\text{Thouless}} = \frac{F_\pi^2}{\sqrt{V}\Sigma} \ , \tag{6.5}$$

or converting this to the dimensionless variable: $z_{\text{Thouless}} = F_\pi^2 \sqrt{V}$. The above relation can also be obtained from the lower bound in the relation (2.3.2) by taking its square and recalling the formula for the pion mass through the quark mass, see Subsection 2.3.1. The determination of the value of z where the χRMT predictions fail can be considered as an empirical value for the Thouless energy. Thus the Thouless energy sets a limit on the value of eigenvalues where the χRMT applies. On the other hand one has to ensure that the physical volume is large enough to be in the confinement phase where all assumptions for the χPT are made. In addition one has to keep

in mind the relation (2.43) ensuring that the χPT expansion is defined. The latter imposes on the physical extent the requirement $L \gg 1/(2F_\pi) \sim 1\,\mathrm{fm}$.

To check the condition (6.5) one can perform the same eigenvalue study at rather large fixed physical volume and different lattice spacings a. Due to the renormalization of F_π and Σ this will lead to different Thouless energies and therefore it should be seen in the behavior of the corresponding cumulative distributions. In fact such a study was done in Ref. [125], but no ultimate confirmation of this behavior was found.

6.1.2 Spectral density

In this Subsection we discuss the microscopic spectral density of the overlap Wilson Dirac operator. We still separate topological sectors, but now we consider the distributions of all computed eigenvalues. We show the eigenvalue distributions for topological sector $|\nu| = 1$ and two lattice volumes, 10^4 and 12^4, in Figure 6.6. χRMT predicts an oscillating behavior (2.98) [47], which is also plotted for comparison. However, here we omit the zero eigenvalues, hence the term with the delta function drops out. We find a good agreement roughly up to the second peak, as expected from Figures 6.2, 6.3 and 6.5. Then we are leaving the microscopic regime and turn to the bulk. The Thouless energy appears in this context as a value of z where we leave the microscopic regime.

If the oscillation is averaged to a plateau, its height agrees well with the eigenvalue density at zero according to the Banks-Casher relation, $\rho(z = 0) = \rho(\lambda = 0)/\Sigma V = 1/\pi$.

6.2 Bulk eigenvalues

In this Section we discuss the eigenvalues in the bulk of the Dirac spectrum. It is expected that the spectral density in the deep bulk domain has a λ^3 behavior. Since we were able to compute as many as 50 conjugate pairs of eigenvalues of the overlap Wilson Dirac operator we can analyze the spectral density in the bulk. The largest eigenvalue corresponds to an energy of about 800 MeV. However, it is difficult to argue whether the considered domain is sufficiently large to accommodate the λ^3 behavior. In Figure 6.7 at the bottom we plot the eigenvalue spectral density for the topological sector $\nu = 1$ on the lattice 12^4 against the λ^3 curve, which we take to be $a + bz^3$. The data follow amazingly well the predicted behavior.

Now we want to make a remark on the Banks-Casher relation. If we were not able to obtain information from the microscopic regime and we had only
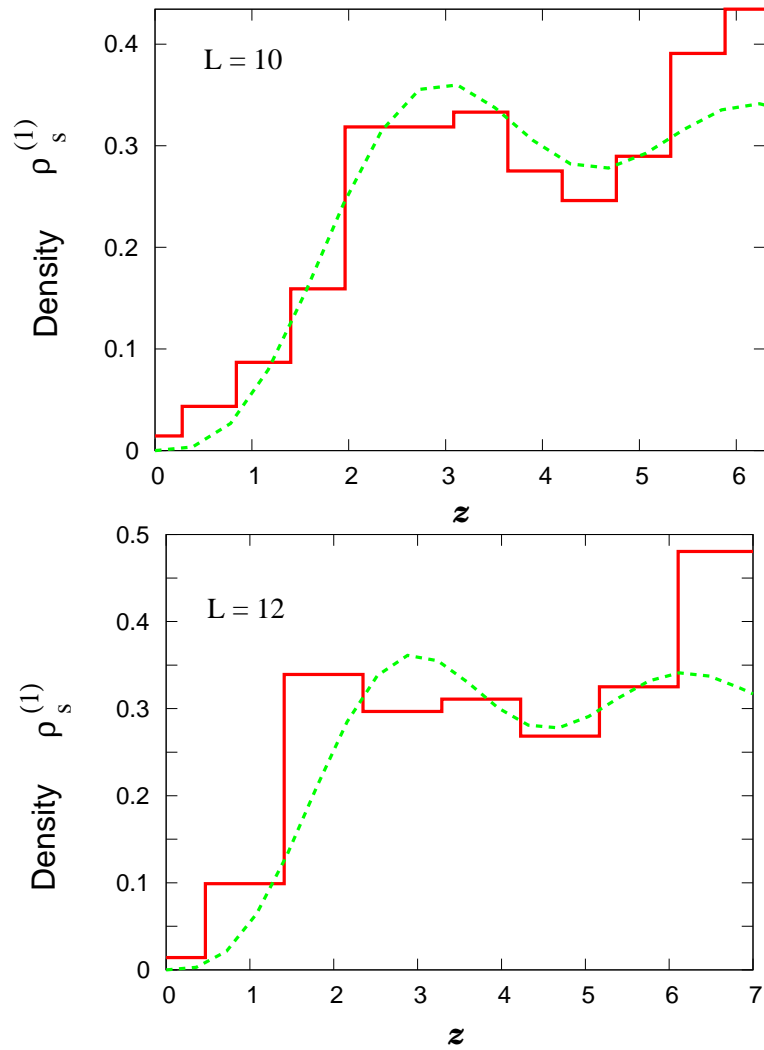
Figure 6.6: The results on the microscopic spectral density $\rho_s(z)$ in topological sectors $|\nu| = 1$ for two lattice volumes 10^4 and 12^4 vs. the χRMT predictions (lines).
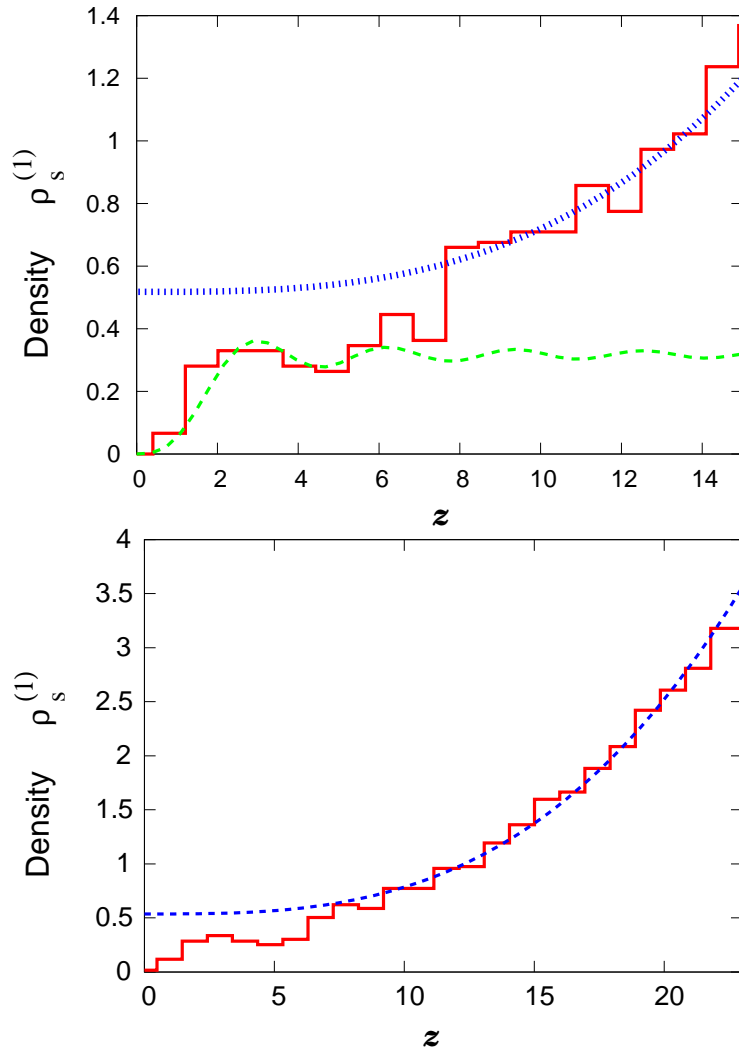
Figure 6.7: The upper plot shows the spectral density $\rho_s(z)$ in the bulk vs. the microscopic regime. One line corresponds to $a + bz^3$ and another to the microscopic spectral density. The plot at the bottom shows the spectral density in the bulk. The cross-over from the microscopic regime to the bulk is nicely seen.

the eigenvalues in the bulk, then the chiral condensate which would follow from the approximation of the eigenvalue density would be overestimated. This can be seen from the plateau extrapolated to low values of z on the Figure 6.7 on the top. For illustration we plot two curves for the bulk and the microscopic regime.

6.2.1   The unfolded spectrum

We now turn to another way of comparing our lattice data to a conjecture from χRMT. This additional evaluation allows us to take all our non-zero eigenvalues into account (for one sign of the imaginary part, i.e. up to 50 for each configuration). We build from all the eigenvalues of all configurations the *hierarchically unfolded distribution* as described for instance in Ref. [115]. For a comprehensive review and other ways of unfolding we refer for instance to Ref. [124].

To construct the hierarchically unfolded spectrum we first numerate all available non-zero eigenvalues with positive imaginary part in each configuration in ascending order, given by the angle in the Ginsparg-Wilson circle. Then we put all these eigenvalues from all configurations together and numerate them again in ascending order. Now we consider pairs of eigenvalues from the same configuration, which follow immediately one after the other in the original numeration. If they differ in the global numeration by k, then k/N_{conf} is the hierarchically unfolded level spacing, where N_{conf} is the number of configurations involved. In Figure 6.8 we show our results for the corresponding level spacing distribution in $V = 12^4$, $\beta = 6$, and in $V = 8^4$, $\beta = 5.85$. The histograms are compared to RMT conjectures for different groups and representations, and we can confirm a good agreement with the Wigner distribution predicted for $SU(3)$ in the fundamental representation. We conclude that this property holds over a large range of volumes. Since we include all our eigenvalues here, our statistics is much larger than in the plots for the microscopic regime. Note, however, that this analysis is not sensitive to the topology any more. There is no physics information such as values for the condensate or the pion decay constant, because one does not keep track of a physical scale. The hierarchically unfolded distribution only tests the correct symmetry group that is to be taken in RMT. Nevertheless, the hierarchically unfolded distribution provides a non-trivial and successful test for χRMT.
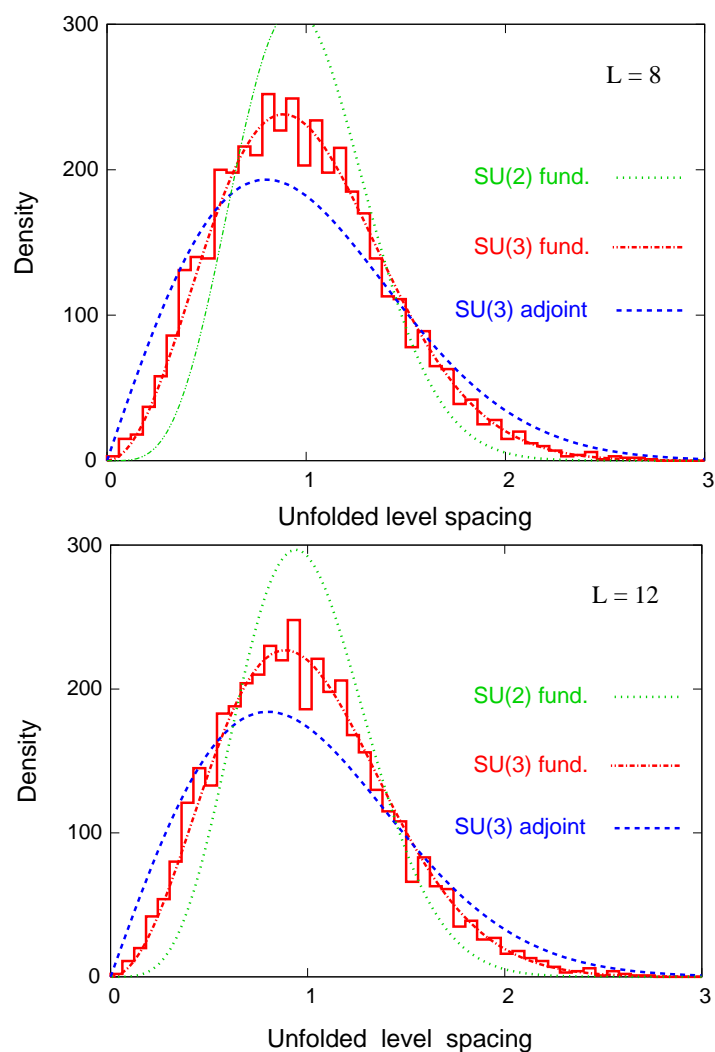
Figure 6.8: The hierarchically unfolded level spacing distributions. For comparison we show the curves for $SU(2)$ and $SU(3)$ fundamental representation and for $SU(3)$ adjoint representation.

Chapter 7

Topological susceptibility

7.1 Motivation

The topological susceptibility for a Yang-Mills gauge theory is defined by

$$\chi_t = \frac{1}{V} \int d^4x d^4y \, \langle q(x)q(y) \rangle_{\text{YM}} \,, \qquad (7.1)$$

where $q(x)$ is a density of the topological charge $Q = \int d^4x \, q(x)$ and the subscript YM means that the average is normalized by the partition function. We refer to quenched QCD, although the topological susceptibility also exists in the dynamical case. The main reason to look at the quenched topological susceptibility comes from the Witten-Veneziano formula [126, 127]. It is motivated by the inability of the constituent quark model to describe a large mass of the η' meson. The Witten-Veneziano formula predicts that at the leading order in the N_f/N_c expansion, with N_f being the number of flavors and N_c the number of colors, the contribution to the η' mass due to the $U_A(1)$ anomaly is given by

$$m_{\eta'}^2 = \frac{2N_f}{F_\pi^2} \chi_t \,. \qquad (7.2)$$

In the absence of the anomaly one could argue that $U_A(1)$ symmetry would be broken spontaneously leading to a massless Goldstone boson for massless quarks. However, a particle with the corresponding quantum numbers is not found, which is attributed to the existence of the $U_A(1)$ anomaly.

To interpret Eq. (7.1) one has to find a properly normalized topological density $q(x)$ and to subtract from the quantity $q(x)q(0)$ an appropriate contact term to define it properly in the continuum limit.

In the case of Ginsparg-Wilson fermions the topological density can be

determined by

$$q_x = \frac{1}{2a^3} \text{Tr}[\gamma_5 D[U]_{x,x}] \ , \tag{7.3}$$

where the trace is taken over color and spinor indices of a Ginsparg-Wilson operator D. It can be shown that this definition leads to a properly defined topological charge and to the Atiyah-Singer index theorem [69, 70, 128, 129]. In Ref. [130] it was also demonstrated that this discretization naturally enters the Witten-Veneziano formula if we consider Ginsparg-Wilson regularization for the fermions

$$m_{\eta'}^2 = \frac{2N_f}{F_\pi^2} \lim_{\substack{V \to \infty \\ a \to 0}} a^4 \frac{1}{V} \sum_{x,y} \langle q_y q_x \rangle_{\text{YM}} \ . \tag{7.4}$$

Note that due to the chiral symmetry of the fermions no additional subtraction is necessary [131]. Using Eq. (7.3) we obtain for the topological susceptibility

$$\chi_t = \lim_{\substack{V \to \infty \\ a \to 0}} \frac{\langle (N_+ - N_-)^2 \rangle_{\text{YM}}}{V} \ , \tag{7.5}$$

where N_+ and N_- is the number of zero modes of the Ginsparg-Wilson fermions with positive and negative chirality, respectively. This formula will be a starting point for the discussion of the results which we obtained using the overlap operator.

The study of the continuum limit of the topological susceptibility with the GW fermions was pioneered in Refs. [116, 125, 132, 133]. It is argued that the continuum extrapolated value of the topological susceptibility is about $\chi_t r_0^4 = 0.059 \pm 0.003$ [133], where $r_0 = 0.5 \, \text{fm}$.

7.2 Results with overlap fermions

We simulated quenched QCD on $L^3 \times T$ lattices with periodic boundary conditions and used the overlap Wilson Dirac operator, as well as the overlap hypercube Dirac operator, to determine the index of the gauge configurations. The configurations were simulated using the usual Monte Carlo procedure where we employed the heat bath and the overrrelaxation method as described in Subsection 3.1. We assume the configurations to be statistically independent, which we checked by measuring the autocorrelation time of the topological charge. It turned out to be below 0.5, which characterizes a completely decorrelated sample.

We considered several lattice volumes and in Table 7.1 we collect the topological susceptibility for the Neuberger operator as well as for the overlap hypercube operator.
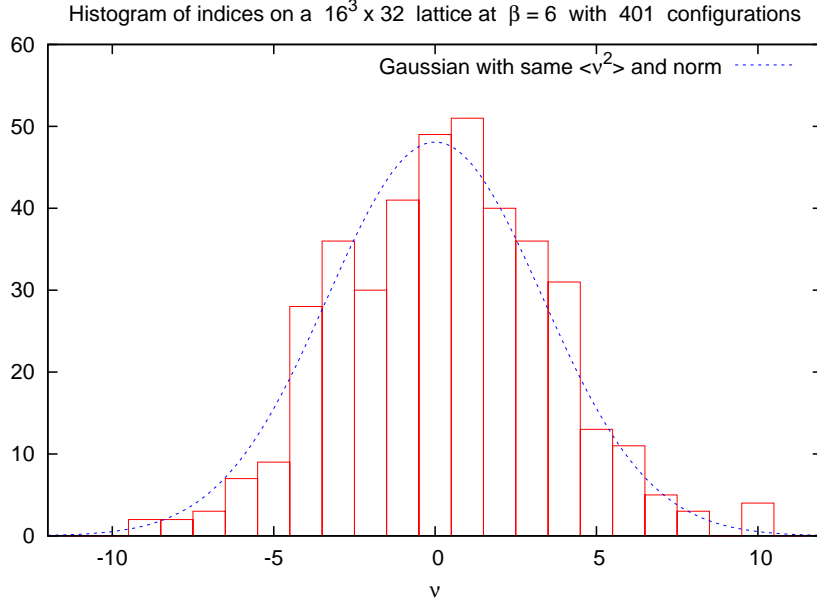
Figure 7.1: The charge histogram and the corresponding Gaussian distribution with the same $\langle \nu^2 \rangle$ and norm.

One expects a Gaussian charge distribution which is confirmed by our data, see Figure 7.1. In order to render the values of the topological susceptibility stable against the fluctuations due to a few entries of high charges ($|\nu| \geq 8$) on the lattice volumes $12^3 \times 24$ and $16^3 \times 32$ we applied the following method: we counted the number of entries q_ν in the interval $[-\nu - 0.5, \nu + 0.5]$ and normalized them to the total number of entries. Then we employed the formula

$$
\begin{aligned}
q_\nu &= \frac{1}{\sqrt{2\pi}} \int_{-u}^{u} \exp\left(-y^2/2\right) dy \ , \\
u &= \frac{|\nu| + 0.5}{\langle \nu^2 \rangle} \ ,
\end{aligned}
\tag{7.6}
$$

to extract the value of $\langle \nu^2 \rangle$ and thereby the topological susceptibility. We calculated it for $|\nu| = 1, 2, \ldots, 5$. Out of these values we computed a mean value and a standard deviation. In Table 7.2 the topological susceptibility calculated with this method is shown.

There are two issues when considering the topological susceptibility calculated on the lattice. First the finite size effects dependence of the topological susceptibility, which is governed by $\exp\left(-L M_{\text{glueball}}\right)$, where $M_{\text{glueball}} \approx 1.5$ GeV is the mass of the lightest glueball. Thus for lattices of $L \geq 1\,\text{fm}$ the
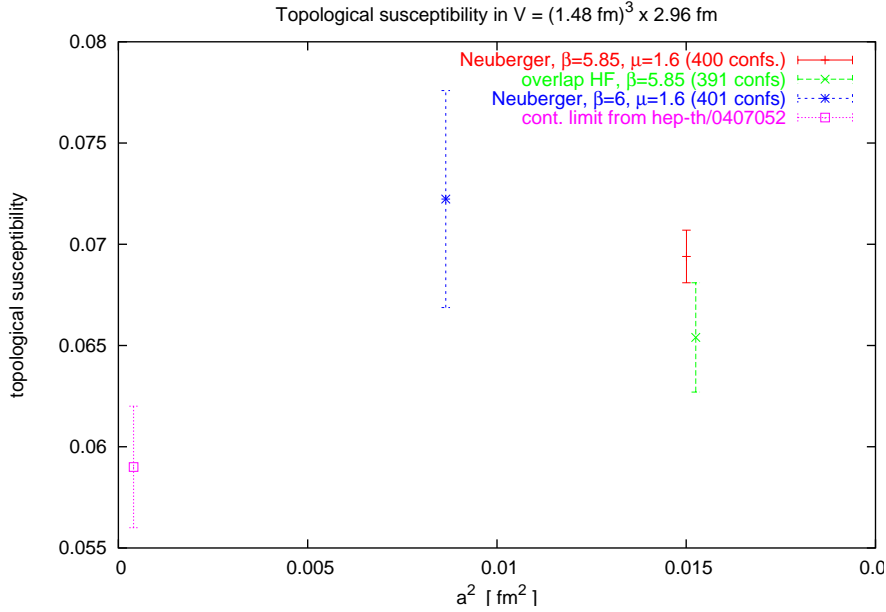
Figure 7.2: The topological susceptibility $\chi_t r_0^4$, calculated with the Neuberger operator and the overlap hypercube Dirac operator, vs. the square of the lattice spacing.

finite size effects on the topological susceptibility are expected to be far below our statistical errors. We see from Table 7.1 that at $\beta = 5.85$ and lattice volumes $V = 10^4$ and $12^3 \times 24$ the corresponding values of the topological susceptibility coincide within the error bars. Second, at finite lattice spacing a the topological susceptibility suffers from discretization effects starting from $\mathcal{O}(a^2)$.

In Figure 7.2 we plot the topological susceptibility calculated with the Neuberger operator and the overlap hypercube operator using Eq. (7.6) vs. the square of the lattice spacing. We fixed the physical volume to $(1.48\,\text{fm})^3 \times 2.96\,\text{fm}$. We show the results for the Neuberger operator for $12^3 \times 24$ volume at $\beta = 5.85$ and $16^3 \times 32$ at $\beta = 6$. The result for the overlap hypercube fermions is given for the volume $12^3 \times 24$ at $\beta = 5.85$. For comparison we also show the continuum extrapolated value from Ref. [133]. We see that the value of the topological susceptibility calculated with the overlap hypercube Dirac operator is closer to the continuum value than the corresponding value of the Neuberger operator. This result hints at an improved scaling behavior of the overlap HF, though further statistics and observables are needed to certify this trend.

operator	lattice size	β	μ	physical volume	$\chi_t r_0^4$	N_{conf}
Neuberger	12^4	6	1.4	$(1.12\,\text{fm})^4$	0.063 ± 0.008	143
Neuberger	10^4	5.85	1.6	$(1.23\,\text{fm})^4$	0.078 ± 0.006	308
Neuberger	$12^3 \times 24$	5.85	1.6	$(1.48\,\text{fm})^3 \times 2.96\,\text{fm}$	0.068 ± 0.0048	400
Neuberger	$16^3 \times 32$	6	1.4	$(1.49\,\text{fm})^3 \times 2.98\,\text{fm}$	0.073 ± 0.0053	401
overlap HF	$12^3 \times 24$	5.85	1	$(1.48\,\text{fm})^3 \times 2.96\,\text{fm}$	0.066 ± 0.0043	391

Table 7.1: The topological susceptibility calculated with the overlap hypercube Dirac operator and with the Neuberger operator using the standard deviation.

operator	lattice volume	β	μ	physical volume	$\chi_t r_0^4$	N_{conf}
Neuberger	$12^3 \times 24$	5.85	1.6	$(1.48\,\text{fm})^3 \times 2.96\,\text{fm}$	0.069 ± 0.0013	400
Neuberger	$16^3 \times 32$	6	1.4	$(1.49\,\text{fm})^3 \times 2.98\,\text{fm}$	0.072 ± 0.0054	401
overlap HF	$12^3 \times 24$	5.85	1	$(1.48\,\text{fm})^3 \times 2.96\,\text{fm}$	0.065 ± 0.0027	391

Table 7.2: The topological susceptibility calculated with the overlap hypercube Dirac operator and the Neuberger operator using Eq. (7.6)

Chapter 8

Mesonic two-point functions

8.1 The axial-vector correlator

In this Section we discuss results on the axial-vector correlator. Most of these results were published in Ref. [134]. We simulated quenched QCD with the Wilson gauge action on the lattices of size $10^3 \times 24$ and 12^4 at $\beta = 6$ with periodic boundary conditions. As a regularization scheme for the fermions we chose the overlap Wilson Dirac operator. We calculated the axial-vector correlator according to formula (2.54). To this end we needed to invert the overlap Wilson Dirac operator at a small quark mass m_q. We approximated the square root appearing in D_{ov} with Chebyshev polynomials to accuracy 10^{-16}. The statistics of the configurations for various topological sectors is given in Table 8.1. To compute the index we used PARPACK [118, 119] and Ritz functional methods [135, 136]. We kept the quark masses light enough in order to stay in the ϵ–regime. To quantify this condition, $z_q = m_q \Sigma V$ must be well below 1. In particular the considered quark masses were chosen in a way that $z_q \leq 0.34$. We determined the parameter F_π by making a fit with an additive constant in Eq. (2.61) at $\tau = 0.5$. Thus it can easily be computed. The chiral condensate Σ, on the other hand, is proportional to the curvature of the parabola. However, as the value of Σ varies in the range of interest, the corresponding parabola changes only very little which makes the extraction of Σ extremely difficult.

We find that the lattice size $10^3 \times 24$ at $\beta = 6$ is too small to accommodate the predictions by the χPT. In Figure 8.1 we show the data for the axial-vector correlator at quark mass $m_q = 21.3\,\mathrm{MeV}$, lattice volume $V = 10^3 \times 24$, at $\beta = 6$ for topological sectors $|\nu| = 1, 2$ along with the corresponding analytical predictions. We plot the analytical curves for two very distinct values of the chiral condensate, $\Sigma = 0$ and $\Sigma = (250\,\mathrm{MeV})^3$. We see that the re-
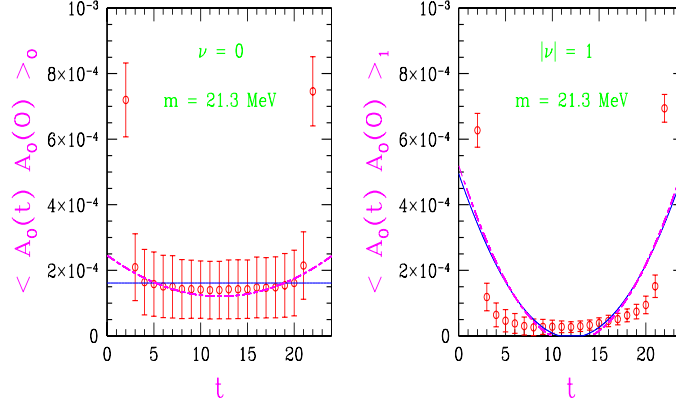
Figure 8.1: The axial-vector correlator computed at quark mass $21.3\,\mathrm{MeV}$ for a lattice volume $10^3 \times 24$ at $\beta = 6$. The left plot shows the axial-vector correlator for topological charge $\nu = 0$ and the right plot for $|\nu| = 1$. The result at $\nu = 0$ suffers from large error bars. In the sector $|\nu| = 1$ we see a clear failure to reproduce the qχPT predictions (curves).

sulting curves lie too close to each other to allow for Σ to be evaluated. The fact that those two curves are almost indistinguishable is valid for topological sectors $|\nu| \neq 0$. It is due to the last term in the expression (2.61). However in the topological sector 0 the sensitivity is restored. At $|\nu| = 1$ we see that the analytical prediction for this lattice volume does not model the data. The failure of the χPT to describe the result on volumes with box length less than $1.2\,\mathrm{fm}$ has been observed before in Section 6.1 where the distributions of eigenvalues of the overlap Wilson Dirac operator were confronted with the χRMT predictions. Thus this conclusion is rather general and sets a consistent constraint in the lattice simulations where the results can be confronted with χPT.

Next we consider the fit by the analytical prediction of the χPT to the simulation data on the volume 12^4 and topological sector $|\nu| = 1$. Our χRMT study of Dirac eigenvalues in Chapter 6 suggests that this volume should be at least at the threshold where the predictions by χPT become valid. The result is shown in Figure 8.2 (on the left) where we fit Eq. (2.61) to the simulation data, omitting the points located far from the center which are strongly affected by the contributions of the excited states. We can compute the additive constant that corresponds to F_π quite accurately. Figure 8.2 (on the right) shows the fitted value of F_π against the extension of the time interval where the fit was done. We find a decent plateau which suggests a value $F_\pi = 87 \pm 4\,\mathrm{MeV}$ for the quenched, bare pion decay constant. Again the chiral condensate cannot be extracted from these data. This we demonstrate
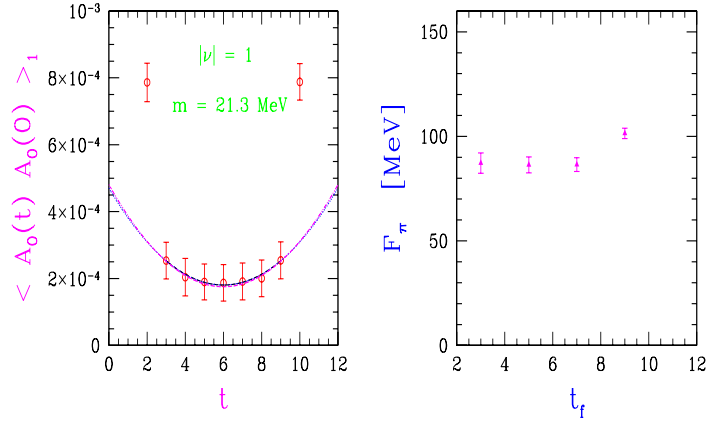
Figure 8.2: The fit of the quenched QCD simulation data for the axial-vector correlator vs. the analytical predictions by χPT (left plot). The curves represent the qχPT predictions for $\Sigma = 0$ and $\Sigma = (250\,\text{MeV})^3$. The extracted value of F_π vs. number of points t_f for the fit range around $t/T = 0.5$ (is shown on the right plot). The lattice volume is 12^4, $\beta = 6$, $|\nu| = 1$ and $m_q = 21.3\,\text{MeV}$.

in Figure 8.2 (on the left) where we plot the analytical prediction for two cases $\Sigma = 0$ and $\Sigma = (250\,\text{MeV})^3$. We see that the resulting curves reside within the error bars and hence make the determination of Σ impossible. Finally we look at the simulation data on 12^4 lattice at $\beta = 6$ for the topological sector $|\nu| = 2$. To check whether the data agree with the analytical predictions we varied F_π in the range that we found from the fit in the topological sector $|\nu| = 1$. The resulting shaded area is shown in Figure 8.3. We conclude that the data for the topological sectors $|\nu| = 1$ and 2 agree within the errors. Note that the agreement at $|\nu| = 2$ is, however, somewhat worse than for the topological sector $|\nu| = 1$ (the data are more flat). This is, in fact, in agreement with the χRMT study of the eigenvalues of the Dirac operator, where we found that the agreement with the χRMT is expected to be worse as we increase the topological sector $|\nu|$.

We obtained of course the bare values for F_π which are still subject to the renormalization. The latter is expected to increase the bare values substantially. [103, 137].
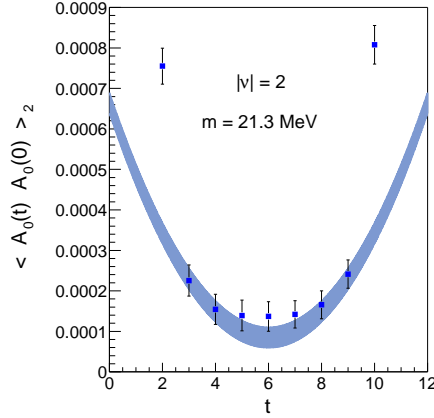
Figure 8.3: The quenched QCD simulation data for the axial-vector correlator vs. the analytical predictions with the parameter F_π in the range that was found by fitting in the topological sector $|\nu| = 1$ (shaded area). The lattice volume is $V = 12^3$, at $\beta = 6$, for topological charge $|\nu| = 2$. The quark mass is $m_q = 21.3\,\text{MeV}$.

8.2 Subtleties of numerical simulations in the ϵ–regime

In this Section we address the practical side of the simulations in the ϵ–regime.

In the ϵ–regime the sector of topological charge $\nu = 0$ may appeal as a good candidate where the chiral condensate can be extracted since the expression (2.61) does not show such an insensitivity to Σ as it is the case for non-zero topological sectors. Unfortunately, this sector is not favorable for the numerical simulations because of the frequently occurring small eigenvalues. As we saw in Section 2.4 and in Chapter 6, where we studied the probability distribution of the lowest eigenvalues, it is the topological sector $\nu = 0$ where we observe a high probability of very small eigenvalues λ_1. As we increase the topological charge, the corresponding probability is suppressed, see for instance Figures 2.1 and 6.3. This behavior is reflected in the relatively large error bars for the axial-vector correlator in the topological sector 0, illustrated in Figure 8.1. We can demonstrate this explicitly by showing how the axial-vector correlator is sampled for the topological sectors 0 and 1. In Figure 8.4 the Monte Carlo histories of $A_0(t)A_0(0)|_{\nu=0}$ and $A_0(t)A_0(0)|_{|\nu|=1}$ are shown. In particular we see strong spikes in the history of the axial-vector correlator for the neutral topological sector. We checked the configurations where they show up. They correspond to cases of small eigenvalues of the
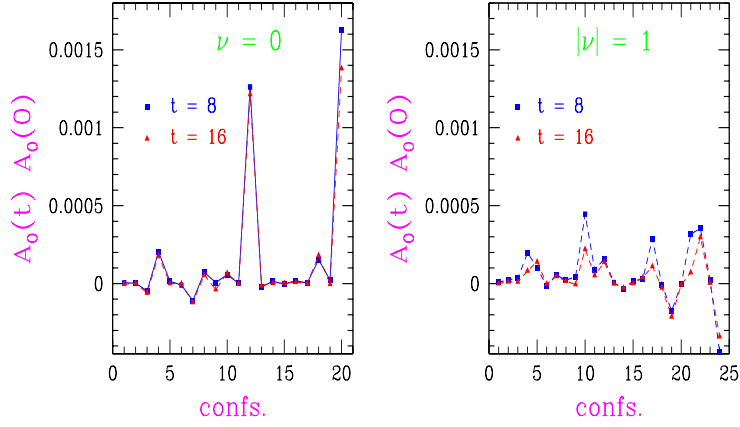
Figure 8.4: Monte Carlo histories of the axial-vector correlator for topological sector $\nu = 0$ (left plot) and topological sector $|\nu| = 1$ (right plot), at $V = 10^3 \times 24$, $\beta = 6$.
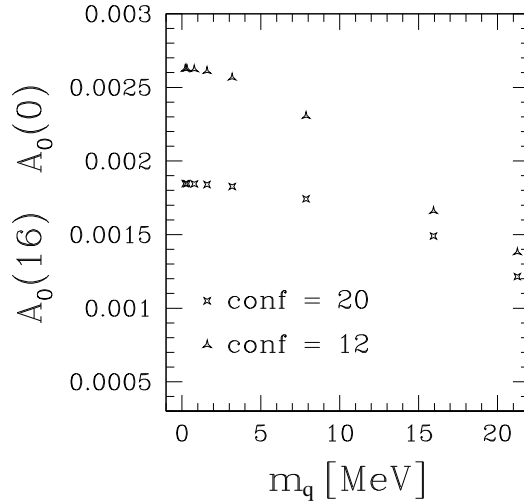
Figure 8.5: The height of the spikes vs. the bare quark mass.

overlap Wilson Dirac operator. The heights of the spikes become larger for smaller quark masses. This is shown in Figure 8.5. The height of the spikes rises monotonously in $\frac{1}{|\lambda_1|}$, where λ_1 is the lowest eigenvalue of the Dirac operator. This also holds for the spikes in the non-trivial sectors, where, however, the occurrence of such very small modes is suppressed. In practice one has to trade off the quark mass in a way first to ensure that it is small enough to be in the ϵ–regime and secondly to have it large enough to damp down the values of the spikes.

Now we want to trace the effect of the spikes on the statistics necessary
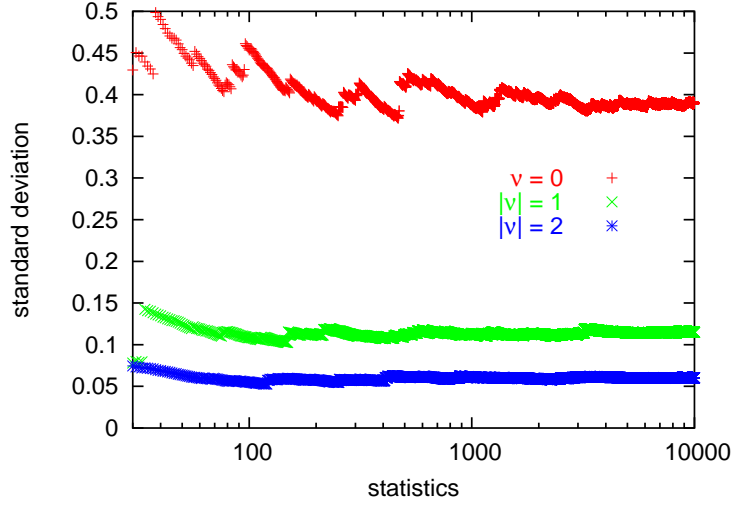
Figure 8.6: The standard deviation of $\Sigma_{\min}^{(\nu)}$ for topological sectors $|\nu| = 0$, 1 and 2 vs. pseudo statistics. The stabilization is observed much earlier for the topological sectors $|\nu| \neq 0$ than for $\nu = 0$.

to sample the Monte Carlo averages of observables of interest. In particular we consider the chiral condensate, which is related to the density of the lowest eigenvalues of the Dirac operator by the Banks-Casher relation (2.30). The starting point for us will be the spectral representation of the chiral condensate (2.32). If we consider the dependence of the chiral condensate on the mass of the valence quark, m_q, i.e. the quark which does not show up in the path integral average — then we can rewrite

$$\Sigma^{(\nu)}(m_q) = \int_0^\infty dz \, \frac{2 m_q \rho_s^{(\nu)}(z)/V}{m_q^2 + (z/(\Sigma V))^2} \, , \quad z = \lambda \Sigma V \, . \tag{8.1}$$

Now we take the first term in the expansion (2.100) and consider only the contribution of the lowest eigenvalue to the chiral condensate

$$\Sigma_{\min}^{(\nu)}(m_q) = \int_0^\infty dz \, \frac{2 m_q \rho_1^{(\nu)}(z)/V}{m_q^2 + (z/(\Sigma V))^2} \, . \tag{8.2}$$

We evaluate this integral by a Monte Carlo method, whereby we sample the integral at the values z distributed according to the χRMT predictions for $\rho_1^{(\nu)}(z)$ given in Eq. (2.101). The resulting value can be trusted only if the standard deviation stabilizes. In Figure 8.6 we show the simulation of the integral at quark mass $m_q = 21.3 \, \text{MeV}$ for various topological charges. In particular we show the standard deviation vs. the statistics. We find that one

needs $\mathcal{O}(10^4)$ configurations to sample $\Sigma_{\min}^{(0)}$, whereas this number reduces to $\mathcal{O}(10^2)$ for topological charges $|\nu| = 1$ and 2. Therefore it is advantageous to simulate in topological sectors $|\nu| > 0$.

As a possible remedy for the spikes there was proposed the low mode averaging method in Ref. [138].

8.3 Zero mode contributions to the pseudo-scalar correlator

In this Section we discuss the results for the zero mode contribution to the pseudo-scalar correlator. The necessary theoretical introduction, as well as the notation, were fixed in Subsection 2.3.4. The method employed here aims to consider only the zero mode contributions to the pseudo-scalar correlation function. The latter allows to compute the low energy constants as we saw in Subsection 2.3.4. Here we discuss the numerical evaluation.

We simulated quenched QCD on a $12^3 \times 24$ at $\beta = 5.85$ and on a $16^3 \times 32$ at $\beta = 6$ lattices with periodic boundary conditions with the Wilson gauge action and computed the lowest eigenmodes of the Neuberger operator. On the $12^3 \times 24$ lattice at $\beta = 5.85$ we also calculated the lowest eigenmodes of the overlap hypercube Dirac operator. Out of the eigenvectors we evaluated the zero mode contribution to the pseudo-scalar correlator according to formulae (2.65 – 2.67). We use the next–to–next–to–leading order expression (2.77) in the ϵ–regime to confront the time derivative of the zero mode contribution to the pseudo-scalar correlator with the corresponding quantity built up from the simulation data. This concept follows Ref. [1], which also presents the first numerical study.

We looked at topological sectors $|\nu| = 1$, 2 and 3 and we found that only the data from the topological sectors 1 and 2 can be used to obtain the low energy constants by fitting to the χPT predictions. Figures 8.7 and 8.9 show the simulation data for the connected contribution $\mathcal{C}_{|\nu|}/L^2$ and for the disconnected contribution $\widetilde{\mathcal{C}}_{|\nu|}/L^2$ computed with the Neuberger operator. For the disconnected part we show data only for topological sectors $|\nu| = 2$ and 3 since the data for the topological sector 1 are the same as for the connected contribution up to the negative sign. In Figures 8.8 we show the contribution of the zero modes calculated with the overlap hypercube fermions.

The time derivative of the zero mode contribution to the pseudo-scalar
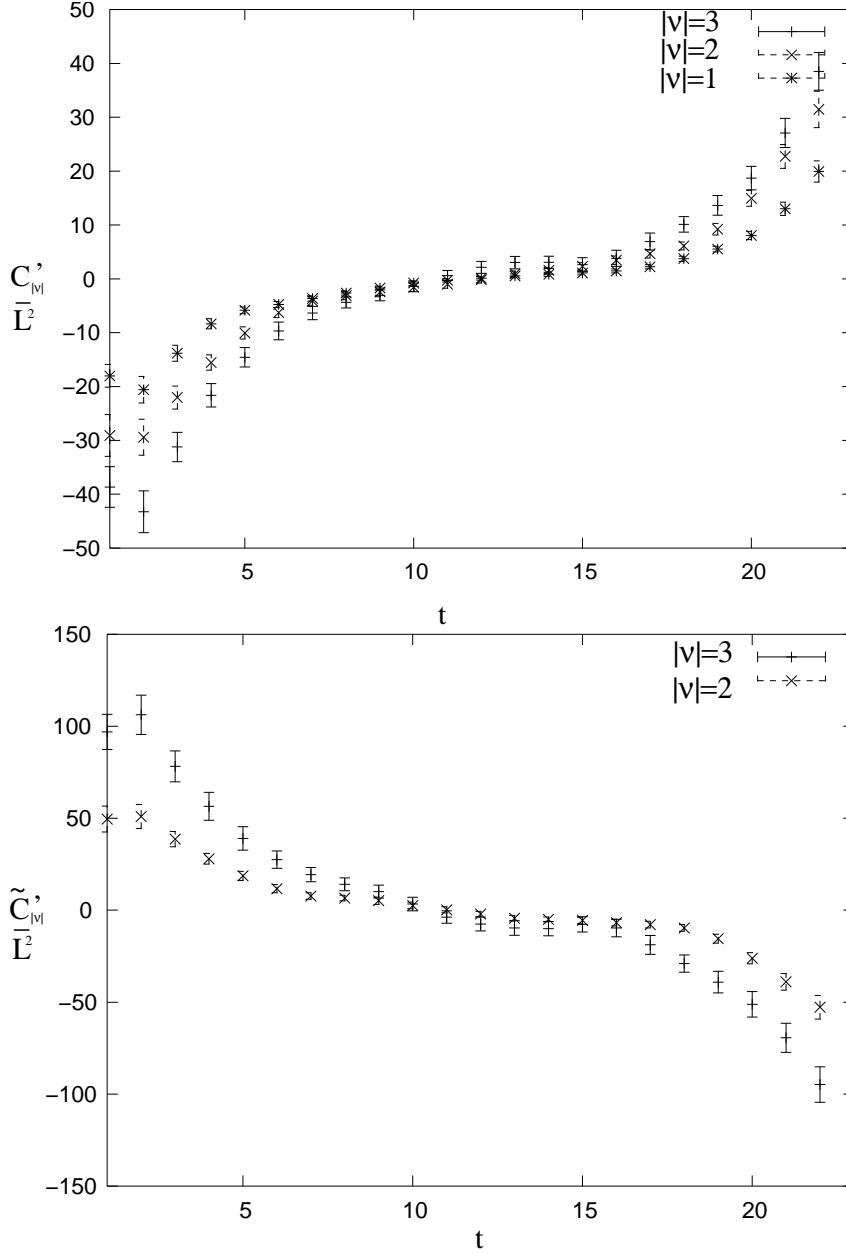
Figure 8.7: The plot on top shows the connected contributions of zero modes to the pseudo-scalar correlator for topological sectors $|\nu| = 1$, 2 and 3. The plot at the bottom represents the disconnected contributions to the pseudo-scalar correlator for topological sectors $|\nu| = 2$ and 3. We use the Neuberger operator on a lattice volume $V = 12^3 \times 24$, at $\beta = 5.85$.
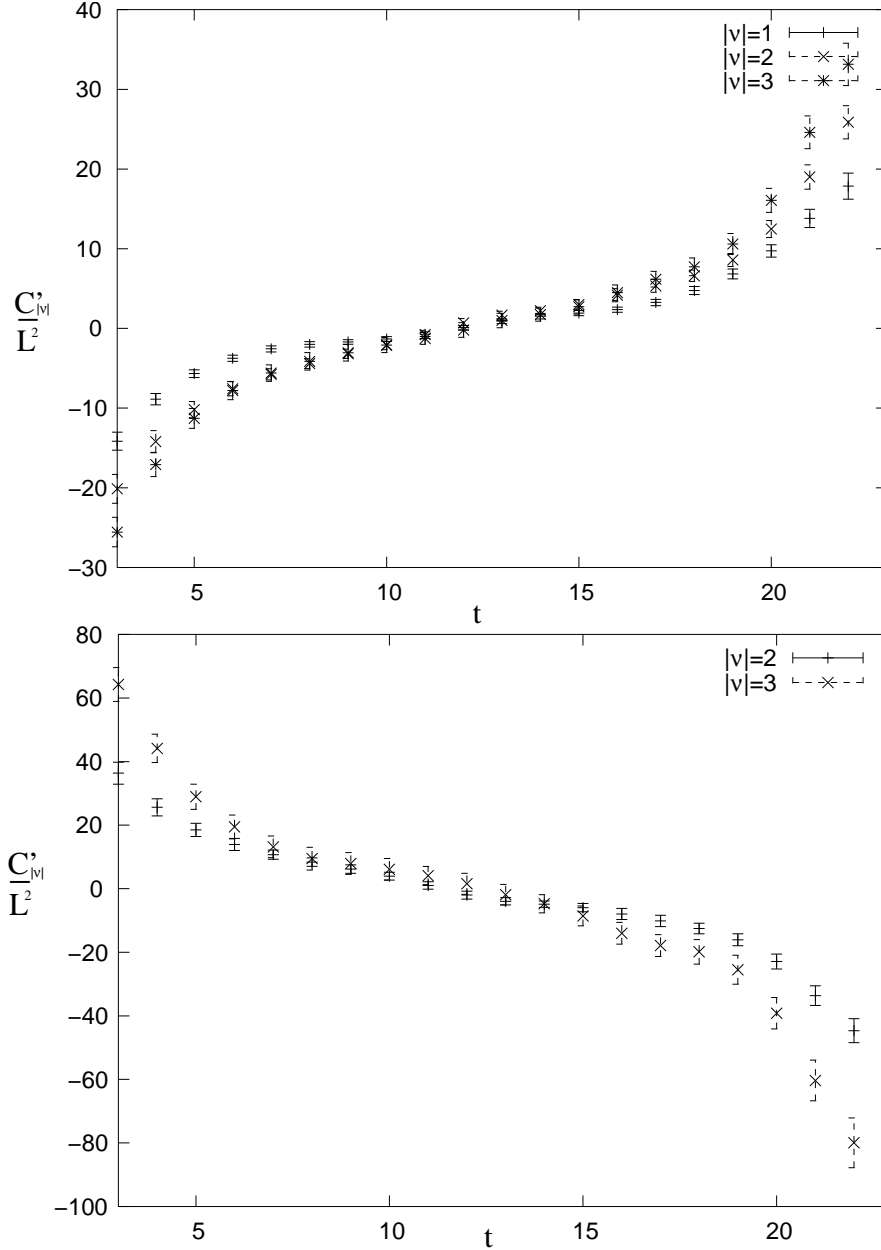
Figure 8.8: The plot on top shows the connected contributions of zero modes to the pseudo-scalar correlator for topological sectors $|\nu| = 1$, 2 and 3. The plot at the bottom represents the disconnected contributions to the pseudo-scalar correlator for topological sectors $|\nu| = 2$ and 3. We use the overlap hypercube operator on a lattice volume $V = 12^3 \times 24$, at $\beta = 5.85$.
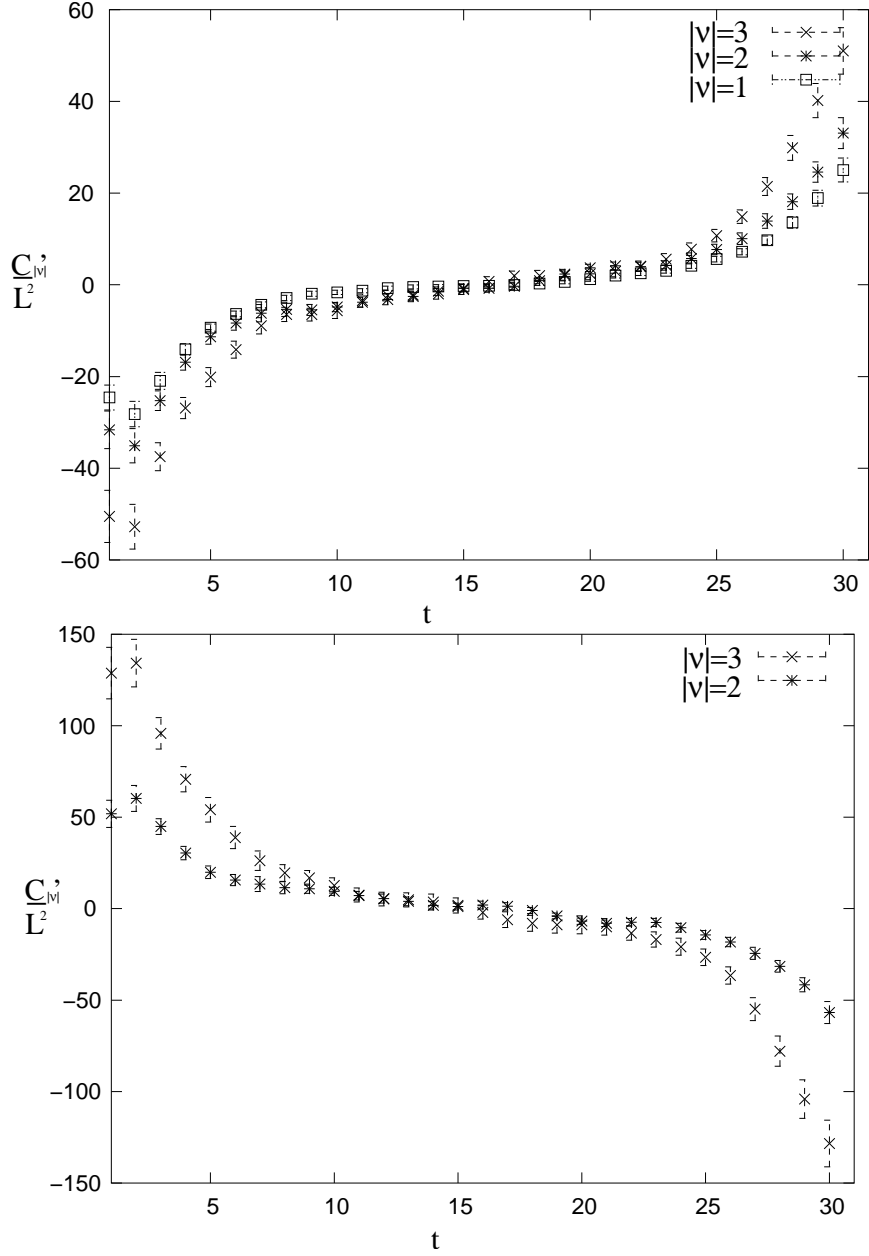
Figure 8.9: The plot on top shows the connected contributions of zero modes to the pseudo-scalar correlator for topological sectors $|\nu| = 1$, 2 and 3. The plot at the bottom represents the disconnected contributions to the pseudo-scalar correlator for topological sectors $|\nu| = 2$ and 3. We use the Neuberger operator on a lattice volume $V = 16^3 \times 32$, at $\beta = 6$.

94

correlator was approximated by the symmetric lattice derivative

$$\frac{df}{dt} \simeq \frac{f(t+1) - f(t-1)}{2} \ . \tag{8.3}$$

First we fitted the data using the general formula (2.66). Since that formula contains the parameters F_π, α and $\langle \nu^2 \rangle$ as unknown coefficients, we have to perform a 3–parameter fit. The shape coefficient β_1 for our anisotropic lattice volume was calculated according to the prescription in Ref. [20],

$$\beta_1 = 0.131465 \ .$$

The fit failed to produce reasonable estimates for the parameters. Therefore we followed the idea outlined in Ref. [1] and considered the expansion of the formula (2.66) in powers of $t/T - 0.5$,

$$\frac{1}{L^2} C'_{|\nu|}(t) = D_{|\nu|} \cdot (t/T - 0.5) + \mathcal{O}((t/T - 0.5)^3) \ ,$$

$$\frac{1}{L^2} \widetilde{C}'_{|\nu|}(t) = \widetilde{D}_{|\nu|} \cdot (t/T - 0.5) + \mathcal{O}((t/T - 0.5)^3) \ , \tag{8.4}$$

where the coefficients $D_{|\nu|}$ and $\widetilde{D}_{|\nu|}$ are given by

$$
\begin{aligned}
D_{|\nu|} &= \frac{2|\nu|}{(F_\pi L)^2} \Bigg\{ |\nu| + \frac{\alpha}{2N_c} - \frac{\beta_1}{F_\pi^2 \sqrt{V}} + \\
&\quad + \left[\left(\frac{7}{3} + 2\nu^2 - 2\langle \nu^2 \rangle \right) \zeta_2 + \frac{1}{2} \gamma_1 \right] \frac{T^2}{F_\pi^2 V} \Bigg\} \ , \\
\widetilde{D}_{|\nu|} &= -\frac{2|\nu|}{(F_\pi L)^2} \Bigg\{ 1 + |\nu| \left(\frac{\alpha}{2N_c} - \frac{\beta_1}{F_\pi^2 \sqrt{V}} \right) + \\
&\quad + |\nu| \left[\left(\frac{13}{3} - 2\langle \nu^2 \rangle \right) \zeta_2 + \frac{\gamma_1}{2} \right] \frac{T^2}{F_\pi^2 V} \Bigg\} \ .
\end{aligned}
\tag{8.5}
$$

Here

$$
\begin{aligned}
h'_2(\tau) &= \zeta_2(\tau - 0.5) + \mathcal{O}((\tau - 0.5)^3) \ , \\
h'_3(\tau) &= \gamma_1(\tau - 0.5) + \mathcal{O}((\tau - 0.5)^3) \ , \\
\zeta_2 &= -\frac{1}{24} \quad \text{and} \quad \gamma_1 = -\frac{1}{12} + \frac{1}{2} \sum_{\vec{n} \neq \vec{0}} \frac{1}{\sinh^2(T|\vec{p}|/2)} = -0.083291
\end{aligned}
\tag{8.6}
$$

with $|\vec{p}| = (2\pi/L)|\vec{n}|$, as in Eq. (2.78). The coefficients $D_{|\nu|}$ and $\widetilde{D}_{|\nu|}$ are arranged as sums of terms of the leading order $\mathcal{O}(\epsilon^4)$, next-to-leading order
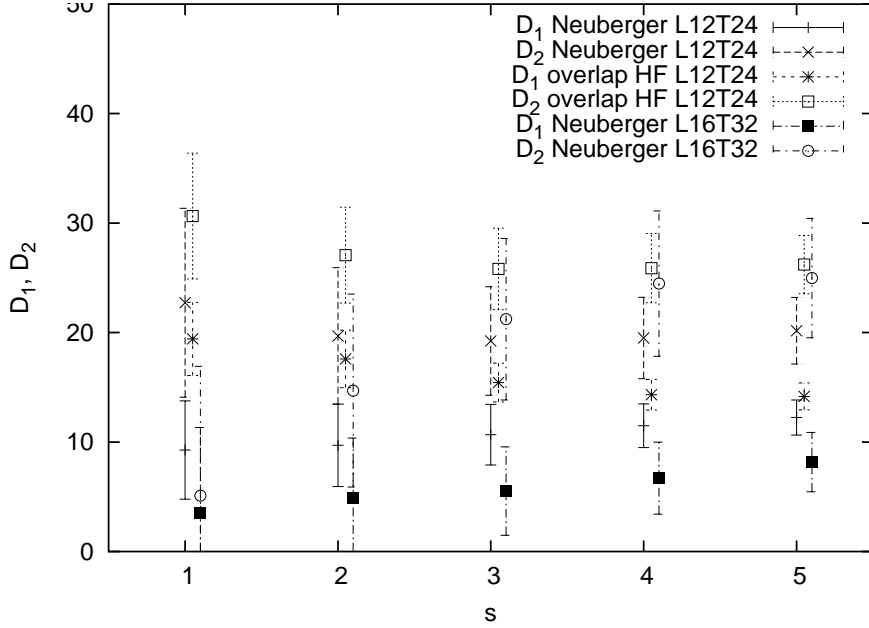
Figure 8.10: The slopes D_1 and D_2 vs. the fitting range $[T/2 - s, T/2 + s]$. We used the Neuberger operator on a $12^3 \times 24$ lattice, at $\beta = 5.85$ and on a $16^3 \times 32$ lattice, at $\beta = 6$ as well as the overlap hypercube Dirac operator on a $12^3 \times 24$ lattice, at $\beta = 5.85$

$\mathcal{O}(\epsilon^6)$ and next-to-next-to-leading order $\mathcal{O}(\epsilon^8)$, where $\epsilon = 1/(L\bar{F}_\pi)$ and $\bar{F}_\pi = F_\pi/\sqrt{3}$ was introduced in Eq. (2.70).

We employ these analytical predictions up to next–to–next–to–leading order to analyze our data. Applying one parameter fits of the data in topological sectors $|\nu| = 1$, 2 and 3 to the linear part of the formula (8.4), we extracted the slopes of $C'_{|\nu|}(t)/L^2$ from the data with jack-knife errors [139, 140]. The results for different fitting ranges are given in Tables 8.2, 8.3, 8.4 and in Figure 8.10.

First we see that the data for the topological charge $|\nu| = 3$ are statistically not very stable and thus we do not use it to extract physical information. Note that in the case of the overlap hypercube Dirac operator the data for the topological sector $|\nu| = 3$ tends to lie on the top of the data for $|\nu| = 2$. Therefore we concentrate on the slopes for topological charges $|\nu| = 1$ and 2.

Secondly, we observe in Figure 8.10 that the data stabilize on a fitting range $[T/2-s, T/2+s]$ starting from $s \geq 3$. Note that we used all data points within this interval. Since the term of $\mathcal{O}((\tau - 0.5)^3)$ in the expansion (8.4) is a NNLO term in the counting, it will be much more complicated to extract it. Therefore we consider only the linear term. Note that we neglect the

$\mathcal{O}((\tau-0.5)^3)$ term although we still allow the coefficients $D_{|\nu|}$ to be corrected by the NNLO terms in Eq. (8.5).

We now take the values for the topological susceptibility (resp. the expectation value of the topological charge squared, $\langle\nu^2\rangle$) from our simulations on the $12^3 \times 24$ lattice at $\beta = 5.85$ as an input for our method,

$$\begin{aligned}
\langle\nu^2\rangle &= 10.4 \pm 0.7 , \quad \text{for the overlap Wilson Dirac }, \\
\langle\nu^2\rangle &= 9.8 \pm 0.7 , \quad \text{for the overlap hypercube Dirac .} \quad (8.7)
\end{aligned}$$

Then we end up with a system of two equations

$$\begin{aligned}
D_1 &= D_1(F_\pi, \alpha, \langle\nu^2\rangle) , \\
D_2 &= D_2(F_\pi, \alpha, \langle\nu^2\rangle) . \quad (8.8)
\end{aligned}$$

Here the left hand side is the numbers extracted from Figure 8.10 at $s = 5$ given in Tables 8.2 - 8.4. We are aware that this choice is quite arbitrary but we have to postpone a more systematic analysis until larger statistics is available. Solving them we determine α and F_π. Unlike Ref. [1], where a three parameter fit to the linear part of the expressions (8.4) was used to extract the low energy constants, in this method we employ only the values of the slopes and their jack-knife errors to obtain the estimates on F_π and α. The corresponding error bars will follow as a result of the error propagation on the fitted values of $D_{|\nu|}$ and the error on the topological susceptibility, i.e.

$$\begin{aligned}
\delta F_\pi &= \sqrt{\sum_{i=1}^{2}\left(\frac{\partial F_\pi(D_1, D_2, \langle\nu^2\rangle)}{\partial D_i}\delta D_i\right)^2 + \left(\frac{\partial F_\pi(D_1, D_2, \langle\nu^2\rangle)}{\partial\langle\nu^2\rangle}\delta\langle\nu^2\rangle\right)^2} , \\
\delta\alpha &= \sqrt{\sum_{i=1}^{2}\left(\frac{\partial\alpha(D_1, D_2, \langle\nu^2\rangle)}{\partial D_i}\delta D_i\right)^2 + \left(\frac{\partial\alpha(D_1, D_2, \langle\nu^2\rangle)}{\partial\langle\nu^2\rangle}\delta\langle\nu^2\rangle\right)^2} \quad (8.9)
\end{aligned}$$

$F_\pi(D_1, D_2, \langle\nu^2\rangle)$ and $\alpha(D_1, D_2, \langle\nu^2\rangle)$ are implicitly determined by the system of Eqs. (8.8). We would like to note that the jack-knife error estimation would be quite difficult to apply for this method since the solutions to Eqs. (8.8) are not always real. Therefore one has to consider the resulting error bars with some caution.

The results of the solution of the Eqs. (8.8) are given in Table 8.5. The first line represents F_π and α extracted from our data with the Neuberger operator, the values for the second line are obtained using the overlap hypercube Dirac operator. The third line represents a three parameter fit to the data from Ref. [1] (Table 8.5) for the Neuberger operator on lattices which are there denoted as C_0 and C_1.

The results for the F_π and α are compatible for different overlap fermions within the error bars. At this stage we only conclude that the computation of α poses a challenge and further investigations are needed.

For completeness we show the statistics of our data together with the statistics for the C_0 lattice in Table 8.6.

Now we fix the value of $\langle \nu^2 \rangle = 10.4$ for the calculations with the overlap Wilson Dirac operator and $\langle \nu^2 \rangle = 9.8$ for the overlap hypercube Dirac operator. Then we perform a two parameter fit of the expression (8.4) to the combined data for two topological sectors $|\nu| = 1$ and 2 on different intervals $t \in [T/2 - s, T/2 + s]$. The results for F_π and α vs. the fitting range are collected in Figure 8.11. We see that the values of F_π and α stabilize at $s = 3$. The values of F_π and α for the Neuberger operator are consistently larger at finer lattice spacing. F_π is still subject to renormalization which can increase it substantially. The value of α seems to scale within 2σ. We also see that the results for the Neuberger operator are compatible with those of the overlap hypercube operator. Note, however, that the data for the overlap hypercube operator tend to be less noisy than for the Neuberger operator on the lattice $12^3 \times 24$, at $\beta = 5.85$.

The estimates and the jack-knife error bars of F_π and α, as well for the re-calculated $D_{|\nu|}$, for the fitting range $[T/2 - 5, T/2 + 5]$ are collected in Table 8.7. First of all we can confirm again that the given statistics is not sufficient to obtain a stable value of the slope D_3 at least on $12^3 \times 24$ lattice at $\beta = 5.85$. Next we see that the two methods that we discussed lead to compatible results. However the two parameter fit produces significantly more reliable error bars. Note that if we change the topological susceptibility in our two parameter fit by 10% this will lead only to a $\mathcal{O}(10\%)$ change in α while F_π remains almost the same. We conclude that performing the two parameter fit is still the best method to obtain the estimates for F_π and α with a control over the errors. We argue that the calculation of the mere zero mode contribution is potentially capable of the extraction of F_π, α and topological susceptibility χ_t once a good statistics is available. Its obvious virtue is that it is not affected by the problems of small quark masses and small eigenvalues of the Dirac operator which magnify the noise of the propagator as we discussed in Section 8.2.
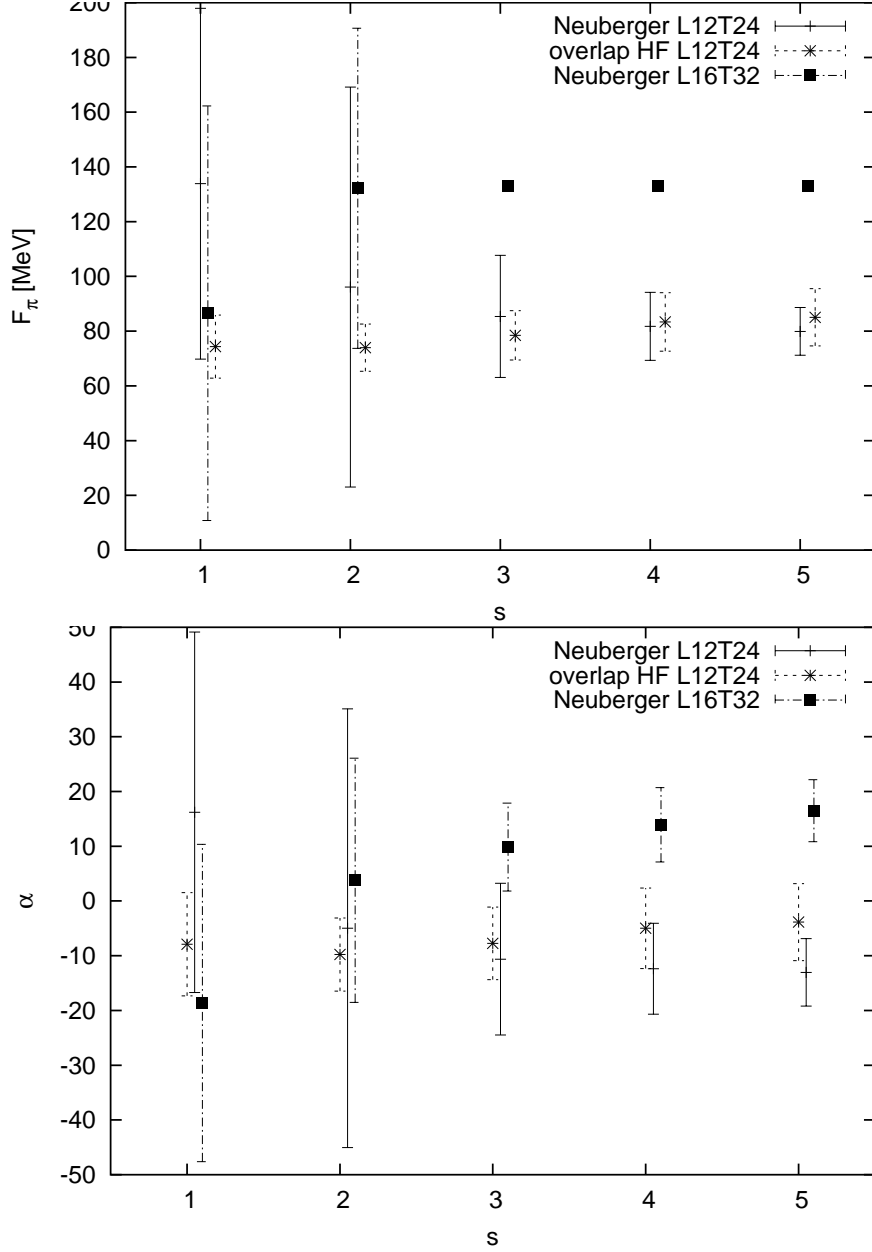
Figure 8.11: F_π and α extracted from a two parameter fit to the combined data from topological sectors $|\nu| = 1$ and 2 vs. the fitting range $[T/2 - s, T/2 + s]$. We used the Neuberger operator on a $12^3 \times 24$ lattice at $\beta = 5.85$ and on a $16^3 \times 32$ lattice at $\beta = 6$, as well as the overlap hypercube Dirac operator on a $12^3 \times 24$ lattice, at $\beta = 5.85$.

lattice size	β	μ	physical volume	number of configurations		
				$\nu = 0$	$|\nu| = 1$	$|\nu| = 2$
12^4	6	1.4	$(1.12\,\text{fm})^4$	47	78	24
$10^3 \times 24$	6	1.4	$(0.93\,\text{fm})^3 \times 1.86\,\text{fm}$	20	24	17

Table 8.1: The statistics of our simulations on two lattice sizes.

fitting range	$D_{|\nu|}$			$\chi^2/d.o.f.$	$\chi^2/d.o.f.$	$\chi^2/d.o.f.$
	$|\nu| = 1$	$|\nu| = 2$	$|\nu| = 3$			
$[11, 13]$	9.2 ± 4.5	22.7 ± 8.6	20.3 ± 12.7	0.2	0.05	4.9
$[10, 14]$	9.7 ± 3.8	19.7 ± 6.2	24.3 ± 9.9	0.1	0.05	2.8
$[7, 17]$	12.2 ± 1.6	20.2 ± 3.0	$27.0 + \pm 5.0$	1.3	0.1	1.3

Table 8.2: The slopes $D_{|\nu|}$ vs. the fitting range computed with the overlap Wilson Dirac operator at $\beta = 5.85$ on $12^3 \times 24$ lattice.

fitting range	$D_{|\nu|}$			$\chi^2/d.o.f.$	$\chi^2/d.o.f.$	$\chi^2/d.o.f.$
	$|\nu| = 1$	$|\nu| = 2$	$|\nu| = 3$			
$[11, 13]$	19.4 ± 3.3	30.6 ± 5.7	27.7 ± 11.4	0.16	1.6	0.05
$[10, 14]$	17.6 ± 2.6	27.1 ± 4.4	23.7 ± 8.9	0.17	0.86	0.07
$[7, 17]$	14.2 ± 1.2	26.2 ± 2.7	26.2 ± 4.5	0.6	0.4	0.15

Table 8.3: The slopes $D_{|\nu|}$ vs. the fitting range computed with the overlap hypercube Dirac operator at $\beta = 5.85$ on $12^3 \times 24$ lattice.

fitting range	$D_{|\nu|}$			$\chi^2/d.o.f.$	$\chi^2/d.o.f.$	$\chi^2/d.o.f.$
	$|\nu| = 1$	$|\nu| = 2$	$|\nu| = 3$			
$[15, 17]$	3.5 ± 7.8	5.1 ± 11.8	48.1 ± 14.5	0.21	0.87	0.47
$[14, 18]$	4.9 ± 5.4	14.7 ± 8.8	35.4 ± 12.9	0.12	0.58	0.32
$[11, 21]$	8.2 ± 2.7	25.0 ± 5.5	22.0 ± 7.4	0.44	0.47	0.3

Table 8.4: The slopes $D_{|\nu|}$ vs. the fitting range computed with the overlap Wilson Dirac operator at $\beta = 6$ on $16^3 \times 32$ lattice.

β	V	D_1	D_2	F_π [MeV]	α	remarks
5.85	$12^3 \times 24$	13.5 ± 1.4	21.8 ± 2.6	80.7 ± 9.1	-12.6 ± 6.6	Neuberger
5.85	$12^3 \times 24$	14.2 ± 1.2	26.2 ± 2.7	85.7 ± 11	-6.2 ± 8.2	overlap HF
6	20^4	3.9 ± 0.5	9.4 ± 0.7			C_1
5.8784	16^4	3.4 ± 0.3	8.9 ± 0.5	$(80.8, 107.4)$	$(-1.8, 7.8)$	C_0

Table 8.5: The first two lines show F_π and α as a solution of the Eq. (8.5), extracted from our data. The third line gives for comparison the values quoted in Ref. [1].

operator kernel	lattice size	β	physical volume	number of configurations		
				$|\nu| = 1$	$|\nu| = 2$	$|\nu| = 3$
Wilson	$12^3 \times 24$	5.85	$(1.48\,\text{fm})^3 \times 2.96\,\text{fm}$	90	72	64
Wilson	$16^3 \times 32$	6	$(1.49\,\text{fm})^3 \times 2.98\,\text{fm}$	92	70	71
hypercube	$12^3 \times 24$	5.85	$(1.48\,\text{fm})^3 \times 2.96\,\text{fm}$	91	83	69
Wilson	16^4	5.8784	$(1.86\,\text{fm})^4$	229	186	–

Table 8.6: The statistics for our data (1st, 2nd and 3rd lines) and for the C_0 lattice in Ref. [1] (fourth line).

D_1	D_2	D_3	F_π	α	$\chi^2/\text{d.o.f.}$
12.4 ± 1.6	20.2 ± 3.1	7.4 ± 17	$79.9 \pm 8.7\,\text{MeV}$	-13.0 ± 6.1	0.7
14.3 ± 1.3	26.2 ± 2.7	23.3 ± 15	$85.1 \pm 10.5\,\text{MeV}$	-3.9 ± 7.0	0.5
9.9 ± 1.9	21.8 ± 3.8	33.7 ± 5.7	$132.9 \pm 0.0\,\text{MeV}$	16.5 ± 5.7	0.6

Table 8.7:   Results of the two parameter fit in the range $[T/2 - 5, T/2 + 5]$ for the combined data in topological sectors $|\nu| = 1$ and 2. The first line represents the results for the overlap Wilson Dirac operator and the second line represents the results for overlap hypercube Dirac operator on a lattice of size $12^3 \times 24$, at $\beta = 5.85$. The third line represents the results for the overlap Wilson Dirac operator on a lattice of size $16^3 \times 32$, at $\beta = 6$.

Chapter 9

Topology conserving Lüscher gauge action

9.1 Motivation

We employ the overlap operator as a regularization for the fermion fields. It obeys the Ginsparg-Wilson relation (2.122) and thus the chiral symmetry is preserved at a finite lattice spacing as discussed in Ref. [69] and we demonstrated in Section 2.5.3. This enables us to perform simulations at small quark masses and to define the topological charge as the index of the overlap operator. In particular it is applied to explore the ϵ–regime. In the previous Chapter we saw that in order to perform the precision calculation of the low energy constants in the ϵ–regime one has to collect as much statistics as possible for a given topological sector. A computer time consuming part of these calculations is that for each configuration one needs to compute the index of the overlap operator. In particular we saw that the simulations in the topological sector $\nu = 0$, which occurs quite often in the simulations, are plagued by the large statistical fluctuations and therefore it is favorable to evaluate observables in the sectors of $|\nu| \neq 0$. As we learned from the χRMT study of the probability distributions of the individual eigenvalues, the topological sectors $|\nu| = 1$ and 2 are of primary interest for the simulations in moderate physical volumes. In simulations on a large lattices the charges fluctuate between $\nu = -10$ and 10, see Figure 7.1. Therefore it would be highly profitable for the simulations if a method was found to sample the statistics within a certain topological sector without recomputing the index. In other words, one seeks a method which provides a large autocorrelation time for the topological charge and still small autocorrelation times for the observables of interest.

The change of the topological sector for the overlap Dirac operator implies that an eigenvalue flips from the origin of the Ginsparg-Wilson circle to $2\mu/a$, i.e. to the cut-off scale, or vice versa as the gauge field is deformed. If the corresponding deformation is done continuously then the inverse square root of $A^\dagger A$ will develop a singularity. As it was already mentioned it is guaranteed under the condition (3.19) that $A^\dagger A$ remains positive. It was shown later by H. Neuberger [141] that this condition can be relaxed to

$$\epsilon \leq \frac{1}{(1 + \frac{1}{\sqrt{2}})d(d-1)} \simeq \frac{1}{20.5} \ . \tag{9.1}$$

If it is fulfilled then the topological charge is guaranteed not to change under a continuous deformation of the gauge field. A non-continuous deformation can, however, still change it but the hope is that the probability of such a change is small in simulations. Applying the weak coupling expansion for the Wilson gauge action we found that the above relation is satisfied for the mean plaquette value at $\beta \sim 40$. Obviously simulations are not possible with such a large value of β due to the strong autocorrelations and tiny lattice spacings. However one hopes that the topological charge will be still conserved over a large number of configurations even if the gauge action only favors the plaquettes obeying the further relaxed condition (9.1).

It is possible to introduce a lattice gauge action which will suppress large values of $S_P(U_P) = 1 - (1/3)\mathrm{Re\,Tr}\,U_P$ and thereby the condition (3.18) will be fulfilled. This will in turn lead to conservation of the topological charge along the simulation trajectory. To this end we define

$$S_P(U^{(P)}_{x,\mu\nu}) \rightarrow S_\alpha(U^{(P)}_{x,\mu\nu}) = \begin{cases} \frac{S_P(U^{(P)}_{x,\mu\nu})}{(1-S_P(U^{(P)}_{x,\mu\nu})/\epsilon)^\alpha} & S_P(U^{(P)}_{x,\mu\nu}) < \epsilon \\ \infty & S_P(U^{(P)}_{x,\mu\nu}) \geq \epsilon \end{cases} \ , \tag{9.2}$$

where $\alpha > 0$. In particular, $\alpha = 1$ was used by M. Lüscher [142, 143] for conceptual purposes and was also applied in Ref. [144] to the Schwinger model. In the latter the authors used $\epsilon = 1$ as opposed to the strict theoretical bound of $1/5$ for two dimensions, in order to let the gauge fields fluctuate more while still suppressing topological transitions. This was sufficient to stabilize the topological history over hundreds of configurations. A potential problem for the simulations with this action can be that due to the stringent constraint the resulting lattice spacing may become too small. This would require very large lattice volumes to obtain a reasonable physical volume for simulations. Yet another caveat was raised by M. Creutz that such an action may lead to a non-positive transfer matrix which will make the transition to Minkowski space at finite lattice spacing impossible [145]. However, one can think of first taking the continuum limit and then going to Minkowski space.

9.2 Results on the topological histories

We used the local Hybrid Monte Carlo (HMC) algorithm — for a description we refer to Appendix A — to simulate the action (9.2) with $\alpha = 1$ in quenched QCD. The standard tools like heat bath and overrelaxation are not applicable in this case since they very much rely on the properties of the gauge action (3.2) which do not hold for the action (9.2). For HMC one has to compute the "force" $F_{x,\alpha}$,

$$
\begin{aligned}
F_{x,\mu,\alpha} &= \frac{\delta S_\alpha(U_{x,\mu\nu}^{(P)})}{\delta U_{x,\mu}} = F_{x,\mu,\alpha}^{\text{Wilson}} \frac{1 + \frac{\alpha-1}{\epsilon} S_P}{(1 - S_P/\epsilon)^{\alpha+1}} \ , \\
F_{x,\mu,\alpha}^{\text{Wilson}} &= \frac{\delta S_P(U_{x,\mu\nu}^{(P)})}{\delta U_{x,\mu}} \ .
\end{aligned}
\tag{9.3}
$$

Figure 9.1 shows the dependence of S_α/S_P vs. S_P as well as F_α/F_P vs. S_P. As α decreases the "force" becomes more flat in the domain of S_P close to the free field.

If the new action is defined with quite a stringent constraint this will reduce the freedom for the gauge field to fluctuate which could imply a very small lattice spacing as we mentioned before. To investigate this we start off by searching a set of values of $\{\epsilon, \beta\}$ which will provide the same $\langle S_P \rangle$ in simulations on 4^4 lattice. The obtained curve of the "constant physics" was used as a guideline for the further analysis where we computed r_0 for the specific values of ϵ, β on the curve. The results for the curve of the "constant physics" are reported in Figure 9.2. As ϵ decreases the value of β must be also decreased in order to obtain the same expectation value for the plaquette $\langle S_P \rangle$. Another problem is the rejection of a link variable due to the violation of the boundary in definition of the action (9.2). It turned out that the rejection rate is increased as β is decreased, see Table 9.1 [146].

Next we picked out a few points from the curve and computed r_0 on a 16^4 lattice. The results for r_0 are given in Table 9.1. We see that r_0 slightly increases as β is decreased. As a pilot test for the topological stability we employed the *cooling method* [147]. This is a relatively fast way compared to the overlap index to estimate the topological charge of a gauge configuration at moderate β. In this approach one deforms a gauge configuration by minimizing its gauge action locally to reach the approximate solutions of the lattice Yang-Mills equations of motion, which are the Euler equations for the Wilson Yang-Mills gauge action. The resulting gauge configurations, which are picked out from the first stable plateau, dissociate in objects with topological charges $\nu = \pm 1$. They can be interpreted as instantons and anti-instantons. Since the cooled configurations are smooth, these charges

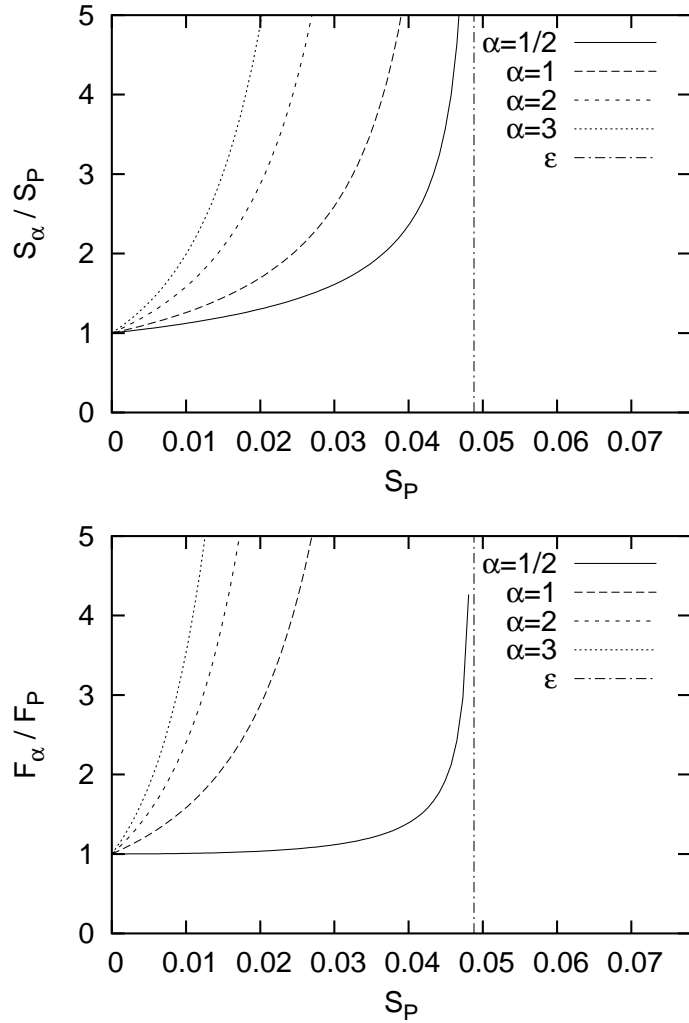Figure 9.1: The plot on top shows the dependence of S_α/S_P vs. S_P. The plot at the bottom shows the dependence of the "force" F_α/F_P vs. S_P. The theoretical bound is shown as an asymptotic vertical line at $S_P = 1/\epsilon$.
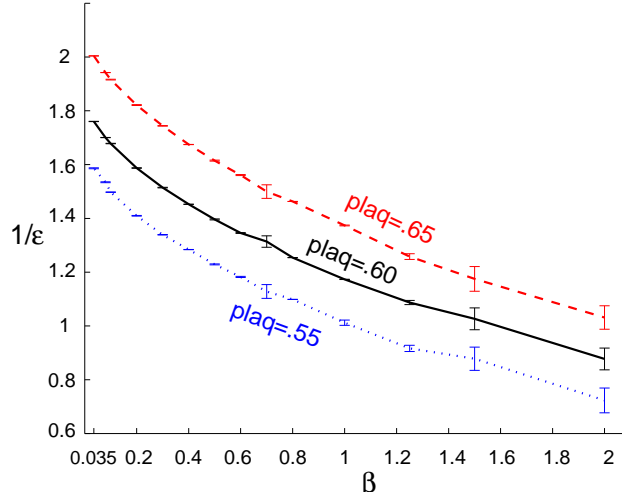
Figure 9.2: The lines of constant expectation value of the plaquette, $\langle S_P \rangle$, in the plane spanned by the action parameters $1/\epsilon$ and β.

can be determined using a simple lattice discretization of the continuum formula (2.8) given for instance in Ref. [148]. Hence the topological charge of a cooled gauge configuration can be determined by the difference of number of instantons N_+ and anti-instantons N_-. To quantify the topological charge conservation we computed the autocorrelation time of $Q_{\text{cool}} = N_+ - N_-$. The main conjecture is that the autocorrelation time of this quantity is a good estimate for the autocorrelation time of the topological charge given by the index of the overlap operator for the equilibrium configurations. The latter is supported by the fact that the corresponding equilibrium configurations are quite smooth ($\beta_W \simeq 6.19$). Hence the definition of the index given by cooling matches the definition of the index given by the overlap operator at least up to 80% [149]. This is verified by our study at stronger coupling $\beta = 6$, shown in Figure 9.3. It shows the distribution of the difference of the topological charge defined with cooling and the topological charge defined by the Neuberger index.

In Figures 9.4 we show the histories of Q_{cool} for the parameters β and ϵ given in Table 9.1.

The autocorrelation times for the quantity Q_{cool}, $\tau_{\text{aut}}^{\text{cool}}$, as well as for the plaquette S_P, $\tau_{\text{aut}}^{\text{plaq}}$, are given in Table 9.1. We see that $\tau_{\text{aut}}^{\text{cool}}$ becomes larger as ϵ is decreased, while the autocorrelation times for the plaquette become even smaller. This gives confidence that the pair $1/\epsilon = 1.52$ and $\beta = 0.3$ constitutes a good parameter set for the action to conduct simulations in the ϵ-regime.
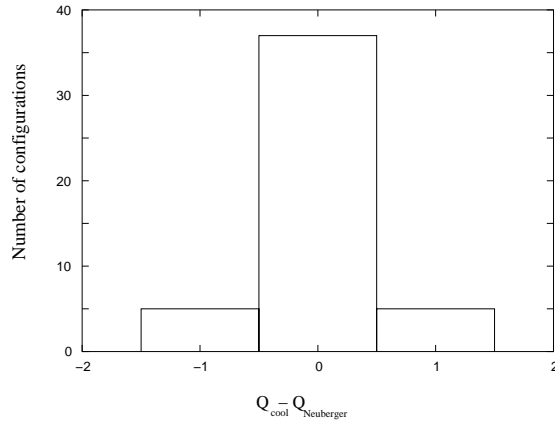
Figure 9.3: The histogram of the difference between topological charge defined by the cooling, Q_{cool}, and the topological charge defined by the index of the Neuberger operator, $Q_{\text{Neuberger}}$. For our parameters $V = 10^3 \times 24$, $\beta = 6$ we observe 80 % agreement.

$1/\epsilon$	β	rejection rate	r_0/a	β_W	$\tau_{\text{aut}}^{\text{cool}}$	$\tau_{\text{aut}}^{\text{plaq}}$
0	6.19	0	7.25	6.19	3.94	7.27
1.25	0.8	$< 0.1\%$	7.0(1)	6.17	5.07	1.15
1.52	0.3	5%	7.3(4)	6.19	21.03	0.85

Table 9.1: Results for the parameter r_0/a computed in simulations on 16^4 lattice for various values of ϵ and β. We give the corresponding value of β for the Wilson action, which we denote as β_W. The autocorrelation times for Q_{cool} and for the plaquette are reported. We also show the the rejection rate for the links.
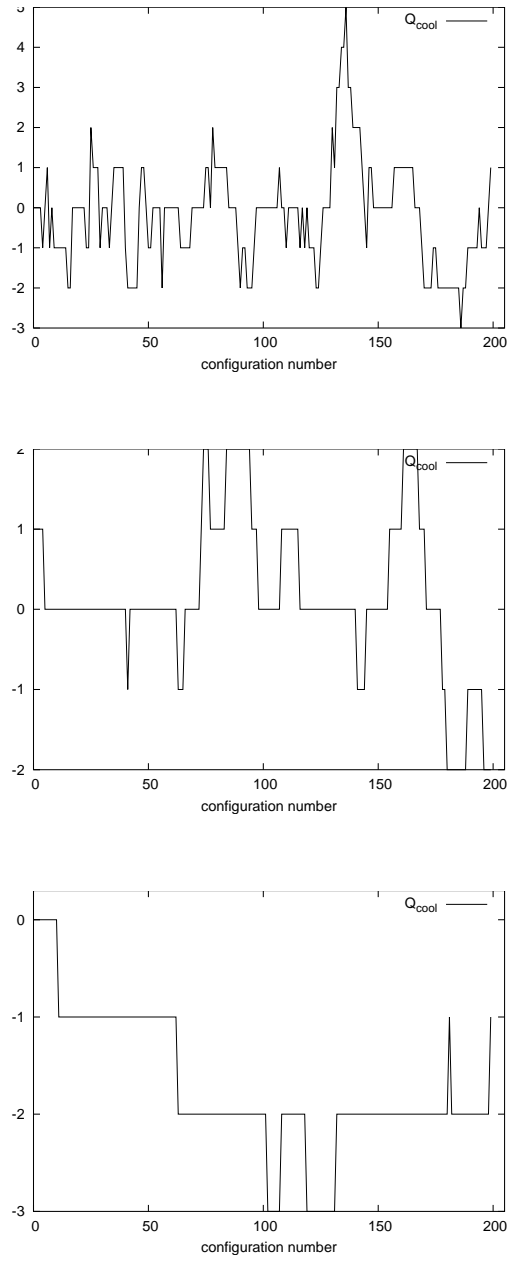
Figure 9.4: Histories of Q_{cool} at $\{\beta, 1/\epsilon\} = \{6.19, 0\}$, $\{0.8, 1.25\}$, $\{0.3, 1.52\}$ for the plot on top, in the middle and at the bottom, respectively.

Chapter 10

Conclusions

In this thesis we presented a study of the feasibility to extract physical information in the ϵ–regime using various formulations of chiral lattice fermions. In this final Section we briefly summarize the main results.

The investigations were done in the framework of quenched lattice QCD. To discretize the fermion fields we chose the Ginsparg-Wilson fermions. In particular we applied the Neuberger operator and the overlap hypercube operator. These formulations provide a regularization scheme which preserves the chiral symmetry at a finite lattice spacing. As a consequence the topological charge is well defined by the index of the overlap Dirac operator. Therefore by simulating quenched QCD in the ϵ–regime one can reach the domain of very small quark masses. The computations are, however, quite tedious and therefore at present only the quenched approximation can be studied. Controlling the finite size effects in QCD simulations in the ϵ–regime one can obtain the low energy constants of the chiral Lagrangian, which are also those of the infinite volume up to quenching effects.

One of the main topics of these investigations was the analysis of the probability distributions of the individual eigenvalues of the Dirac operator in the QCD simulations in the ϵ–regime. We confronted the simulation data with the analytical prediction conjectured in the framework of the χRMT. The conjecture is that the χRMT is a theory which can describe eigenvalue densities in the ϵ–regime. It is mainly based on the fact that in the limit of large matrices the χRMT partition function coincides with the χPT partition function to the leading order in the ϵ–regime. Also some quantities like the microscopic spectral density were calculated for the special cases both, in χRMT and in χPT, leading to the same expressions. The ability of χRMT to explain the simulations in the ϵ–regime being yet a conjecture received a convincing support in our investigations. To this end we found that the behavior of the probability distributions of the individual eigenvalues can be

reliably described by the χRMT if the box length of the physical volume exceeds about $L \geq 1.12\,\mathrm{fm}$. The chiral condensate enters as the only parameter for the probability distributions of the individual eigenvalues. Therefore it can be obtained by fitting the χRMT curves to the simulation data.

A next result obtained from this study was the determination of the lower bound for the size of the physical volume where the data can be described by χPT. It has proven to help in understanding the behavior of the two-point mesonic functions. In particular we could explain why the correlators calculated in quenched simulations on $(0.93\,\mathrm{fm})^3 \times 1.86\,\mathrm{fm}$ are not modeled by the χPT. It turned out that the size of the physical volume of $L \approx 0.93\,\mathrm{fm}$ is too small for the simulations in the ϵ–regime and a size of $L \approx 1.12\,\mathrm{fm}$ lies on the threshold. When trying to extract the low energy constants F_π and Σ from the axial-vector two-point function we found that F_π, which enters the formula in an additive constant, can be obtained by fitting. The chiral condensate Σ, on the contrary, enters in a way that leaves the analytic formula almost insensitive to drastic changes in Σ for the topological sectors $|\nu| > 0$. The sensitivity is restored only for $\nu = 0$. This makes it prohibitively difficult to extract Σ using the axial-vector two-point function at $|\nu| \neq 0$. On the other hand, the signal for the axial-vector correlator in the topological sector $\nu = 0$ turned out to be very noisy. This we attributed to a high probability of occurrence of near-zero modes. The latter was also supported by our χRMT study of the eigenvalues.

To estimate the statistics needed for the topological sectors $|\nu| = 0$, 1 and 2 we considered the contribution to the chiral condensate given by the distribution of the lowest eigenvalue of the Dirac operator $\Sigma_{\mathrm{min}}^{(\nu)}$. Then we simulated fake eigenvalues with these distributions and obtained the necessary statistics to stabilize the standard deviation of the $\Sigma_{\mathrm{min}}^{(\nu)}$. It turned out that one needs a tremendous statistics of $\mathcal{O}(10^4)$ configurations in the topological sector $\nu = 0$ (for this stabilization). For higher topological sectors ($|\nu| = 1, 2$) this number is decreased to $\mathcal{O}(10^2)$ configurations.

As an alternative method to calculate the low energy constants one can consider only the contribution of the zero modes to the mesonic two-point functions. We computed such contributions to the pseudo-scalar two-point function. The analytical expressions for them are known and we fitted them to our data to explore the possibility of extracting the parameters F_π and α — yet another low energy parameter appearing in the chiral quenched Lagrangian. We were able to obtain reasonable bounds on these values with our statistics. Therefore we conclude that this is a promising method to compute the low energy constants.

Next we considered the topological susceptibility. This quantity was computed using two formulations of the overlap operator: the Neuberger fermions

(with the usual Wilson action as its kernel) and the hypercube fermions (with the truncated fixed point action as its kernel). The overlap hypercube operator is expected to be superior to the conventional formulation. It turned out that the locality is improved and the topological susceptibility comes closer to the continuum value at the same lattice spacing.

As a theoretical development of the simulations in the ϵ–regime one can think of a method to simulate a set of configurations belonging to a certain topological charge without recomputing the index. The problem can be re-formulated as to simulate configurations with the topological charge being strongly autocorrelated while other observables of interest remaining decor-related. This we studied using a gauge action proposed by M. Lüscher. We are confident that we found a good set of parameters for the Lüscher gauge action to meet these requirements.

Bibliography

[1] L. Giusti, P. Hernández, M. Laine, P. Weisz, and H. Wittig. Low-energy couplings of qcd from topological zero-mode wave functions. *JHEP*, 01:003, 2004.

[2] K. Osterwalder and R. Schrader. Axioms for euclidean green's functions. *Commun. Math. Phys.*, 31:83, 1973.

[3] K. Osterwalder and R. Schrader. Axioms for euclidean green's functions. 2. *Commun. Math. Phys.*, 42:281, 1975.

[4] L. B. Okun. *Leptons and quarks*. Nauka, Moscow, 1981.

[5] I. Montvay and G. Münster. *Quantum Fields on a Lattice*. Cambridge University Press, Cambridge, U.K., 1994.

[6] M. F. Atiyah and I. M. Singer. The index of elliptic operators. 1. *Annals Math.*, 87:484, 1968.

[7] Y. Nambu. Axial vector current conservation in weak interactions. *Phys. Rev. Lett.*, 4:380, 1960.

[8] J. Goldstone. Field theories with 'superconductor' solutions. *Nuovo Cim.*, 19:154, 1961.

[9] G. 't Hooft. Symmetry breaking through bell-jackiw anomalies. *Phys. Rev. Lett.*, 37:8, 1976.

[10] G. 't Hooft. Computation of the quantum effects due to a four- dimensional pseudoparticle. *Phys. Rev.*, D14:3432, 1976.

[11] T. Banks and A. Casher. Chiral symmetry breaking in confining theories. *Nucl. Phys.*, B169:103, 1980.

[12] S. R. Coleman, J. Wess, and B. Zumino. Structure of phenomenological lagrangians. 1. *Phys. Rev.*, 177:2239, 1969.

[13] C. G. Callan, S. R. Coleman, J. Wess, and B. Zumino. Structure of phenomenological lagrangians. 2. *Phys. Rev.*, 177:2247, 1969.

[14] S. Weinberg. Phenomenological lagrangians. *Physica*, A96:327, 1979.

[15] J. Gasser and H. Leutwyler. Chiral perturbation theory to one loop. *Ann. Phys.*, 158:142, 1984.

[16] J. Gasser and H. Leutwyler. Chiral perturbation theory: expansions in the mass of the strange quark. *Nucl. Phys.*, B250:465, 1985.

[17] J. Gasser and H. Leutwyler. Thermodynamics of chiral symmetry. *Phys. Lett.*, B188:477, 1987.

[18] H. Neuberger. A better way to measure f_π in the linear σ model. *Phys. Rev. Lett.*, 60:889, 1988.

[19] H. Neuberger. Soft pions in large boxes. *Nucl. Phys.*, B300:180, 1988.

[20] P. Hasenfratz and H. Leutwyler. Goldstone boson related finite size effects in field theory and critical phenomena with $o(n)$ symmetry. *Nucl. Phys.*, B343:241, 1990.

[21] F. C. Hansen. Finite size effects in spontaneously broken $su(n) \times su(n)$ theories. *Nucl. Phys.*, B345:685, 1990.

[22] F. C. Hansen and H. Leutwyler. Charge correlations and topological susceptibility in qcd. *Nucl. Phys.*, B350:201, 1991.

[23] W. Bietenholz. Goldstone bosons in a finite volume: The partition function to three loops. *Helv. Phys. Acta*, 66:633, 1993.

[24] H. Leutwyler and A. Smilga. Spectrum of dirac operator and role of winding number in qcd. *Phys. Rev.*, D46:5607, 1992.

[25] T. Yoshié. Light hadron spectroscopy. *Nucl. Phys. Proc. Suppl.*, 63:3, 1998.

[26] S. Aoki and et. al. Quenched light hadron spectrum. *Phys. Rev. Lett.*, 84:238, 2000.

[27] C. W. Bernard and M. F. L. Golterman. Chiral perturbation theory for the quenched approximation of qcd. *Phys. Rev.*, D46:853, 1992.

[28] P. H. Damgaard and K. Splittorff. Partially quenched chiral perturbation theory and the replica method. *Phys. Rev.*, D62:054509, 2000.

[29] P. H. Damgaard, P. Hernández, K. Jansen, M. Laine, and L. Lellouch. Finite-size scaling of vector and axial current correlators. *Nucl. Phys.*, B656:226, 2003.

[30] P. H. Damgaard, M. C. Diamantini, P. Hernández, and K. Jansen. Finite-size scaling of meson propagators. *Nucl. Phys.*, B629:445, 2002.

[31] P. H. Damgaard and S. M. Nishigaki. Universal spectral correlators and massive dirac operators. *Nucl. Phys.*, B518:495, 1998.

[32] P. H. Damgaard and S. M. Nishigaki. Distribution of the k-th smallest dirac operator eigenvalue. *Phys. Rev.*, D63:045012, 2001.

[33] T. Wilke, T. Guhr, and T. Wettig. The microscopic spectrum of the QCD dirac operator with finite quark masses. *Phys. Rev.*, D57:6486, 1998.

[34] S. M. Nishigaki, P. H. Damgaard, and T. Wettig. Smallest dirac eigenvalue distribution from random matrix theory. *Phys. Rev.*, D58:087704, 1998.

[35] D. Diakonov and V. Yu. Petrov. Quark propagator and chiral condensate in an instanton vacuum. *Sov. Phys. JETP*, 62:204, 1985.

[36] E. V. Shuryak and J. J. M. Verbaarschot. Random matrix theory and spectral sum rules for the dirac operator in qcd. *Nucl. Phys.*, A560:306, 1993.

[37] E. V. Shuryak. The role of instantons in quantum chromodynamics. 1. physical vacuum. *Nucl. Phys.*, B203:93, 1982.

[38] E. V. Shuryak. The role of instantons in quantum chromodynamics. 2. hadronic structure. *Nucl. Phys.*, B203:116, 1982.

[39] E. V. Shuryak. The role of instantons in quantum chromodynamics. 3. quark - gluon plasma. *Nucl. Phys.*, B203:140, 1982.

[40] A. Smilga and J. J. M. Verbaarschot. Spectral sum rules and finite volume partition function in gauge theories with real and pseudoreal fermions. *Phys. Rev.*, D51:829, 1995.

[41] M. E. Peskin. The alignment of the vacuum in theories of technicolor. *Nucl. Phys.*, B175:197, 1980.

[42] S. Dimopoulos. Technicolored signatures. *Nucl. Phys.*, B168:69, 1980.

[43] Ya. I. Kogan, M. A. Shifman, and M. I. Vysotsky. Spontaneous breaking of chiral symmetry for real fermions and n=2 susy yang-mills theory. *Sov. J. Nucl. Phys.*, 42:318, 1985.

[44] A. Altland and M. R. Zirnbauer. Field theory of the quantum kicked rotor. *Phys. Rev. Lett.*, 77:4536, 1996.

[45] M. A. Halasz and J. J. M. Verbaarschot. Effective lagrangians and chiral random matrix theory. *Phys. Rev.*, D52:2563, 1995.

[46] G. Akemann, P. H. Damgaard, U. Magnea, and S. Nishigaki. Universality of random matrices in the microscopic limit and the dirac operator spectrum. *Nucl. Phys.*, B487:721, 1997.

[47] J. J. M. Verbaarschot and I. Zahed. Spectral density of the qcd dirac operator near zero virtuality. *Phys. Rev. Lett.*, 70:3852, 1993.

[48] J. J. M. Verbaarschot. The spectrum of the qcd dirac operator and chiral random matrix theory: The threefold way. *Phys. Rev. Lett.*, 72:2531, 1994.

[49] J. J. M. Verbaarschot. Spectral sum rules and selberg's integral formula. *Phys. Lett.*, B329:351, 1994.

[50] J. J. M. Verbaarschot. The spectrum of the dirac operator near zero virtuality for n(c) = 2 and chiral random matrix theory. *Nucl. Phys.*, B426:559, 1994.

[51] J. J. M. Verbaarschot and I. Zahed. Random matrix theory and qcd in three-dimensions. *Phys. Rev. Lett.*, 73:2288, 1994.

[52] P. H. Damgaard, J. C. Osborn, D. Toublan, and J. J. M. Verbaarschot. The microscopic spectral density of the QCD dirac operator. *Nucl. Phys.*, B547:305, 1999.

[53] A. Bohr and B. Mottelson. *Nuclear Structure I*. Benjamin, New York, 1969.

[54] K. G. Wilson. Confinement of quarks. *Phys. Rev.*, D10:2445, 1974.

[55] H. J. Rothe. *Lattice Gauge Theories*. World Scientific, Singapore, 1992.

[56] S. Elitzur. Impossibility of spontaneously breaking local symmetries. *Phys. Rev.*, D12:3978, 1975.

[57] K. G. Wilson. *in New Phenomena In Subnuclear Physics, ed. A. Zichichi, (Plenum Press, New York), Part A (1977) 69.*

[58] H. B. Nielsen and M. Ninomiya. Absense of neutrinos on a lattice. 1. proof by homotopy theory. *Nucl. Phys.*, B185:20, 1981. Erratum Nucl. Phys. B195 (1982) 541.

[59] H. B. Nielsen and M. Ninomiya. Absense of neutrinos on a lattice. 2. intuitive topological proof. *Nucl. Phys.*, B193:173, 1981.

[60] L. H. Karsten. Lattice fermions in euclidean space-time. *Phys. Lett.*, B104:315, 1981.

[61] J. B. Kogut and L. Susskind. Hamiltonian formulation of wilson's lattice gauge theories. *Phys. Rev.*, D11:395, 1975.

[62] L. Susskind. Lattice fermions. *Phys. Rev.*, D16:3031, 1977.

[63] J. B. Kogut. An introduction to lattice gauge theory and spin systems. *Rev. Mod. Phys.*, 51:659, 1979.

[64] H. S. Sharatchandra, H. J. Thun, and P. Weisz. Susskind fermions on a euclidean lattice. *Nucl. Phys.*, B192:205, 1981.

[65] H. Kluberg-Stern, A. Morel, O. Napoly, and B. Petersson. Flavors of lagrangean susskind fermions. *Nucl. Phys.*, B220:447, 1983.

[66] M. F. L. Golterman and J. Smit. Selfenergy and flavor interpretation of staggered fermions. *Nucl. Phys.*, B245:61, 1984.

[67] B. Bunk, M. Della Morte, K. Jansen, and F. Knechtli. The locality problem for two tastes of staggered fermions. 2004.

[68] P. H. Ginsparg and K. G. Wilson. A remnant of chiral symmetry on the lattice. *Phys. Rev.*, D25:2649, 1982.

[69] M. Lüscher. Exact chiral symmetry on the lattice and the ginsparg-wilson relation. *Phys. Lett.*, B428:342, 1998.

[70] P. Hasenfratz, V. Laliena, and F. Niedermayer. The index theorem in qcd with a finite cut-off. *Phys. Lett.*, B427:125, 1998.

[71] P. Hasenfratz. Lattice qcd without tuning, mixing and current renormalization. *Nucl. Phys.*, B525:401, 1998.

[72] Y. Kikukawa and H. Neuberger. Overlap in odd dimensions. *Nucl. Phys.*, B513:735, 1998.

[73] H. Neuberger. Exactly massless quarks on the lattice. *Phys. Lett.*, B417:141, 1998.

[74] H. Neuberger. More about exactly massless quarks on the lattice. *Phys. Lett.*, B427:353, 1998.

[75] W. Bietenholz. Solutions of the ginsparg-wilson relation and improved domain wall fermions. *Eur. Phys. J.*, C6:537, 1999.

[76] W. Bietenholz, N. Eicker, A. Frommer, Th. Lippert, B. Medeke, K. Schilling, and G. Weuffen. Preconditioning of improved and 'perfect' fermion actions. *Comput. Phys. Commun.*, 119:1, 1999.

[77] K. Wilson and J. Kogut. The renormalization group and the ϵ-expansion. *Phys. Rep.*, C12:75, 1974.

[78] L. P. Kadanoff. Lectures on the application of renormalization group techniques to quarks and strings. *Rev. Mod. Phys.*, 49:267, 1977.

[79] W. Bietenholz and U. J. Wiese. Perfect lattice actions for quarks and gluons. *Nucl. Phys.*, B464:319, 1996.

[80] W. Bietenholz. Chiral symmetry, renormalization group and fixed points for lattice fermions. *Proc. of XIV Brazilian National Meeting on Particles and Fields*, page 360.

[81] W. Bietenholz, R. Brower, S. Chandrasekharan, and U. J. Wiese. Progress on perfect lattice actions for qcd. *Nucl. Phys. Proc. Suppl.*, 53:921, 1997.

[82] W. Bietenholz and U. J. Wiese. Perfect actions with chemical potential. *Phys. Lett.*, B426:114, 1998.

[83] K. Orginos, W. Bietenholz, R. Brower, S. Chandrasekharan, and U. J. Wiese. The perfect quark-gluon vertex function. *Nucl. Phys. Proc. Suppl.*, 63:904, 1998.

[84] M. Creutz. Monte carlo study of quantized $su(2)$ gauge theory. *Phys. Rev.*, D21:2308, 1980.

[85] N. Metropolis, A. W. Rosenbluth, M. N. Rosenbluth, A. H. Teller, and E. Teller. *J. Chem. Phys.*, 21:1087, 1953.

[86] N. Cabibbo and E. Marinari. A new method for updating $su(n)$ matrices in computer simulations of gauge theories. *Phys. Lett.*, B119:387, 1982.

[87] S. L. Adler. An overrelaxation method for the monte carlo evaluation of the partition function for multiquadratic actions. *Phys. Rev.*, D23:2901, 1981.

[88] S. L. Adler. Overrelaxation algorithms for lattice field theories. *Phys. Rev.*, D37:458, 1988.

[89] F. R. Brown and T. J. Woch. Overrelaxed heat bath and metropolis algorithms for accelerating pure gauge monte carlo calculations. *Phys. Rev. Lett.*, 58:2394, 1987.

[90] M. Creutz. Overrelaxation and monte carlo simulation. *Phys. Rev.*, D36:515, 1987.

[91] P. Hernández, K. Jansen, and M. Lüscher. Locality properties of neuberger's lattice dirac operator. *Nucl. Phys.*, B552:363, 1999.

[92] W. H. Press, S. A. Teukolsky, W. T. Vetterling, and B. P. Flannery. *Numerical Recipes: The Art of Scientific Computing (2nd edition)*. Cambridge University Press, 1992.

[93] P. Hernández, K. Jansen, and L. Lellouch. Finite-size scaling of the quark condensate in quenched lattice qcd. *Phys. Lett.*, B469:198, 1999.

[94] W. Bietenholz. Approximate ginsparg-wilson fermions for qcd. *Proc. of the International Workshop on Non-Perturbative Methods and Lattice QCD Guangzhou (China), X.-Q. Luo and E.B. Gregory (eds.)*, page 3, 2000.

[95] K. Jansen. Private communication.

[96] W. Bietenholz. Convergence rate and locality of improved overlap fermions. *Nucl. Phys.*, B644:223, 2002.

[97] T. Blum and et al. Quenched lattice qcd with domain wall fermions and the chiral limit. *Phys. Rev.*, D69:074502, 2004.

[98] J. van den Eshof, A. Frommer, Th. Lippert, K. Schilling, and H. A. van der Vorst. Numerical methods for the qcd overlap operator. i: Sign-function and error bounds. *Comput. Phys. Commun.*, 146:203, 2002.

[99] L. Giusti, C. Hoelbling, M. Lüscher, and H. Wittig. Numerical techniques for lattice qcd in the ϵ- regime. *Comput. Phys. Commun.*, 153:31, 2003.

[100] G. Arnold, N. Cundy, J. van den Eshof, A. Frommer, S. Krieg, Th. Lippert, and K. Schafer. Numerical methods for the qcd overlap operator. ii: Optimal krylov subspace methods. 2003.

[101] N. Cundy and et. al. Numerical methods for the qcd overlap operator. iii: Nested iterations. 2004.

[102] T. Chiarappa, K. Jansen, K.-I. Nagai, M. Papinutto, L. Scorzato, A. Shindler, C. Urbach, U. Wenger, and I. Wetzorke. Comparing iterative methods for overlap and twisted mass fermions. 2004.

[103] W. Bietenholz, S. Capitani, T. Chiarappa, N. Christian, M. Hasenbusch, K. Jansen, K.-I. Nagai, M. Papinutto, L. Scorzato, S. Shcheredin, A. Shindler, C. Urbach, Wenger U., and I. Wetzorke. Going chiral: overlap versus twisted mass fermions. 2004.

[104] R. Sommer. A new way to set the energy scale in lattice gauge theories and its applications to the static force and α_s in su(2) yang-mills theory. *Nucl. Phys.*, B411:839, 1994.

[105] S. Necco and R. Sommer. The $n_f = 0$ heavy quark potential from short to intermediate distances. *Nucl. Phys.*, B622:328, 2002.

[106] M. Guagnelli, R. Sommer, and H. Wittig. Precision computation of a low-energy reference scale in quenched lattice qcd. *Nucl. Phys.*, B535:389, 1998.

[107] P. H. Damgaard, U. M. Heller, R. Niclasen, and K. Rummukainen. Looking for effects of topology in the dirac spectrum of staggered fermions. *Nucl. Phys. Proc. Suppl.*, 83:197, 2000.

[108] P. H. Damgaard, U. M. Heller, R. Niclasen, and K. Rummukainen. Staggered fermions and gauge field topology. *Phys. Rev.*, D61:014501, 2000.

[109] S. Dürr and C. Hoelbling. Staggered versus overlap fermions: A study in the schwinger model with $n_f = 0, 1, 2$. *Phys. Rev.*, D69:034503, 2004.

[110] E. Follana, A. Hart, and C. T. H. Davies. The index theorem and universality properties of the low- lying eigenvalues of improved staggered quarks. 2004.

[111] K. Y. Wong and R. M. Woloshyn. Topology and staggered fermion action improvement. 2004.

[112] F. Farchioni, I. Hip, and C. B. Lang. Effects of topology in the dirac spectrum of staggered fermions. *Phys. Lett.*, B471:58, 1999.

[113] F. Farchioni, I. Hip, C. B. Lang, and M. Wohlgenannt. Eigenvalue spectrum of massless dirac operators on the lattice. *Nucl. Phys.*, B549:364, 1999.

[114] B. A. Berg, U. M. Heller, H. Markum, R. Pullirsch, and W. Sakuler. Exact zero-modes of the compact qed dirac operator. *Phys. Lett.*, B514:97, 2001.

[115] R. G. Edwards, U. M. Heller, J. E. Kiskis, and R. Narayanan. Quark spectra, topology and random matrix theory. *Phys. Rev. Lett.*, 82:4188–4191, 1999.

[116] P. Hasenfratz, S. Hauswirth, T. Jörg, F. Niedermayer, and K. Holland. Testing the fixed-point qcd action and the construction of chiral currents. *Nucl. Phys.*, B643:280–320, 2002.

[117] W. Bietenholz, K. Jansen, and S. Shcheredin. Spectral properties of the overlap dirac operator in qcd. *JHEP*, 07:033, 2003.

[118] C. Lanczos. Solution of systems of linear equations by minimized iteration. *J. Res. Nat. Bur. Stand.*, 49:33, 1952.

[119] D. C. Sorensen. Implicit application of polynomial filters in a k-step arnoldi method. *Siam J. Matrix Anal. Appl.*, 13:357, 1992.

[120] F. Farchioni. Leutwyler-smilga sum rules for ginsparg-wilson lattice fermions. 1999.

[121] S. Capitani, M. Göckeler, R. Horsley, P. E. L. Rakow, and G. Schierholz. Operator improvement for ginsparg-wilson fermions. *Phys. Lett.*, B468:150, 1999.

[122] W. Bietenholz. Private notes.

[123] P. H. Damgaard. Quenched finite volume logarithms. *Nucl. Phys.*, B608:162, 2001.

[124] J. J. M. Verbaarschot and T. Wettig. Random matrix theory and chiral symmetry in qcd. *Ann. Rev. Nucl. Part. Sci.*, 50:343, 2000.

[125] L. Giusti, M. Lüscher, P. Weisz, and H. Wittig. Lattice qcd in the ϵ-regime and random matrix theory. *JHEP*, 11:023, 2003.

[126] E. Witten. Current algebra theorems for the $u(1)$ 'goldstone boson'. *Nucl. Phys.*, B156:269, 1979.

[127] G. Veneziano. $u(1)$ without instantons. *Nucl. Phys.*, B159:213, 1979.

[128] L. Giusti, G. C. Rossi, and M. Testa. Topological susceptibility in full qcd with ginsparg-wilson fermions. *Phys. Lett.*, B587:157, 2004.

[129] M. Lüscher. Topological effects in qcd and the problem of short-distance singularities. 2004.

[130] L. Giusti, G. C. Rossi, M. Testa, and G. Veneziano. The $u_a(1)$ problem on the lattice with ginsparg-wilson fermions. *Nucl. Phys.*, B628:234, 2002.

[131] S. Chandrasekharan and U. J. Wiese. An introduction to chiral symmetry on the lattice. *Prog. Part. Nucl. Phys.*, 53:373, 2004.

[132] L. Del Debbio and C. Pica. Topological susceptibility from the overlap. *JHEP*, 02:003, 2004.

[133] L. Del Debbio, L. Giusti, and C. Pica. Topological susceptibility in the su(3) gauge theory. 2004.

[134] W. Bietenholz, T. Chiarappa, K. Jansen, K.-I. Nagai, and S. Shcheredin. Axial correlation functions in the ϵ-regime: A numerical study with overlap fermions. *JHEP*, 02:023, 2004.

[135] B. Bunk, K. Jansen, M. Lüscher, and H. Simma. Desy report (september 1994).

[136] T. Kalkreuter and H. Simma. An accelerated conjugate gradient algorithm to compute low lying eigenvalues: A study for the dirac operator in $su(2)$ lattice qcd. *Comput. Phys. Commun.*, 93:33, 1996.

[137] F. Berruto, N. Garron, C. Hoelbling, L. Lellouch, C. Rebbi, and N. Shoresh. Preliminary results from a simulation of quenched qcd with overlap fermions on a large lattice. *Nucl. Phys. Proc. Suppl.*, 129:471, 2004.

[138] L. Giusti, P. Hernandez, M. Laine, P. Weisz, and H. Wittig. Low-energy couplings of qcd from current correlators near the chiral limit. *JHEP*, 04:013, 2004.

[139] S. A. Gottlieb, P. B. MacKenzie, H. B. Thacker, and D. Weingarten. Hadronic couplings constants in lattice gauge theory. *Nucl. Phys.*, B263:704, 1986.

[140] R. Gupta, G. Guralnik, G. Kilcup, A. Patel, S. R. Sharpe, and T. Warnock. The hadron spectrum on a $18^3 \times 42$ lattice. *Phys. Rev.*, D36:2813, 1987.

[141] H. Neuberger. Bounds on the wilson dirac operator. *Phys. Rev.*, D61:085015, 2000.

[142] M. Lüscher. Abelian chiral gauge theories on the lattice with exact gauge invariance. *Nucl. Phys.*, B549:295, 1999.

[143] M. Lüscher. Weyl fermions on the lattice and the non-abelian gauge anomaly. *Nucl. Phys.*, B568:162, 2000.

[144] H. Fukaya and T. Onogi. Lattice study of the massive schwinger model with theta term under lüscher's 'admissibility' condition. *Phys. Rev.*, D68:074503, 2003.

[145] M. Creutz. Positivity and topology in lattice gauge theory. 2004.

[146] S. Shcheredin, W. Bietenholz, K. Jansen, K.-I. Nagai, S. Necco, and L. Scorzato. Testing a topology conserving gauge action in qcd. 2004.

[147] E.-M. Ilgenfritz, M. L. Laursen, G. Schierholz, M. Müller-Preussker, and H. Schiller. First evidence for the existence of instantons in the quantized su(2) lattice vacuum. *Nucl. Phys.*, B268:693, 1986.

[148] E.-M. Ilgenfritz, B. V. Martemyanov, M. Müller-Preussker, S. Shcheredin, and A. I. Veselov. On the topological content of su(2) gauge fields below t(c). *Phys. Rev.*, D66:074503, 2002.

[149] K.-I. Nagai, W. Bietenholz, T. Chiarappa, K. Jansen, and S. Shcheredin. Simulations in the ϵ-regime of chiral perturbation theory. *Nucl. Phys. Proc. Suppl.*, 129:516, 2004.

[150] P. Marenzoni, L. Pugnetti, and P. Rossi. Measure of autocorrelation times of local hybrid monte carlo algorithm for lattice qcd. *Phys. Lett.*, B315:152, 1993.

[151] R. T. Scalettar, D. J. Scalapino, and R. L. Sugar. New algorithm for the numerical simulation of fermions. *Phys. Rev.*, B34:7911, 1986.

[152] S. Duane, A. D. Kennedy, B. J. Pendleton, and D. Roweth. Hybrid monte carlo. *Phys. Lett.*, B195:216, 1987.

Appendix A

A local Hybrid Monte Carlo algorithm

In this Appendix we discuss the implementation of the local HMC algorithm [150] that we used to simulate the Lüscher gauge action. It is based on the HMC algorithm described in Refs. [151, 152]

Let us consider the Hamiltonian of the $SU(3)$ gauge theory

$$H[\pi, U] = \frac{1}{2} \sum_{x,\mu} \sum_{j=1}^{8} \pi_{x,\mu,j}^2 + S_{\text{YM}}[U] \ . \tag{A.1}$$

We define $\pi_{x,\mu} = \sum_{j=1}^{8} \pi_{x,\mu,j} \lambda_j$, where λ_j are the Gell-Mann matrices for the $SU(3)$ gauge group. The variables $\pi_{x,\mu}$ are canonical momenta for $U_{x,\mu}$. The local HMC algorithm for the simulation of the gauge fields $U_{x,\mu} \in SU(3)$ starts off by choosing a random value of the momentum $\pi_{x,\mu}$ according to the Gaussian distribution

$$P_G[\pi_{x,\mu}] \propto \prod_{j=1}^{8} \exp\left\{ -\frac{1}{2} \pi_{x,\mu,j}^2 \right\} \ . \tag{A.2}$$

Then, using the Hamiltonian H the pair $[\pi_{x,\mu}, U_{x,\mu}]$ is changed along the discretized trajectory in phase space up to the end point $[\pi'_{x,\mu}, U'_{x,\mu}] \equiv T_H[\pi, U]$, where T_H is the discretized evolution operator corresponding to the Hamiltonian H. It is assumed that the discretized classical dynamics equations, which define the operator T_H, are such that the mapping $[\pi_{x,\mu}, U_{x,\mu}] \rightarrow [\pi'_{x,\mu}, U'_{x,\mu}]$ is reversible in the sense

$$P_H([\pi'_{x,\mu}, U'_{x,\mu}] \leftarrow [\pi_{x,\mu}, U_{x,\mu}]) = P_H([-\pi_{x,\mu}, U_{x,\mu}] \leftarrow [-\pi'_{x,\mu}, U'_{x,\mu}]) \ . \tag{A.3}$$

P_H is the probability of the configuration transition

$$P_H([\pi'_{x,\mu}, U'_{x,\mu}] \leftarrow [\pi_{x,\mu}, U_{x,\mu}]) = \delta([\pi'_{x,\mu}, U'_{x,\mu}] - T_H[\pi_{x,\mu}, U_{x,\mu}]) , \quad \text{(A.4)}$$

which takes this form since the change is deterministic in the case of the classical equations of motion. The reversibility condition holds for instance for the leap frog integration. After the trajectory $[\pi_{x,\mu}, U_{x,\mu}] \rightarrow [\pi'_{x,\mu}, U'_{x,\mu}]$ is determined, the pair $[\pi'_{x,\mu}, U'_{x,\mu}]$ is either accepted or rejected, and the old pair $[\pi_{x,\mu}, U_{x,\mu}]$ is kept. The acceptance is defined by the Metropolis probability

$$P_A([\pi'_{x,\mu}, U'_{x,\mu}] \leftarrow [\pi_{x,\mu}, U_{x,\mu}]) = \min\left\{ 1, e^{-\Delta H[\pi'_{x,\mu}, U'_{x,\mu}] + \Delta H[\pi_{x,\mu}, U_{x,\mu}]} \right\} , \quad \text{(A.5)}$$

where

$$\Delta H[\pi_{x,\mu}, U_{x,\mu}] = \sum_{j=1}^{8} \frac{1}{2}\pi_{x,\mu,j}^2 + \sum_{\mu < \nu} \beta\, S_P(U_{x,\mu\nu}^{(P)}) \quad \text{(A.6)}$$

is the part of the Hamiltonian H which includes $\pi_{x,\mu}$ and $U_{x,\mu}$. The total transition probability is

$$\begin{aligned} P([U'_{x,\mu} \leftarrow U_{x,\mu}]) &= \int [d\pi_{x,\mu}\, d\pi'_{x,\mu}]\, P_A([\pi'_{x,\mu}, U'_{x,\mu}] \leftarrow [\pi_{x,\mu}, U_{x,\mu}]) \times \\ &\quad P_H([\pi'_{x,\mu}, U'_{x,\mu}] \leftarrow [\pi_{x,\mu}, U_{x,\mu}])\, P_G[\pi_{x,\mu}] . \quad \text{(A.7)} \end{aligned}$$

It can be shown that this probability distribution has the canonical distribution proportional to $\exp(-S_{\mathrm{YM}}[U])$ as a unique fixed point. It can be proved by using the reversibility condition (A.3). Therefore a finite difference approximation to the Hamiltonian equations must also account for it.

Applying now this algorithm to each pair $[\pi_{x,\mu}, U_{x,\mu}]$ we perform the update of the gauge field throughout the lattice.

We close the explanation of the algorithm by giving the description of the finite difference approximation to the Hamiltonian equations, i.e. to the evolution operator T_H. It is given by the leapfrog integration, which proceeds as follows: one performs a first half step

$$\pi_{x,\mu,j}\left(\frac{\Delta\tau}{2}\right) = \pi_{x,\mu,j}(0) - \frac{\delta\Delta S_{\mathrm{YM}}[U_{x,\mu}(0)]}{\delta_j U_{x,\mu}} \frac{\Delta\tau}{2} , \quad \text{(A.8)}$$

and then for steps $k = 0, 1, \ldots, n-1$

$$U_{x,\mu}(k\Delta\tau + \Delta\tau) = \exp\left\{ \sum_{j=1}^{8} i\lambda_j \pi_{x,\mu,j}\left(k\Delta\tau + \frac{\Delta\tau}{2}\right)\Delta\tau \right\} U_{x,\mu}(k\Delta\tau) , \quad \text{(A.9)}$$

and for $k = 1, 2, \ldots, n-1$

$$\pi_{x,\mu,j}(k\Delta\tau + \frac{\Delta\tau}{2}) = \pi_{x,\mu,j}(k\Delta\tau - \frac{\Delta\tau}{2}) - \frac{\delta\Delta S_{\mathrm{YM}}[U_{x,\mu}(k\Delta\tau)]}{\delta_j U_{x,\mu}}\Delta\tau , \quad \text{(A.10)}$$

and finally

$$\pi_{x,\mu,j}(n\Delta\tau) = \pi_{x,\mu,j}(n\Delta\tau - \frac{\Delta\tau}{2}) - \frac{\delta\Delta S_{\mathrm{YM}}[U_{x,\mu}(n\Delta\tau)]}{\delta_j U_{x,\mu}}\Delta\tau , \quad \text{(A.11)}$$

where $\Delta S_{\mathrm{YM}}[U_{x,\mu}] = \sum_{\mu<\nu} \beta \, S_P(U_{x,\mu\nu}^{(P)})$ is the part of the lattice gauge action which contains $U_{x,\mu}$. The derivative appearing in these formulae is defined as

$$\frac{\delta f[U_{x,\mu}]}{\delta_j U_{x,\mu}} = \frac{\partial}{\partial\alpha} f \left[e^{i\alpha\lambda_j} U_{x,\mu} \right]_{\alpha=0} . \quad \text{(A.12)}$$

Curriculum Vitae

Name:	Stanislav Shcheredin
1996 - 2002	Study at Moscow State University
	field Physics
02/2002 - 02/2005	Ph.D. at
	Humboldt University Berlin,
	Chair Prof. M. Müller-Preußker,
	Institute for Physics

Selbständigkeitserklärung

Hiermit erkläre ich, die vorliegende Arbeit selbständig ohne fremde Hilfe verfaßt und nur die angegebene Literatur und Hilfsmittel verwendet zu haben.

Stanislav Shcheredin
1. November 2004